Effect of the cylindrical reactor length on fullerene synthesis

based on the thermal plasma dissociation of C2Cl4

David Harbec

Department of Chemical Engineering McGill University Montreal, Quebec, Canada

Under the supervision of Prof. Jean-Luc Meunier and Dr. Theodora Alexakis

A thesis submitted to the Faculty of Graduate Studies and Research in partial fulfilment of the requirements of the degree of Master of Engineering



National Library of Canada

Acquisitions and Bibliographic Services

395 Wellington Street Ottawa ON K1A 0N4 Canada Bibliothèque nationale du Canada

Acquisitions et services bibliographiques

395, rue Wellington Ottawa ON K1A 0N4 Canada

Your Me Votre reterence

Our Ste Notre reterence

The author has granted a non-exclusive licence allowing the National Library of Canada to reproduce, loan, distribute or sell copies of this thesis in microform, paper or electronic formats.

The author retains ownership of the copyright in this thesis. Neither the thesis nor substantial extracts from it may be printed or otherwise reproduced without the author's permission.

L'auteur a accordé une licence non exclusive permettant à la Bibliothèque nationale du Canada de reproduire, prêter, distribuer ou vendre des copies de cette thèse sous la forme de microfiche/film, de reproduction sur papier ou sur format électronique.

L'auteur conserve la propriété du droit d'auteur qui protège cette thèse. Ni la thèse ni des extraits substantiels de celle-ci ne doivent être imprimés ou autrement reproduits sans son autorisation.

0-612-79075-4



Abstract

A new approach for the synthesis of fullerenes (C_{60} , C_{70}) using a 100kW D.C non-transferred thermal plasma torch is based on the dissociation of tetrachloroethylene (C_2Cl_4). Experimental tests performed in a spherical reactor (ID=30cm) showed a high production rate of up to 9 g/h of fullerenes and indicated a good scale-up potential. CFD modeling demonstrated an increase of the C_{60} yield with the residence time of the precursor species in the 2200-2600 K temperature window for fullerene formation, but strong limitations from the reactor geometry.

A new cylindrical reactor was designed (ID=40 cm) with the flexibility to modify its length up to L=100 cm. An improvement of the precursor residence time by a factor of 100 is calculated in the new reactor design. CFD Modeling and spectroscopy temperature profiles on off-core plasma regions are within the same scale. Low fullerene yield (1.2 g/h) suggests reactor wall temperature optimization. Fullerene yield increases as a function of reactor length.

Résumé

Une nouvelle approche pour la synthèse des fullerènes (C₆₀, C₇₀) utilisant une torche à plasma thermique à courant continu non-transféré de 100 kW est basée sur la dissociation du tetrachloroéthylène (C₂Cl₄). De hauts rendements, allant jusqu'à 9 g/h de fullerènes, dans un réacteur sphérique (φ=30 cm) ont indiqué la possibilité d'accroître l'échelle de production. Une modélisation CFD a démontré une augmentation du rendement C₆₀ en fonction du temps de résidence des précurseurs dans la fenêtre de température 2200-2600K pour la formation des fullerènes, mais de grandes limitations de la géométrie sphérique.

Un nouveau réacteur cylindrique a été conçu (\$\phi=40\$ cm) avec la flexibilité de modifier sa longueur jusqu'à L=100 cm. Une amélioration du temps de résidence des précurseurs d'un facteur 100 a été calculée dans le nouveau design. Les profils de température provenant de la modélisation CFD et de la spectroscopie se concordent bien pour les valeurs situées hors de l'axe du jet plasma. Le rendement bas en fullerènes (1,2 g/h) suggère qu'une optimisation de la température des parois du réacteur soit nécessaire. Le rendement en fullerènes augmente en fonction de la longueur du réacteur.

Acknowledgement

I would like to take this opportunity to thank all those who have helped me in the pursuit of this degree:

- Prof. Jean-Luc Meunier, my supervisor, his valuable guidance, fundamental insight, and support in this research project.
- Dr. Theodora Alexakis, from *Pyrogenesis Inc.*, for sharing her previous experience with the project and for her interest to my huge amount of questions.
- Dr. Manitra Razafinimanana, Dr. Philippe Teulet and Mrs. Marquidia Pacheco, from the Toulouse plasma physics centre in France, for their plasma diagnostic expertise and help with the spectroscopy equipment.
- Dr. Burhanettin Çiçek, from Ankara University, for his chemical engineering point of view contribution in starting this project.
- Jörg Oberste-Berghaus, for freely sharing his expertise in the lab and numerous enlightening discussions. And the rest of the McGill plasma group, in particular Prof. Richard J. Munz, Mr. Hongsun Seon and Mr. Felipe Aristizabal, for the useful exchange of ideas and group meetings.
- Mr. Maxime Daneau, Mr. Jocelyn Rémillard and the rest of the *Pyrogenesis* automation and machine shop group, for their technical support on the thermal plasma torch system and their patience in changing and re-machining my burned parts.
- Mrs. Irina Grigore, from *Pyrogenesis Inc.*, for her huge contribution on the fullerene quantification procedure.

- The McGill chemical engineering machine shop staff, in particular Mr. Alain Gagnon, Mr. Walter Greenland, Mr. Charles Dolan, for materializing my abstract ideas and drawings. They were sometime hard to understand!
- Mr. Lou Cusmich and Mr. Frank Caporuscio, for their technical knowledge in electronics and lab equipment and especially their sense of humour.
- To the rest of the McGill chemical engineering staff, especially the storekeepers and secretaries, without whom this project could not have been realized.
- Finally, to my parents (Réjean and Diane), sister (Nathalie) and brother (Sébastien), for their love and encouragements to develop my full potential, even in the worst moments.

This research project came possible with the financial support of the Natural Science and Engineering Research Council (NSERC) and *Pyrogenesis Inc.*, in Montreal, Quebec.

Table of Contents

	Page
Chapter 1: Introduction	1
1.1 Structure and Properties of Fullerenes	4
1.2 Toward Tangible Applications of Fullerenes	6
1.2.1 Battery and Fuel Cell Electrodes	6 7
1.2.2 Gas Storage 1.2.3 Diamond Precursor	
	8 8
1.2.4 Strengthening/Hardening of Materials	9
1.2.5 Optical Applications 1.2.6 Sensor Applications	9
1.2.0 Sensor Applications	9
Chapter 2: Literature Review	11
2.1 Overview of Fullerene Synthesis Methods	11
2.1.1 Vaporization of Graphite	11
2.1.2 Combustion of Hydrocarbons	16
2.1.3 Injection of Carbon Materials into a Plasma Torch	17
2.2 Mechanisms of Formation	26
Chapter 3: Experimental	29
3.1 Apparatus and Instrumentation	29
3.1.1 Reactor Assembly Process Description	29
3.1.2 Plasma Torch System	31
3.1.3 Leak Detection	32
3.1.4 Real-Time Temperature Acquisition	33
3.1.5 Power Supply	33
3.1.6 C ₂ Cl ₄ Injection System	33
3.1.7 Vacuum System	34
3.1.8 Exhaust Gas Neutralizing System	35
3.2 Extraction and Purification of Fullerenes	35
3.2.1 Laboratory Equipment and Instrumentation	35
3.2.2 Quantification of Fullerenes	35
3.3 Optical Setup	36
Chapter 4: Procedure and Analysis	38
4.1 Operation of Soot Production System	38
4.2 Mass Spectrometry	39
4.3 Extraction of Fullerenes from Soot	40
4.4 Quantification of Fullerenes in Crude Extract	40
	. •
Chapter 5: Modeling Background	41
5.1 Explanation of Model	41
5.1.1 Assumptions made by Bilodeau <i>et al.</i> [6]	41
5.1.2 Boundary Conditions	42.

Chapter 6: Diagnostic Background	45
6.1 Generalities on Thermodynamic Equilibrium	46
6.1.1 Complete Thermodynamic Equilibrium (CTE)	46
6.1.2 Local Thermodynamic Equilibrium (LTE)	47
6.2 Temperature Determination using Atomic Lines	48
6.3 Temperature Determination using Molecular Lines (C ₂)	49
6.4 Abel Inversion	50
Chapter 7: Results and Discussion	53
7.1 Modeling	53
7.2 Spectroscopy Results	57
7.3 Soot Generation Experimental Results	62
7.3.1 Vacuum Trials and Improvements	62
7.3.2 Overall Energy Balance	64
7.3.3 Overall Mass Balance	66
7.3.4 Effect of Reactor Length on Fullerene Production	68
7.3.5 Soot Quality Reproducibility	71
Conclusions	73
Future Work	77
References	78
Appendix I: C ₆₀ Physical Constants	82
Appendix II: Modeling of the Different Reactor Length	84

List of Figures

	<u>Page</u>
Figure 1.1: Structures of C ₆₀ and C ₇₀	2
Figure 1.2: Structures of higher fullerenes and buckytubes	2
Figure 1.3: Relation between the lattice expansion and the increases of T _c	6
Figure 2.1: Schematic of an arc discharge generator	12
Figure 2.2: Fullerene content in collected soot versus electrode gap	13
Figure 2.3: <i>Pyrogenesis</i> reactor system	17
Figure 2.4: Experimental yield vs. theoretical residence time	19
Figure 2.5: Overall C ₆₀ and C ₇₀ yields as a function of C ₂ Cl ₄ feed	
and torch power level	20
Figure 2.6: Overall C_{60} and C_{70} collection rate as a function of run duration	21
Figure 2.7: Microwave fullerene synthesis system	22
Figure 2.8: Cota-Sánchez <i>et al.</i> experimental Setup [11]	24
Figure 2.9: Formation of C_{60} and C_{70} via the <i>Direct Pathway</i>	28
Figure 3.1: New reactor assembly	29
Figure 3.2: Schematic of the overall fullerene soot production	30
Figure 3.3: Cross-sectional view of the plasma torch (<i>Pyrogenesis</i> RPT2 model)	•
Figure 3.4: Optical setup	37
Figure 4.1: MS output of soot produced in the cylindrical reactor	39
Figure 5.1: Computational domain of the simulated reactor adapted from	
the spherical model	42
Figure 5.2: Actual experimental reactor geometry	42
Figure 6.1: Level transition representation of an electron	48
Figure 6.2: Simulated Swan band for a temperature of 4000 K	50
Figure 6.3: Illustration of the Abel Inversion	51
Figure 7.1: Reactor Isotherms (K) from modeling in the 1 m long	
cylindrical reactor	53
Figure 7.2: Velocity vectors from modeling in the 1 m long cylindrical reactor	54
Figure 7.3: Velocity vectors from modeling in the spherical reactor (ID=30 cm)	56
Figure 7.4: Modeled temperature profile (K) near the nozzle exit region	58
Figure 7.5: Temperature profiles measured from line of sight intensities	
and from modeling	58
Figure 7.6: Boltzmann plot on Swan Band obtained at point (0, 0.6)	
on the plasma jet	59
Figure 7.7: Hypothetical Temperature pattern showing maximum temperature	
in the core of the jet, and the Swan band (C ₂) emissivity as a function of radius	70
in line of sight positions y=0	60

Figure 7.8: Temperature point of measurement between modeling	
and experimental acquisitions	62
Figure 7.9: Percentage of C ₆₀ in soot and CN density versus base vacuum	64
Figure 7.10: System definition for energy balance calculations	64
Figure 7.11: Deposition yield for total soot	67
Figure 7.12: Replicate comparison following their soot quality	71
Figure AII.1: Temperature profile (K) from modeling [helium flow: 225 slpm; torch power: 55kW; C ₂ Cl ₄ flow: 0.29 mol/min; pressure: 200 torr, reactor length 40 cm]	86
Figure AII.2: Temperature profile (K) from modeling [helium flow: 225 slpm; torch power: 55kW; C ₂ Cl ₄ flow: 0.29 mol/min; pressure: 200 torr, reactor length 63 cm]	87
Figure AII.3: Temperature profile (K) from modeling [helium flow: 225 slpm; torch power: 55kW; C ₂ Cl ₄ flow: 0.29 mol/min; pressure: 200 torr, reactor length 88 cm]	88

List of Tables

Table 2.1: Operating parameters of fullerene synthesis using the arc discharge method	13
Table 2.2: Operating parameters and C_{60} yield comparisons in using different electrode composition	14
Table 2.3: Theoretical estimation of residence time in 2200-2600 K zone and associated production yields	19
Table 2.4: Yields of C ₆₀ and C ₇₀ according to temperature zone in the reactor	23
Table 2.5: Wang et al., [49] experimental conditions	26
Table 3.1: Pyrogenesis RPT2 plasma torch operating parameter specs	31
Table 6.1: Data of the selected spectral lines of Helium	49
Table 7.1: Comparison of residence times in 2200-2600 K zone obtained in the cylindrical (1 m long) and spherical reactors	55
Table 7.2: Residence times in 2200-2600K zone versus three investigated reactor length during the experimental soot generation	56
Table 7.3: Summary of the calorimetric study	65
Table 7.4: Summary of percentage mass recovery	67
Table 7.5: C ₆₀ yields associated with the length or the type of reactor	69
Table 7.6: Standard deviation calculations of replicate soot quality	71
Table AI.1: Physical constants for C ₆₀ molecules	82
Table AI.2: Physical constants for crystalline C ₆₀ in the solid state	83

Being the third allotrope of carbon after diamond and graphite, C_{60} and C_{70} (Figure 1.1) are the most common forms of the fullerene family, composed partially of $\rm sp^2$ and $\rm sp^3$ -hybridized carbons. Unlike aromatics, fullerenes have no hydrogen atom or any other groups attached. Lower fullerenes (C_{60} to C_{84}) (Figure 1.1 and 1.2) are truncated icosahedrons, which look like a soccerball. Each molecule (C_n) consists of 12 pentagons and a certain number of hexagons (m) obeying Euler's theorem: m=(n-20)/2 [47]. C_{60} and C_{70} are the smallest fullerenes for which this theorem applies. All other fullerenes having fewer carbon atoms have some pentagonal faces, which makes a more elongated molecule. Molecules having a high number of carbon atoms (of the other of hundred) are stretched as long tubes and called buckytubes or nanotubes (Figure 1.2).

The fullerene structure possesses unique physical, chemical, electrochemical and biological properties. It promises to launch a collection of new compounds, with possible uses in electronics, gas storage (oxygen, hydrogen and others), materials, catalysts, diamond film production, optical sensors and pharmaceuticals. The excellent future of fullerenes is due to their outstanding properties: fullerenes are superconductive, indifferent to the most violent shocks, fibers of 5 nanometers may be generated and it is consistent lubricant [37][51].

Fullerenes were discovered in carbon vapor obtained from the laser irradiation of graphite [26] and their formation occurs in a temperature window between 2200 K and 2600 K [31]. At the moment, fullerenes may be produced at high cost and low scale-up potential via the graphite vaporization with resistive heating or arc discharge [15][19][22]. For the moment, the separation/refining step of soot into purified fullerenes contributes significantly to the high costs of production. Although these processes are capable to produce common (C₆₀, C₇₀, etc) and higher fullerenes (e.g. nanotubes), the lack of economical large-scale production and purification avoid their tangible industrial application [51].

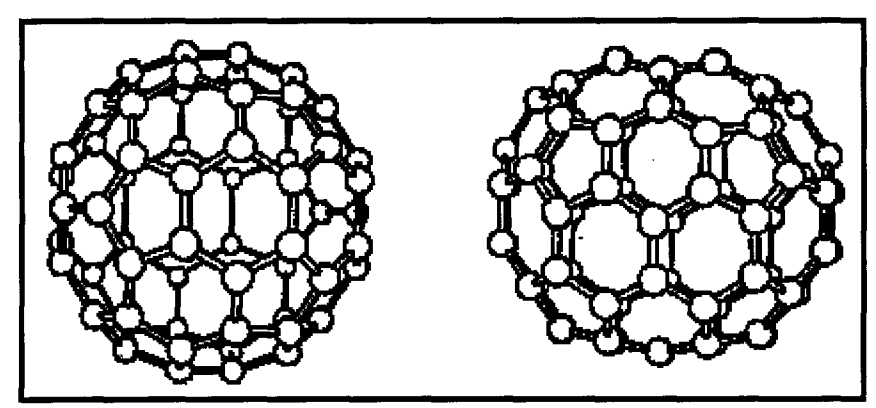


Figure 1.1: Structures of C₆₀ (left) and C₇₀ (right) [1]

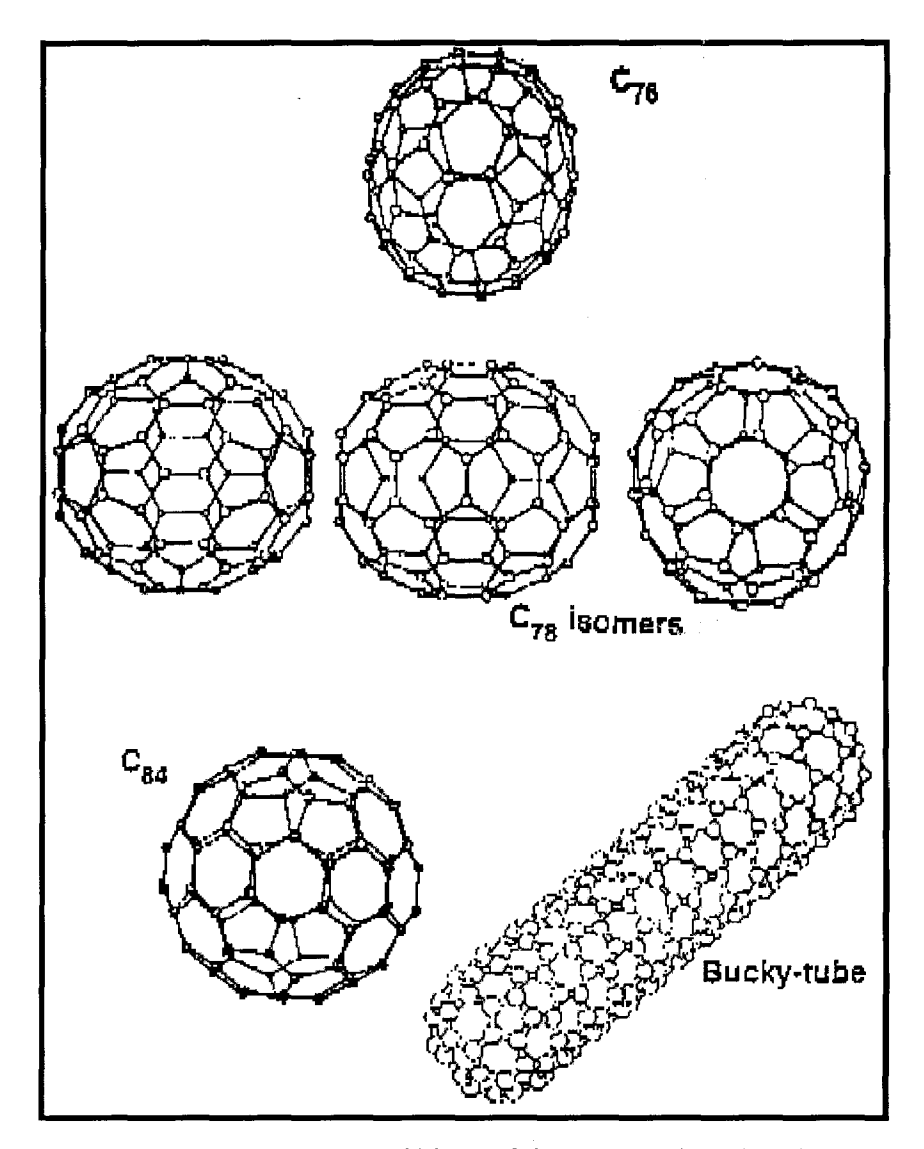


Figure 1.2: Structures of higher fullerenes and buckytubes [1]

In 1992, research at *Pyrogenesis*, in Montreal, Quebec led to the development of a potential large scale process in which fullerenes were produced via the thermal plasma dissociation of halogenated carbons in a spherical reactor. Tetrachloroethylene (C₂Cl₄) was selected as the carbon source for fullerene synthesis because of its unstable C-Cl bonds in the high temperature zone predicted for fullerene formation. This finding is based on the minimization of the Gibbs free energy of several carbon sources as starting material. By controlling the temperature gradient in the reactor, carbon atoms recombine themselves to form many types of carbon molecules, including fullerenes, which deposit as a soot film on the reactor inside wall. The mechanism of formation of fullerenes is still unknown using this method of production. Once the soot is collected and subjected to solvent extraction, the quantification of fullerene in the soot film is executed by high performance liquid chromatography (HPLC) analysis, [1][2].

The present thesis proposes the study of the *Pyrogenesis* process in a cylindrical reactor in order to inquire if this geometry improves the production performance of fullerenes and forecasts large scale potential. Following the synthesis results in the original reactor and modeling of the flow and temperature fields, recommendations were made relative to the reactor design geometry. This master thesis work is focused on the following objectives:

- I. Measure the temperature profiles of the He + C₂Cl₄ plasma flame in the cylindrical reactor.
- II. Modify the model developed by Bilodeau *et al.* [6] to cylindrical coordinates in order to investigate the temperature profile and residence time for various operating conditions.
- III. Measure fullerene yields for three different reactor lengths for preliminary process optimization.

1.1: Structure and Properties of Fullerenes

The 60 carbon atoms in C_{60} are arranged into a truncated icosahedron, where all carbon sites are equivalent vertices. Euler's theorem stipulates that a regular truncated icosahedron has 90 edges of equal length, 60 equivalent vertices, 20 hexagonal faces, and 12 additional pentagonal faces to form a closed shell. Inspection of C_{60} structure shows that every pentagon is surrounded by five hexagons (Figure 1.1), giving the form of corannulene. For each carbon atom, two single C-C bonds are located along edges of the fusion of a pentagonal and hexagonal faces. A double C-C bond follows edge at the fusion of two hexagons. Hybridization of C_{60} is a mixture of sp² and sp³, leading to its curvature, which strongly affect chemical reactivity, thermal and electrical conductivity, superconductivity and optical properties of fullerenes. The average nearest-neighbor carbon-carbon distance of C_{60} lies between graphite and diamond with 1.44 Å. However, the single bonds are 1.46 Å and 1.455 Å, and the double bonds are 1.40 Å and 1.391 Å as measured by NMR and neutron scattering respectively [12]. Appendix I lists additional physical quantities for C_{60} as molecules and solid state.

Primitive x-ray powder diffraction (XRD) patterns on crystalline C_{60} suggested hexagonal close-packed (hcp) lattice. An enhanced single-crystal study shows that molecules take place in a face-centered cubic (fcc) lattice form with a lattice constant of 14.17 Å, a nearest-neighbor C_{60} - C_{60} distance of 10.02 Å and a density of 1.72 g/cm³ [12][14]. Li *et al.*, [29] determined a lattice constant of 14.16 Å under a fcc crystalline form and performed Vickers hardness measurements on the (100) and (111) faces. Vickers numbers were respectively H_v =14.5±0.6 and 17.5±0.5. Compared to H_v =25 for pure gold, C_{60} seems to be a soft material.

The van der Waals forces, retaining solid state C_{60} together, simplified dissolution and evaporation processes, since they are much weaker than covalent carbon-carbon bonds. Also, this weak bonding allows easy compression in three dimensions, rather than in one dimension as in the case of graphite [12]. Fischer *et al.* [14] and Duclos *et al.* [13] demonstrated that crystalline C_{60} is relatively compressible. The first paper revealed an

isothermal volume compressibility of 6.9 X 10^{-12} cm²/dyne. The second completed a soft equation of state for solid C₆₀ from 0 to 20 GPa, which resulted in an atmospheric-pressure bulk modulus K_o=18.1±1.8 GPa and pressure derivative dK_o/dP=5.7±0.6.

During the past decade, researchers studied chemistry, especially oxidation [10][42] and superconductivity [43] of fullerenes and isolation of higher fullerenes (C_{76} , C_{78} , C_{82} , C_{84} , C_{90} , C_{96}) [25]. Chen *et al.* [10] studied the behavior of C_{60} in pure oxygen at 200°C. Under this condition, the fcc crystalline shape transforms into amorphous carbon-oxygen compounds and icosahedral structure get destroyed. The authors note 12 as the maximum oxygen uptake of pure C_{60} (O/ C_{60}).

Saxby *et al.* [42] realized oxidation of purified C_{60} by thermogravimetric analysis in air. They demonstrated that increasing the heating rate from 1 to 20°C/min increases the temperature of maximum rate of weight loss from 444 to 600°C. At 1°C/min, C_{60} start to decompose at a lower temperature (444°C) than diamond (629°C), graphite (644°C), and soot (565°).

Preliminary research works stated that a crystal made with C₆₀ molecules would turn superconducting at a superconducting transition temperature (T_c) of 18 K if they are spiked with alkali metals for a better conducting behavior. Superconductors can be stimulated by conducting positively charged holes (electron vacancies), which increases the crystal lattice distance, the density of states and consequently, T_c. Schön *et al.* [43] anticipated to implement gate-induced hole doping in C₆₀, resulting to an increase of T_c to 52 K. Such results suggest that higher T_c's might be obtained with suitable "expanded" fullerene crystals. The research group tried numerous of additives. It was found that CHCl₃ expands the C₆₀ lattice constant to 14.29 Å and CHBr₃, to 14.45 Å. Figure 1.3 relates this lattice constant expansion to the increases of T_c [43].

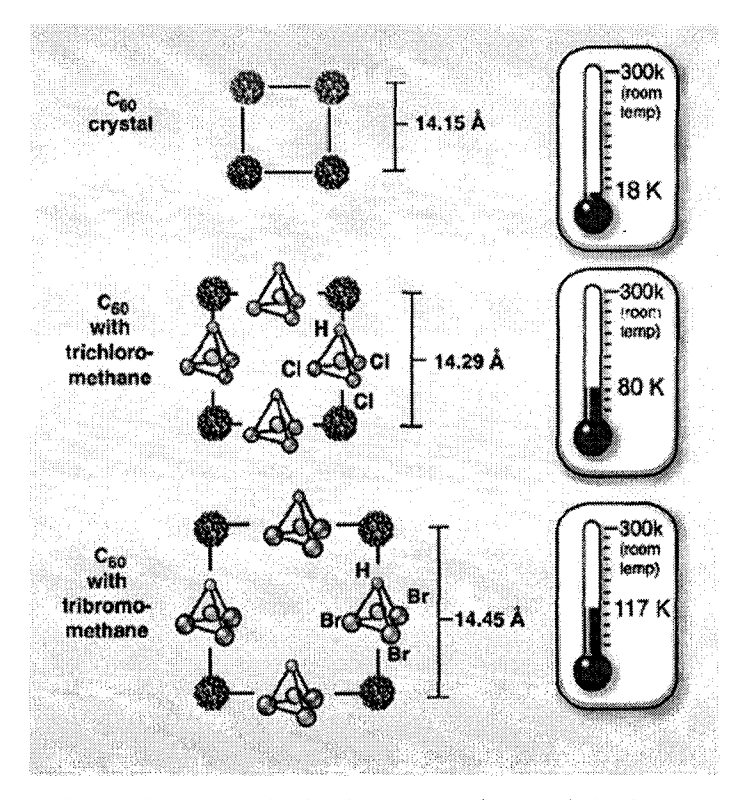


Figure 1.3: Relation between the lattice expansion and the increases of T_c [43]

1.2: Toward Tangible Applications of Fullerenes

Fullerene property studies keep attention on future commercial usage in [51]:

- 1. Battery and Fuel Cell Electrodes
- 2. Gas Storage (oxygen, hydrogen and others)
- 3. as Precursor to Diamond
- 4. Strengthening/Hardening of Materials
- 5. Optical Applications
- 6. Sensor Applications

1.2.1 Battery and Fuel Cell Electrodes

Fullerenes may revolutionize nickel-metal hydride and lithium-ion battery technology due to their capacity to be electrochemically hydrogenated according to:

$$C_{60} + x H_2O + xe^{-} = C_{60}H_x + xOH^{-}$$

This ability suggests use of various film thicknesses of fullerenes (C_{60}/C_{70}) on various kinds of substrate as for anode and the cathode materials. Charge-discharge performance of these electrodes has been evaluated and showed a behavior that depends on the substrate and fullerene film thickness. Discharge capacity from 1600 mA.h/g, which corresponds to $C_{60}H_{48}$ hydrogenation, to full hydrogenation has been achieved. These new fullerene hydride electrodes demonstrated a very fast charging time lower than 40 minutes for full capacity. [51].

1.2.2 Gas Storage

Fullerene-based materials or hydrides have demonstrated economical, high storage and light weight abilities in gas storage, especially for hydrogen and oxygen. These days, hydrogen storage receives more attention due to its energy potential point of view.

For instance, the 30 double C-C bonds on each C_{60} molecule can be opened-up, for hydrogen storage, and re-closed reversibly for hydrogen gas release under particular conditions of temperature and pressure. Hydrogenated-fullerenes are thermodynamically more stable than fullerenes themselves. Thus, hydrogenation of C_{60} is theoretically favored under appropriate conditions [51].

The future of this application could be in hydrogen gas fuel cell for electric vehicles. For the time being, the development of these vehicles is limited by the current available hydrogen gas technologies, such as metal hydrides and cryogenic liquefied gas storage. For the case of metal hydrides, they are potentially hazardous, constitute high weight systems and provide low hydrogen storage densities. Cryogenic liquefied gas storage currently supplies the highest storage density but requires very high energy consumption. High capacity and environmentally safe potentials of fullerene-hydrides might power electrical cars and internal combustion engines [51].

On another point of view, fullerene-based materials were found to store oxygen at low pressure (less than 10 atm) to a significantly higher degree than sieves or zeolite, conventionally used materials for this purpose. At some point, fullerene-based materials

can easily separate oxygen from air in a gas-liquid adsorption process. These aptitudes may lead to development of a high density, low pressure room-temperature oxygen storage system for the medical, commercial and military sectors [51].

1.2.3 Diamond Precursor

Research [17][33][34] reported excellent diamond depositions and coatings using fullerene as source of carbon. Diamond is a material composed entirely of sp³-hybridized carbons giving a three-dimensional crystalline structure. Consequently, the partial sp³ bonding configuration of curved structure shape of fullerenes, as opposed to the planar shape of graphite (sp² bonding), highly contributes to the diamond precursor behavior [51].

1.2.4 Strengthening/hardening of materials

Unique characteristics of fullerenes, formally their small size (≈0.7 nm) and high reactivity emerge excellent metal and alloy strengthening opportunities. The higher reactivity of fullerenes over standard carbon stimulates in-situ interactions between fullerenes and metals, resulting generation of carbide particles. The small size of fullerene molecules simply allows an efficient dispersion strengthening of metallic matrices with these carbide dispersoids. Carbide dispersoids, of a given size of 1-5 µm, suggest a potential increase of several orders of magnitude in shear strength required for plastic deformation [51].

For instance, a <0.1 wt% fullerene additive in Ti-24.5Al-17Nb increases hardness by 30% and double yield strength while preserving ductility to moderate levels. A part strengthening, this in-situ carbide formation may bring investigating effects in materials such as improving electrical conductivity. The carbide dispersoids enhance the electrical conductivity by scavenging dissolved impurities and substitutional alloying components [51].

1.2.5 Optical Applications

Fullerenes displayed interesting optical properties such as optical limiting [18][48], large second harmonic response and an ultra-fast suppression of the second-harmonic generation (SHG) intensity [32][50].

The first property refers to a decrease in transmittance of a material with increased incident light intensity. In other word, the given material allows all light below a threshold value of activation to come in and a retransmission of this light at a constant level, which is below a defined damage threshold value. Therefore, this phenomenon gives rise to some future in eye and sensor protection applications [51].

The second and third characteristics, which refer to nonlinear optical properties, are due to delocalized π - conjugated electrons of the C_{60} molecule. As example, the usefulness of nonlinear optical response may be applied in systems involving conversion of light of frequency W to frequency 2W. The ultra fast suppression of SHG intensity happens when the fullerene film is simultaneously illuminated with a second light source, either pulsed or steady state. This may find future opportunities in optical computing and information processing [51].

Fullerenes has emission lines in UV spectra. This property may lead them to replace mercury in fluorescent tubes. This application on this radiation energy would be more than beneficial on the environment.

1.2.6 Sensor applications

The recent development of fullerene-based capacitors, solid-state sensors, was based on the electron accepting properties of fullerene films and high sensitivity occurring when planar molecules interact with the film surface. Fullerene film capacitors are very attractive for chemical sensors [51].

Previous studies on fullerene-based capacitors demonstrated a detection of less than 1 ppm H_2S in N_2 and sensitivity of water in isopropanol at a resolution of 40 ppm. These preliminary results just reveal a technological aim for fullerene chemical sensors [51].

Chapter 2: Literature Review

2.1: Overview of Fullerene Synthesis Methods

2.1.1 Vaporization of Graphite

The two most common methods of fullerene production using vaporization of graphite are resistive heating and arc discharge [15][21][22]. The second method results in a higher yield of fullerenes and is therefore used commercially for the production of fullerenes. Another alternative in the field of graphite vaporization is the production of fullerenes via harnessing sunlight, which uses renewable energy and was implemented by Smalley and co-workers at Rice University, Texas [5].

- 2.1.1.1 Arc Discharge Method

The arc discharge method for fullerene production uses an electric arc (dc or ac) to decompose graphite rods in a helium atmosphere. Figure 2.1 represents a typical arc discharge apparatus used by Hauffler and co-workers [21] at Rice University, Houston, Texas. The electrode system operates horizontally as shown in the schematic. A copper cylindrical reactor of 8 cm i.d., 15 cm long surrounded by a water-cooled jacket was used for soot collection. The graphite rod and disk are connected to an external ac (60 Hz) high current power source with copper clamps and two water-cooled vacuum current feedthroughs. The vaporization of graphite is accomplished by driving a 100-200 A current and a 10-20 V voltage between both electrodes. The spring tension is adjusted to determine the gap between both electrodes, which gives the freedom to control the process.

For operation, the system is held near 100 torr of helium. The plasma arc starts up by touching the two graphite electrodes together and then immediately moving them away to the required distance. At a certain degree of applied current, the power dissipation at the anodic rod results in the vaporization of graphite consuming up the anode while the cathodic graphite rod grows at its end due to condensation of carbon [15]. The temperature profile and the residence time of carbon clusters depend on the arc current,

pressure and type of buffer gas. The inter-electrode gap strongly influences the fraction of carbon transported from the anode to the cathode as well as the radiation level and heat exchange between the plasma and the surrounding arc gas [22]. It is believed that the intense light energy emitted from this plasma arc process may photochemically destroy potential fullerene cluster.

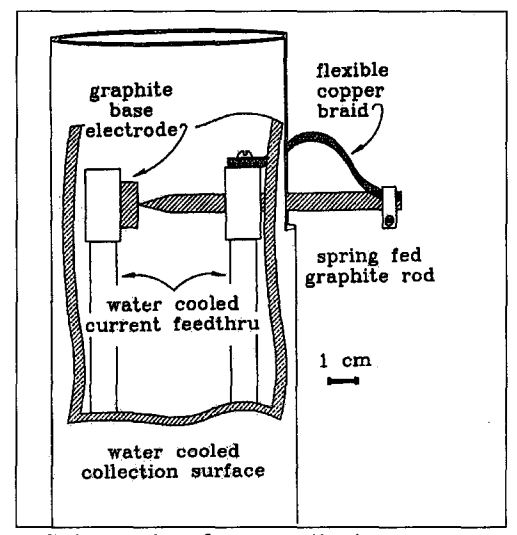


Figure 2.1: Schematic of an arc discharge generator [19]

Huczko and co-workers [22] used a setup similar to Figure 2.1 and optimized the following parameters: ac or dc feeding mode, input power, buffer gas, pressure, and electrode gaps. Their study led them to use electrode (6 mm in diameter) gaps between 0.5 and 4 mm for dc arcing, and to perform their tests in helium at 13.3 kPa. The fullerene content in the soot was determined by conventional spectrophotometric techniques. Table 2.1 shows the basic operating parameters. The erosion rate was kept constant at two levels for different electrode gaps by adjustment of the power input [22].

Table 2.1: Operating parameters of fullerene synthesis using the arc discharge method [22]

Expt no.	electrode gap (mm)	Current (A)	Voltage (V)	Input Power (W)	Carbon transport (wt.%)	Erosion rate (mg/s)
1	0.5	61.5	17.5	1085	53.7	3.1
2	1.0	65.0	18.0	1170	57.6	3.1
3	2.0	67.0	2.05	1375	51.6	3.1
4	3.0	73.0	21.5	1570	46.1	3.1
5	4.0	86.0	24.0	2065	39.3	3.1
6	0.5	65.5	19.0	1245	50.8	5.7
7_	1.0	67.0	20.0	1340	52.6	5.7
88_	2.0	76.0	21.0	1595	46.6	5.7
9	3.0	96.0	23.0	2210	42.9	5.7
10	4.0	131.0	26.5	3470	32.4	5.7

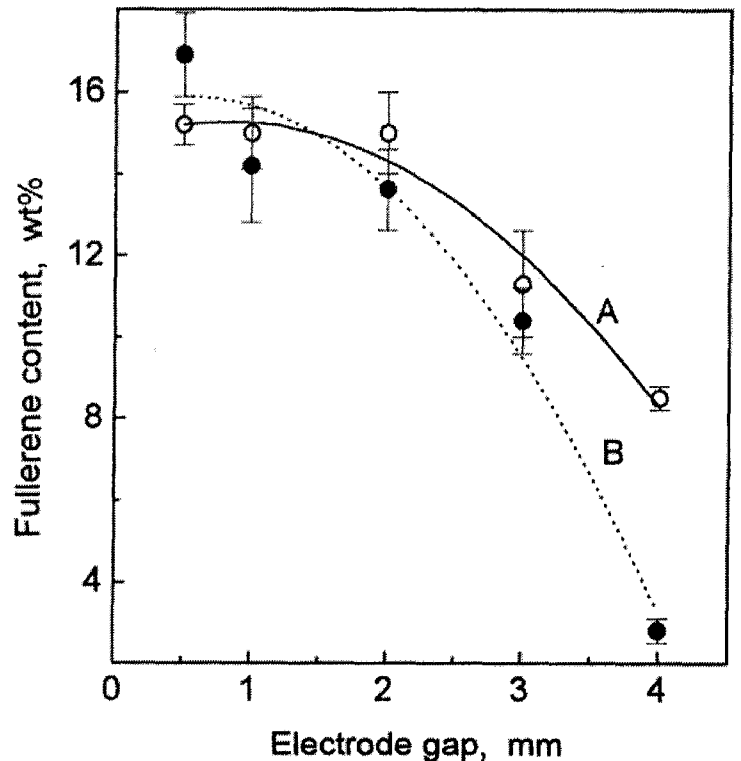


Figure 2.2: Fullerene content in collected soot vs. electrode gap. **A:** 3.1 mg/s anode erosion rate; **B:** 5.7 mg/s anode erosion rate [22]

From Table 2.1 and Figure 2.2, it may be seen that the fraction of carbon transport and the fullerene content in the soot steadily decrease with increasing the electrode gap despite equal graphite erosion rates. Huczko *et al.* [22] found that this decrease is not due to the

photochemical destruction of potential fullerene cluster. They explain that some pronounced expansion of carbon species into the surrounding space, and some strong sublimation and spallation of the anode material occur at high currents. The sublimation and spallation of the anode led to effective generation of graphite microcrystallites, which reduced the carbon availability for fullerenes [22].

In addition to synthesize fullerenes, the graphite arc with the co-evaporation of various elements, especially metals, produced interesting carbon nanomaterials. Huczko *et al.* [23] aim a new study to investigate the influence of transition metals, introduced into the carbon arc, on the plasma characteristics and on the formation of fullerenes and nanotubes. For this purpose, the authors performed dc arcing in the experimental setup described in Figure 2.1 with homogeneous graphite electrodes 6 mm in diameter and containing 0.6 wt.% of either Fe or Co-Ni metal mixture. These experiments were compared with those initiated with pure graphite electrodes. Fullerene yields associated to their operating conditions are shown in Table 2.2. The electrode gap and the anode sublimation rate were kept constant: within 1 mm and between 3 and 4 mg/s respectively.

Table 2.2: Operating parameters and C₆₀ yield comparisons in using different

electrode composition [23]

Electrode Composition	Pressure (kPa)	Current (A)	Voltage (V)	Input Power (W)	Sublimation rate (mg/s)	C ₆₀ Content (wt%)
С	8	74	19	1406	3.9	10.5
	40	71	23	1633	3.3	7.3
	80	64	29	1856	3.9	4.8
C-Fe	8	79	25	1975	3.3	4.4
	40	70	28	1960	2.9	4.5
	80	71	31	2201	3.6	6.4
C-Co/Ni	8	65	22	1430	4.2	5
	40	76	28	2128	3.6	4.5
	80	78	31	2418	3.3	5

The results shows that at low pressure, doped electrodes significantly reduced the yield of C_{60} , whereas the yield is independent of the electrode composition at higher pressures. The soot was also tested under LD TOF MS techniques for relative mass distribution

determination of higher fullerenes, mainly C₇₀, C₇₂, C₇₄ and C₈₀. The resulting mass spectra were normalized to the C₆₀ peak. As expected, the pure graphite electrodes demonstrated very low higher fullerene spectra. The Fe-doped electrodes showed a distinct enhancement for higher fullerene production, whereas a completely opposite effect was obtained with the Co-Ni-doped electrodes. The existence of higher fullerenes is nearly suppressed at the highest pressure of operation (80 kPa). Therefore, the authors concluded that Fe atoms or clusters might play a catalytic role in higher fullerene production [23].

Finally, the soot was analyzed by SEM and TEM for carbon nanotube investigation. Huczko *et al.* [23] noted that the resulting soot is more compact, much less dusty, and more cloth-like in using doped electrodes. Also, a weblike material was often produced in the discharge chamber. Arcing with the Fe-doped electrodes, carbon nanotubules were detected mostly in the weblike material surrounding the cathode deposit, while similar structure were found in both the chamber-deposited soot and webs. No nanotube was presented in the cathode core deposit [23].

- 2.1.1.2 Production via Harnessing Sunlight

Smalley and co-workers at Rice University constructed the harnessing sunlight method after previous experiments revealed that photochemistry might destroy potential fullerene clusters; a hypothesis that Huczko *et al.* [22] contradict. This method produces fullerenes by harnessing focused sunlight with a parabolic mirror onto the tip of a thin graphite rod to vaporize carbon. This seems contradictory because it exposes clusters to UV light. Although, sunlight is required to maintain the carbon as atoms or very small fragments, the vapor is carried away into a relatively dark area in order for clustering to occur [5].

The system operated for three hours in the Franklin Mountains in Texas, where the solar flux was 800 to 900 watts per squared meter, evaporating 5 mg of carbon. Analyzing the resulting soot, almost the complete fraction was C_{60} and C_{70} . The problem with this setup

is the lack of power flux. About 1000 watts per squared centimeter is needed to efficiently vaporize graphite [5].

The National Renewable Energy Laboratory (NREL), in Colorado, used a 10 kW high-flux solar furnace attaining the temperatures and the solar flux to efficiently vaporize carbon. In this device, it is reported that milligrams of carbon are vaporized in a matter of minutes. Also, the UV radiation is at least two orders of magnitude less than in arc discharge plasma and the carbon soot was formed only in zones of the apparatus that are not directly UV irradiated. This finding is consistent with Smalley's hypothesis, which stipulates that the transport of carbon vapor into a shadow zone is important to initiate fullerene formation [5].

2.1.2 Combustion of Hydrocarbons

Research conducted by a group at Massachusetts Institute of Technology [21] determined the effect of a series of parameters on the synthesis of fullerenes using premixed laminar flames of benzene and oxygen with argon as diluent. Burner pressure, carbon/oxygen ratio, residence time, and concentration of diluent gas were studied versus the production of C_{60} and C_{70} . The equipment used by MIT is a premixed laminar flame stabilized on a water-cooled burner. The burner operates at low-pressure between 1-3 hours and consists of a horizontal copper plate through which the gas mixture comes in the upward direction.

The largest yield of fullerenes was obtained (20% in the soot produced and only 0.26% of the carbon fed is transformed into fullerenes) using a pressure of 69 torr, a C/O ratio of 0.989 and dilution of 25% helium. The fullerene content in the soot ranged from 0.003% to 20%. Although this method achieves higher soot purity than obtained in the thermal plasma dissociation of C₂Cl₄ system (section 2.1.3) for instance, the combustion system represents a lower yield of fullerene when the fed carbon is taken as the basis of yield calculation. In thermal plasma dissociation of C₂Cl₄ method, up to 14.2% of the carbon fed is converted into fullerenes.

Chapter 2 Literature Review

In order to make the burner efficient and get the required temperature range, the C/O ratio needs to be minimized. However, large yield of fullerenes occurred when C/O ratio is maximized. Therefore, there is an upper limit in the C/O ratio, which restricted the fullerene yield using combustion of hydrocarbons.

2.1.3 Injection of Carbon Material into a Plasma Torch

- 2.1.3.1 Production via Dissociation of C₂Cl₄ (*Pyrogenesis* Process)

A new process for fullerene production was developed by Alexakis *et al.* [1][2] and is shown on Figure 2.3.

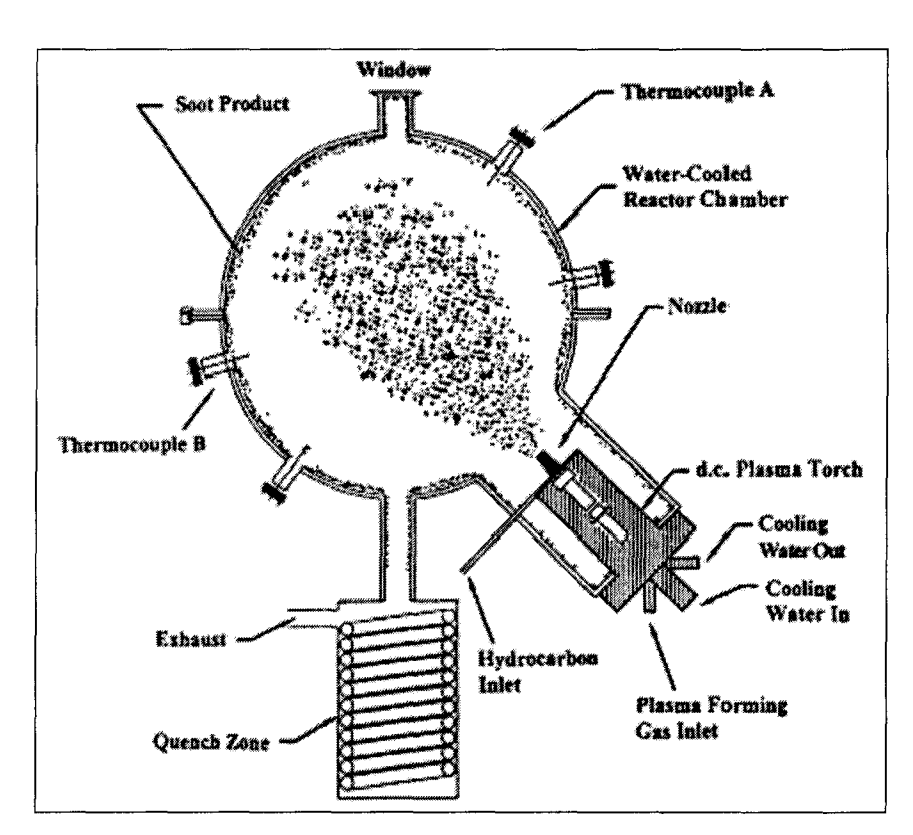


Figure 2.3: Pyrogenesis reactor system [1][2]

Alexakis [1] completed an in-depth study, where the system is under vacuum from 200 to 760 torr and helium, the plasma forming-gas, enters in the plasma torch at 110-225 slpm. The halogenated carbon gas (C₂Cl₄) at 0.15-0.54 mol/min is mixed with the helium carrier gas at 20 slpm and is fed into the plasma jet at the torch exit through a nozzle. The

Chapter 2 Literature Review

C₂Cl₄ molecules are dissociated in the plasma. Depending on the control parameters, some of the carbon atoms rearrange themselves into fullerenes, which condense with soot and other by-products on the water-cooled reactor wall. The gas leaving the reactor is quenched in a stainless steel receiving unit consisting of water-cooled coils, where additional soot condenses. Then, the gas is treated in an afterburner where halogenated compounds are combusted. Finally, the burner outlet gas is neutralized in a scrubber with caustic (solution of NaOH) [1].

A spherical geometry was chosen in order to try to maintain the temperature uniform in the reactor. However, the reactor resulted in a poor temperature control and in a strong limitation of the expansion of the fullerene formation temperature window (2200-2600K) given by McKinnon [31]. It is reported that increasing the torch power, the feed rate of C₂Cl₄ and running time increase simultaneously the temperature inside the reactor and the thickness of soot the layer on the reactor wall. The explanation given for this trend is that the accumulating soot on the reactor wall acts as an insulator. This temperature rise in the reactor affects the rate of fullerene soot deposition producing important fullerene losses by sublimation, and co-generation of chlorinated by-products [1]. A new cylindrical reactor design will bring a better wall temperature control and an optimized expansion of the fullerene formation temperature window.

A Computational Fluid Dynamics (CFD) model including the plasma zone and carbon condensation was made by Bilodeau *et al.* [6] for the C₂Cl₄-based *Pyrogenesis* reactor. Using the temperature window of 2200-2600K for fullerene formation, the residence time of the main stream was calculated. Table 2.3 summarizes the residence times and the obtained yields for the different operating conditions using Alexakis [1] reactor geometry.

Table 2.3: Theoretical estimation of residence time in 2200-2600 K zone and associated production yields [1]

Operati Conditi			Modeling Results	Experimental Results		
Power (kW)	C ₂ Cl ₄ feed rate (mol/min)	Pressure (torr)	Residence time in 2200- 2600 K (s)	Soot yield (g)	C ₆₀ yield (mg/mol C ₂ Cl ₄)	C ₇₀ yield (mg/mol C ₂ Cl ₄)
45	0.29	200	3.0×10^{-5}	9.8	215	35
55	0.29	200	9.1 x 10 ⁻⁵	13.1	350	85
65	0.29	200	14.1 x 10 ⁻⁵	14.2	420	115
65	0.15	200	19.0 x 10 ⁻⁵	13.6	510	105
65	0.29	200	14.1 x 10 ⁻⁵	14.2	420	115
65	0.44	200	7.9 x 10 ⁻⁵	14.8	350	105
65	0.54	200	6.6 x 10 ⁻⁵	14.1	300	105
65	0.29	200	7.9×10^{-5}	14.0	500	100
65	0.29	300	9.9×10^{-5}	16.0	500	120
65	0.29	400	n/a	12.0	250	50

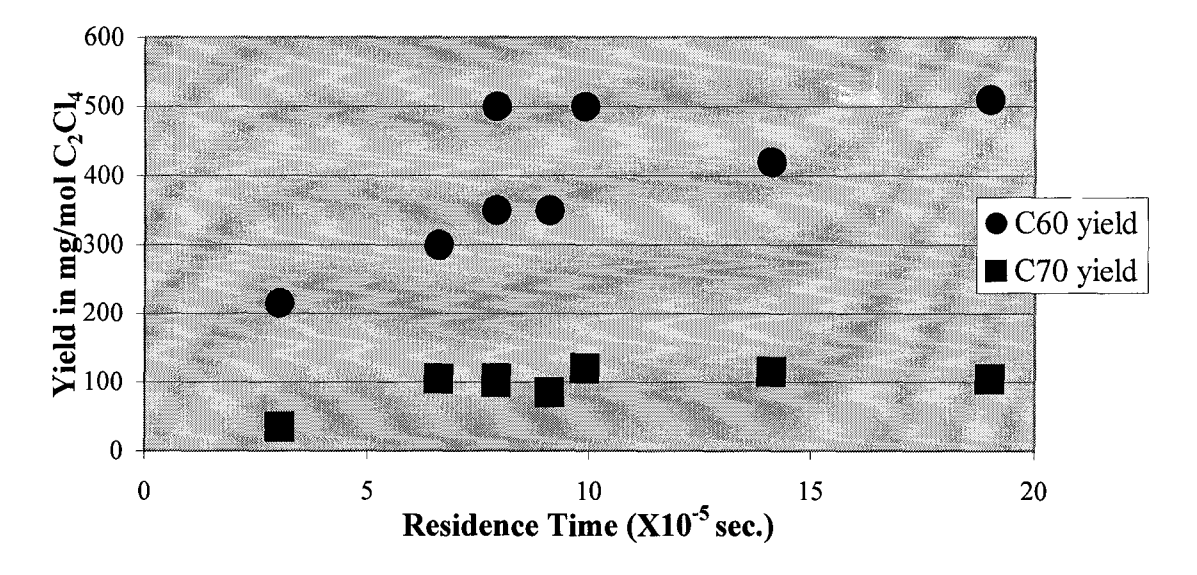


Figure 2.4: Experimental yield versus theoretical residence time

According to Table 2.3 and Figure 2.4, C_{60} yield is increasing with a larger residence time, while the C_{70} yield remains approximately constant. As a guideline, a complete dissociation reaction will produce 24 g/mol C_2Cl_4 of both C_{60} and C_{70} in a full conversion efficiency mode. According to the data in Table 2.3, the conversion percentage of C_2Cl_4 into fullerenes roughly lies between 0.5% and 2.0%. Decreasing the torch operating

Chapter 2 Literature Review

power from 65 kW to 55 kW and 45 kW considerably reduces the yield of soot, C₆₀ and C₇₀. It also suggests that a torch operating power below 55 kW is not appropriate to maintain the temperature profile required for the *Pyrogenesis* process. An increase of the torch power above 55 kW improves both the amount of soot produced and concentration of fullerenes in the bulk.

At 55 kW and 65 kW, the soot yield was approximately constant at 12 grams per mole of C₂Cl₄ fed as the C₂Cl₄ feed rate increases from 0.15 mol/min to 0.54 mol/min, whereas at 45 kW, the soot yield dropped to 7 grams per mole C₂Cl₄. At 55 kW, the overall yield of C₆₀ decreases with increasing C₂Cl₄ feed rate (Figure 2.5A), while C₇₀ yield increases steadily (Figure 2.5B). Operating at 65 kW, C₆₀ yield decreases with C₂Cl₄ feed rate (Figure 2.5A), whereas C₇₀ yield remains constant at 100 mg/mol C₂Cl₄ (Figure 2.5B) [1].

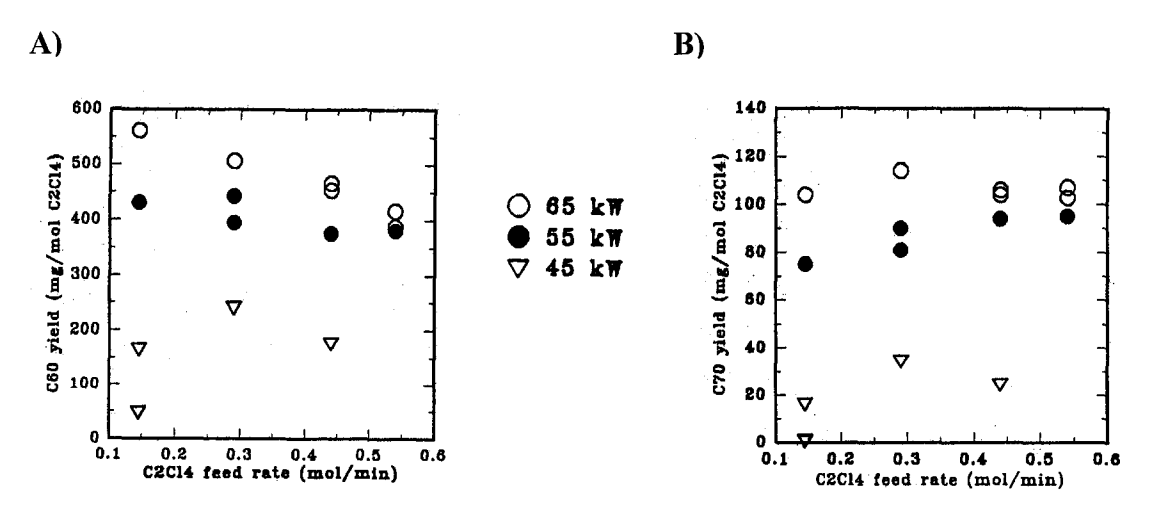


Figure 2.5: Overall C_{60} (**A**) and C_{70} (**B**) yields as a function of C_2Cl_4 feed and torch power level [200 torr] [1]

In addition, an increase of the operating pressure decreases the production rate of fullerenes. Higher pressures decrease the reactor temperature, which in turn favor the formation of small-chlorinated species. Also, higher pressure may affect the mixing of C_2Cl_4 with the plasma, resulting in incomplete pyrolysis or in the formation of small-chlorinated compounds.

Chapter 2 Literature Review

The variations in soot collection rate and soot composition as a function of run duration were studied. For this purpose, the torch power, C_2Cl_4 feed rate and pressure were fixed at 55 kW, 0.29 mol/min, and 200 Torr, respectively. The experiments show that the average soot collection rate becomes constant at 3.2 g/min in the reactor and 0.7 g/min in the cooling unit after 2 minutes. The overall C_{60} collection rate increases up to about 110 mg/min in 2 minutes at which point the collection rate remains constant until 6 minutes (Figure 2.6A). After 6 minutes, the overall C_{60} collection start to decrease showing an average collection rate of about 100 mg/min for a 8 minutes run. The overall C_{70} collection rate increases rapidly to 25 mg/min during the first 4 minutes (Figure 2.6B). For the next 4 minutes, the author was not able determine if the overall C_{70} collection rate remains constant at about 27 mg/min or slightly increases from 25 to 30 mg/min. Getting hotter reactor temperatures with run duration, a slight increase of C_{70} collection rate would suggest that higher reactor temperatures favor C_{70} formation.

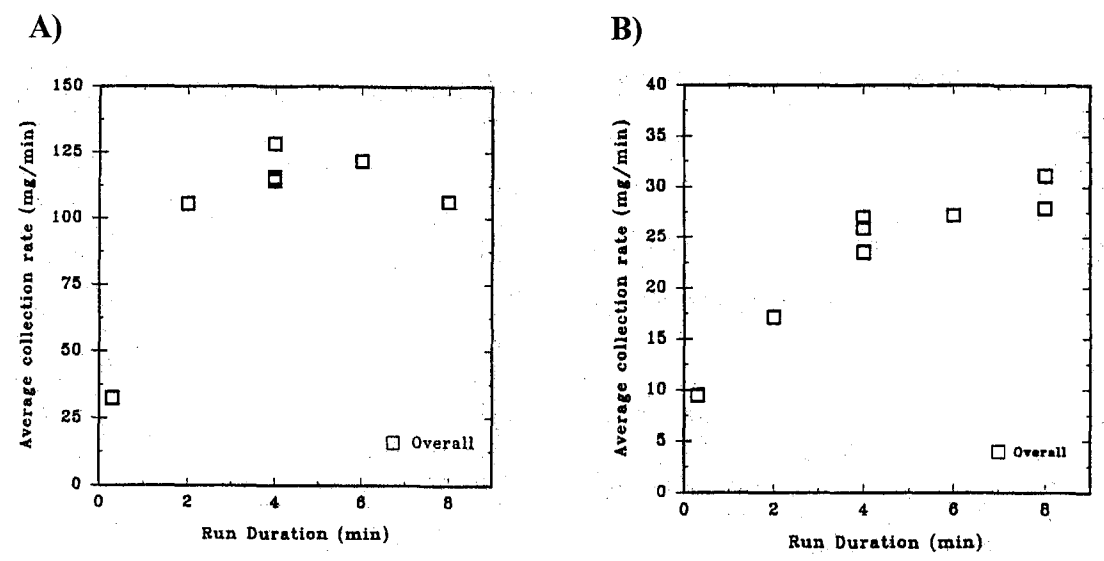


Figure 2.6: Overall C_{60} (**A**) and C_{70} (**B**) collection rate as a function of run duration [55 kW, 0.29 mol/min C_2Cl_4 , 200 torr] [1]

For short runs, analysis showed that more than 50% of the soot in the reactor consisted of chlorinated by-products, whereas in longer runs, the concentration of these by-products in the soot collected dropped to 10%. In short runs, the relatively low reactor temperature induces a lower residence time of the carbon species in high temperature zone than in

longer runs. For long run duration, the higher reactor temperatures are expected to favor formation of graphitic networks [1].

- 2.1.3.2 Microwave Synthesis from Chloroform

This process is an extrapolation of the *Pyrogenesis* process with the introduction of 250 W microwave to the plasma torch along square wave-conduct pipe. The carbon source, chloroform, in an argon atmosphere vaporizes into the quartz column reactor (Figure 2.7) through the plasma torch. Vacuum pressure, microwave energy, gas flow rate were the investigated parameters for fullerenes production [52].

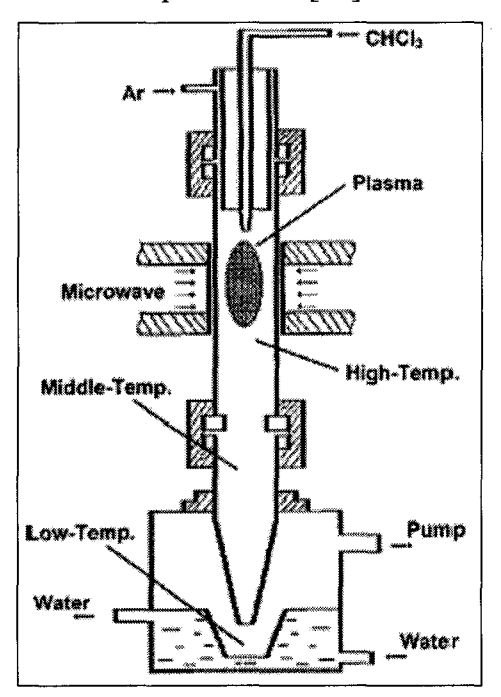


Figure 2.7: Microwave fullerene synthesis system [52]

It is reported that a vacuum pressure below than 0.01 MPa cannot maintain the plasma. However, an increase of the argon flow rate could help to maintain the flame, but reducing the yield of products. An argon flow rate higher than 350 ml/min resulted in an unstable plasma jet. An increase in the carbon feed rate disturbed the plasma by depositing soot on the wall of plasma zone. To attempt to solve the latter problem, argon could be introduced on the side of the plasma torch to sweep the soot out of the plasma zone. Finally, any increases in microwave energy increase the fullerenes yields [52]. Xie

Chapter 2 Literature Review

et al. [52] focused on evaluating dependence of fullerene formation versus temperature and collision probability. According to the temperature difference in the reactor, soot was collected separately at high-, middle- and low-temperature zone, shown on Figure 2.7, and analyzed for quantification.

Table 2.4: Yields of C_{60} and C_{70} according to temperature zone in the reactor [52]

Reaction atmosphere							
Zone	C ₆₀ (%)	C ₇₀ (%)	C ₇₀ /C ₆₀ (%)	Temperature gradient	Collision probability		
High-T	1.1	0.3	28.6	Small	Intensive		
Middle-T	0.3	0.1	39.2	Middle	Middle		
Low-T	1.3	0.2	19.9	Small	Middle		

Table 2.4 suggests that temperature gradient and collision probability have a greater effect on fullerene formation than temperature itself. Small temperature gradient and intensive collision probability seem to help the production of fullerenes.

- 2.1.3.3 Production via the Dissociation of Mixtures of Carbon Sources and Metallic Catalyst

In this study, the objective was to synthesis carbon nanotubes. A method based on the evaporation of carbon and catalyst using a H.F. induction plasma torch, as source of energy to activate the precursor species is proposed. Mixtures of acetylene-catalyst and carbon black-catalyst are used as source of raw materials. The authors relate an efficient synthesis of carbon nanostructures to some significant chemical and physical phenomena involved in the method: 1) the production of the carbon vapor and the metal vapor catalyst generated into the plasma, 2) the chemical and physical evolution of the carbon and catalyst species into the reactor, and 3) the different reactor zones, which are characterized by specific temperatures, residence times, species density, and species transport throughout the different temperature gradients [11].

Experiments were carried out in experimental setup shown on Figure 2.8. The H.F. induction plasma torch possesses a quartz confinement tube of 50 mm i.d. and 4-turns coil

Chapter 2 Literature Review

was used to vaporize the mixtures of raw materials. The maximum power was up to 60 kW with an oscillator frequency of 2 to 5 MHz. The whole experimental setup (Figure 2.8) is surrounded by a water-cooled jacket and is divided into two section: 1) the reactor (150 mm i.d., 500 mm long) and the quenching zone (130 mm i.d., 500 mm long), and 2) the filtration system, which includes a cyclone and two stainless steel filters (38 mm o.d., 350 mm long) [11]. The system allowed the control of the operating parameters. For instance, electrical power, the reactor pressure, the carbon and catalyst feed rate, the carbon-catalyst percent ratio, and the type of plasma gas are among the monitored parameters. In the results presented, the plasma torch was run under the following fixed gas flow rates and electrical power, and the reactor pressure was maintained 66 kPa.

Central Gas:

30 slpm Ar

Sheath Gas:

120 slpm He

Powder Gas:

8 slpm He

Electrical Power:

40 kW

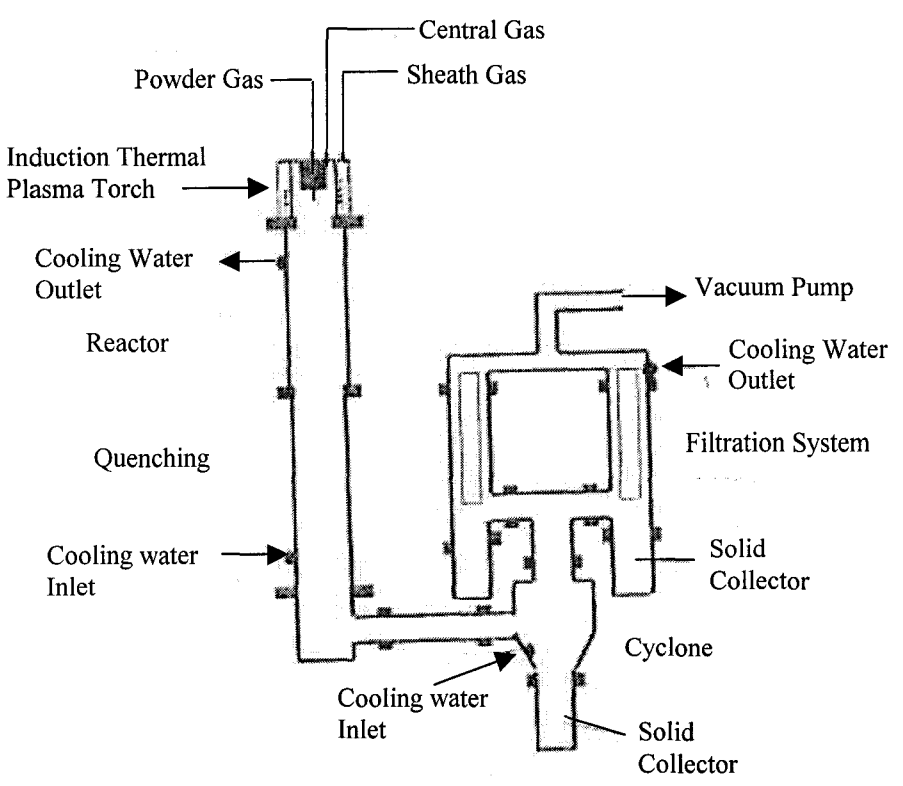


Figure 2.8: Cota-Sánchez et al. experimental Setup [11]

Three kinds of gas flow were introduced into the plasma torch: the sheath gas protecting the quartz tube from hot plasma, the central gas as the plasma forming gas and, the carrier gas introducing solid and liquid materials into the plasma.

Experiments were performed under two different test sets: 1) mixtures of acetylene-iron and acetylene-nickel-cobalt and 2) mixture of carbon black BP 3700-iron were studied as starting material.

Preliminary tests were done without feeding raw material in order to evaluate the effect of the plasma on the catalyst. The authors speculated an increase in the catalyst's specific surface after the plasma treatment. Normally, iron passes from 0.9 to 16.2 m²/g whereas nickel specific surface increases from 0.6 to 15.1 m²/g [11].

C₆₀ seemed more likely to be produced under the presence of iron. Mixtures of iron-C₂H₂ and iron-black carbon as raw materials generated soot up to 3.9% fullerene content whereas mixtures C₂H₂-Nickel-Cobalt did not generate any trace of fullerenes. The authors correlate this result with the specific surface and the Body Centered Cubic (BCC) structure of iron due to their role in the contact and the reaction sensitivity between the catalyst and the reactants [11]. The lack of carbon nanotubes is attributed to the size of catalyst used (>5 μm). According to Cota-Sánchez *et al.* [11], previous research demonstrated that large catalyst particles (>20 nm) favor formation of carbon nanofibres and nanoparticles, conversely, smaller catalyst (<20 nm) improve the yield performance of carbon nanotubes.

Wang *et al.* [49] performed a similar study by using C-Si mixed particles fed in an induction thermal plasma torch. This torch consists of a quartz confinement of 80 mm i.d. with a 3-turns coil to vaporize the raw materials. A 1.67 MHz oscillator supplied power with a maximum capacity up to 200 kW.

Chapter 2 Literature Review

Experiments were all carried out at 5 g/min C-Si feed rate and 30 kW torch power using two kinds of gas compositions: pure Ar and He/Ar mixture. The authors affirm that argon is suitable for keeping the plasma stability and helium was selected according to the previous results obtained with vacuum arc system. Reactor pressure, carrier gas and sheath gas conditions were the varied parameters [49].

Table 2.5: Wang et al., [49] experimental conditions

Test	Pressure	Pressure Carrier gas		Sheath gas (l/min)		
No.	(Torr)	(l/min)	Axial	Swirl		
1	150	Ar: 10	Ar: 70	Ar: 30		
2	150	He: 10	He: 70	Ar: 30		
3	380	He: 10	He: 70	Ar: 30		
4	500	He: 10	He: 70	Ar: 30		

Time of Flight Mass Spectrometer (TFMS) recognized the formation of C60 and C70 as well as higher fullerenes. TFMS outputs suggest that condition #2 (Table 2.5) synthesizes the highest purity soot and has a good scale up potential for nanotube production. In addition, these results were put into relation with Swan band (C₂) intensity. A high C₂ molecular spectra intensity in the high temperature zone of the plasma jet stimulates an efficient production of fullerenes [49].

2.2: Mechanisms of Formation

Theories on the mechanisms of formation of fullerenes have evolved since the two basic speculated models proposed by Goeres and Sedlmayr in 1991 [16], and by Smalley [44] and Heath in 1992 [20]. Those mechanisms were based on the graphite vaporization process and involve the ablation of a graphite single sheet followed by ring rearrangement leading to cage closure. Smalley [44] and Heath [20] hold that fullerene formation occurs through a series of polycyclic aromatic intermediates consisting of 5 rings and 6 rings positioned to maximize the number of nonadjacent 5 rings while minimizing the number of unsatisfied valences. The pentagons allow curling the fullerene intermediate and enabling to join some peripheral bonds. Clusters containing unsatisfied valences will react with carbon atoms and clusters until the achievement of a relatively stable closed

Chapter 2 Literature Review

fullerene structure [20][44]. Goeres and Sedlmayr [16] also consider polycyclic aromatic intermediates and describe fullerene formation via polymerization of C₁₀ carbon chain. The latter tends to form monocyclic rings reacting and collapsing to form naphthalenoctyl structures. Then, this type of structure favors the connection of pentagons that produces the curvature of the intermediates [16]. Recent research however demonstrated that the formation of fullerenes is initiated by one specific molecule: a precursor. Despite all of the research in defining the mechanism of fullerene formation, no conventional formation pathway has been fixed.

Among the different proposals, Hunter *et al.* [24] suggests that the formation of fullerenes pass trough a two six-membered rings with a spiraling polyyne chain as precursor. A series of radical-induced closures occurs with both ends of the polyyne chain zipping up to an icosahedral C₆₀. Strout *et al.* [45] argues that long bicyclic rings, which are called cycloadducts, give a lower energy road to fullerenes. Cycloadducts undergo a sequence of cyclizations that result a carbon "hoop" as fullerene intermediate. The "hoop" follows a series of carbon shifts to form new pentagons or hexagons in order to close the "hoop" and yield to fullerene.

Researchers from Auburn University, Alabama [9] and from the Massachusetts Institute of Technology [27][36] studied curved polycyclic aromatic hydrocarbons (PAH) as fullerene precursors in combustion of hydrocarbons. Every soot component was analyzed to construct a kinetic mechanism for the formation of fullerenes.

Both groups propose a simple series of C_2H_2 addition to the growing molecule, where corannulene ($C_{20}H_{10}$) is involved as a precursor. This model, inspired from works done by Smalley [44] and Heath [20], is commonly called the *Direct Pathway* [39].

The mechanism starts from the conversion of a C_{16} fragment. Ring closure and cyclization are imposed to the C_{16} chain. Addition of two C_2 molecules leads to the fullerene precursor, $C_{20}H_{10}$. From C_{16} to C_{60} , the future fullerene molecule bonds itself to

Chapter 2 Literature Review

 C_2 generating intermediates with 10 free valences [9] rearranging to incorporate pentagons as well as hexagons in the bonding pattern. The C_{50} cluster (Figure 2.9, step 7) can yield two open C_{60} (Figure 2.9, step 8) and (Figure 2.9, step 10). The cluster in step 10 can rearrange itself as in step 8 and cyclizes to form fullerenes or alternatively, can grow by C_2 addition to yield to C_{70} [9].

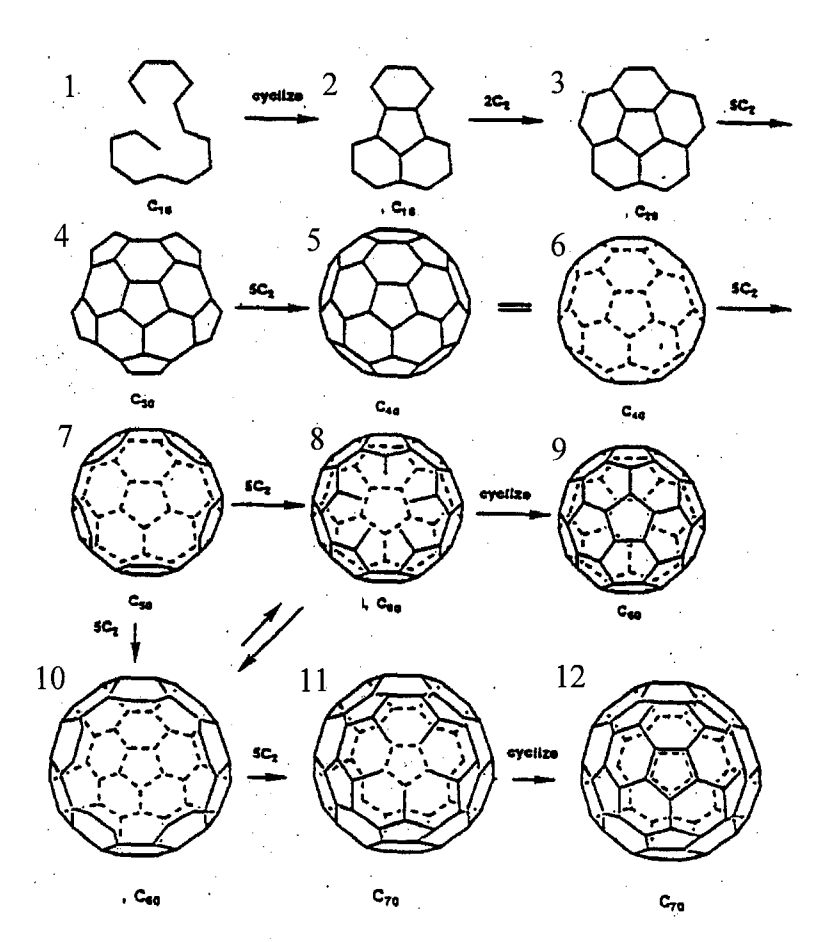


Figure 2.9: Formation of C_{60} and C_{70} via the *Direct Pathway* [9]

Chapter 3: Experimental

3.1: Apparatus and Instrumentation

3.1.1 Reactor Assembly Process Description

Fullerenes are synthesized using a plasma torch based on the dissociation of tetrachloroethylene (C₂Cl₄) as described in section 2.1.3. The new water-cooled reactor shown on Figure 3.1 was designed in stainless steel with a cylindrical geometry (ID=40 cm) and the flexibility to modify the length of the expanding plasma flame with a movable water-cooled disk plate (ID=36 cm) up to a possible total reactor length of L=100 cm. A quartz window provides optical access to the plasma jet for spectroscopy measurements. A non-transferred D.C. plasma torch operated between 45 and 65 kW is used for the dissociation of C₂Cl₄. C₂Cl₄ is injected at flow rates of 0.15-0.54 mol/min at a temperature of 200°C \pm 10°C with 20 slpm of carrier gas helium. Helium is also used as the plasma forming gas at 225 slpm. The operating pressure inside the reactor is set at a value between 200 and 300 torr and is controlled manually with a water-sealed vacuum pump and a globe valve. The gas leaving the reactor passes through a cooling unit consisting of copper water-cooled coils surrounded by a stainless steel water-cooled jacket, where the remaining products are condensed before entering the vacuum pump. The chlorinated exhaust from the pump is treated through a packed column in which an alkaline solution shower absorbs the chlorine gas. High Performance Liquid Chromatography (HPLC) is used for the quantification of fullerenes in the soot. Figure 3.2 shows the overall production system.

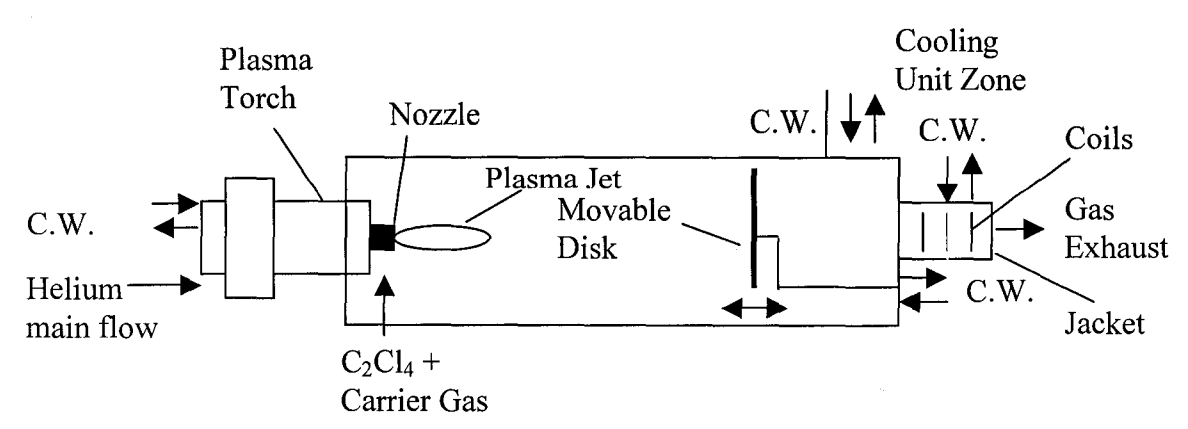


Figure 3.1: New reactor assembly (C.W.=cooling water)

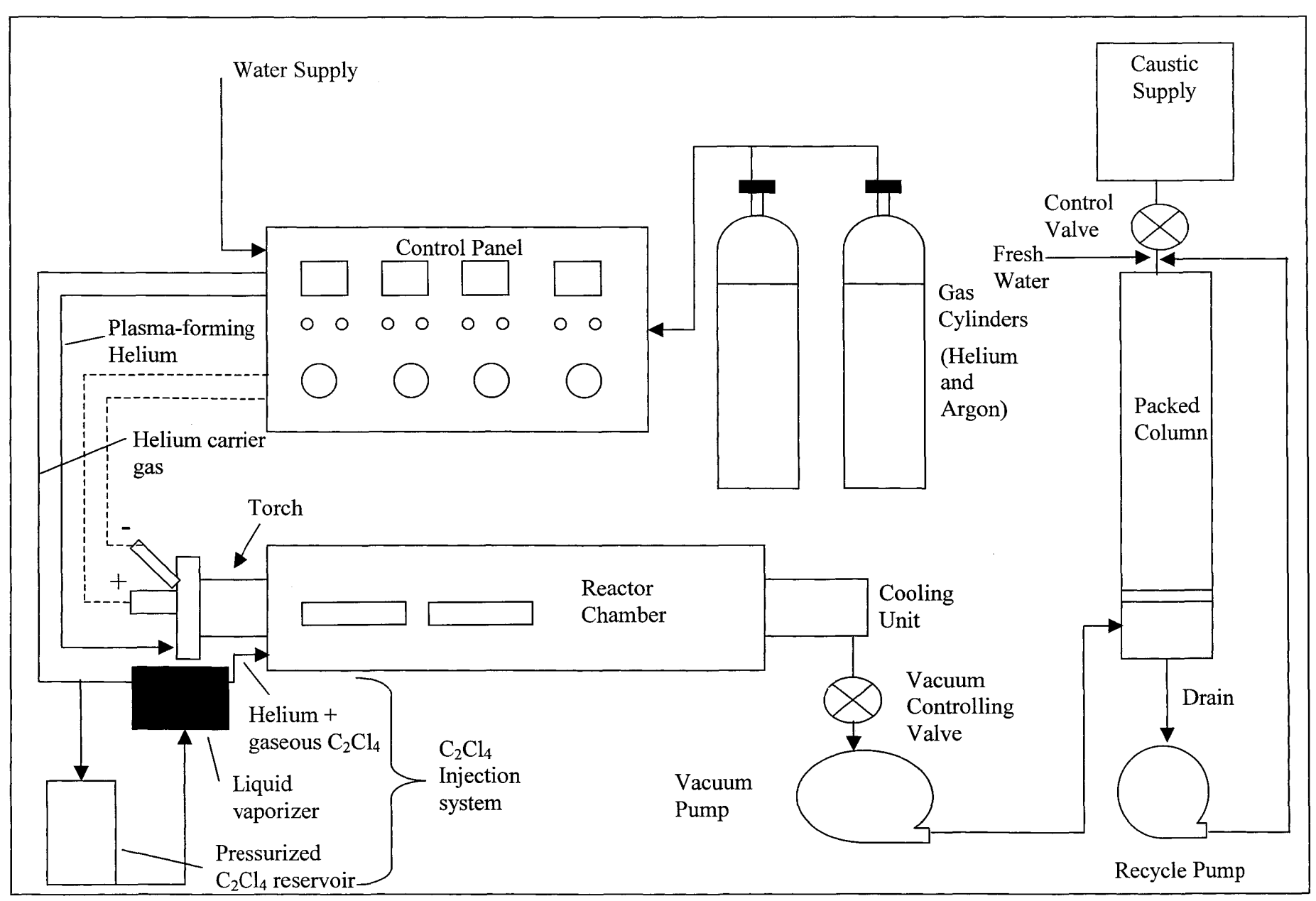


Figure 3.2: Schematic of the overall fullerene soot production

Chapter 3 Experimental

3.1.2 Plasma Torch System

C₂Cl₄ gas was dissociated in a non-transferred D.C. plasma torch, machined by *Pyrogenesis Inc* (RPT2 model) featuring a maximum power of 100 kW. Figure 3.3 presents a cross-sectional overview of the plasma torch. The carbon source was injected through the plasma exit nozzle made of thoriated tungsten (ThO₂W). The plasma was generated using electrodes also made of ThO₂W. Compared to conventional systems, these electrodes were set in reverse polarity, where the cathode was located at the torch exit. The plasma-forming gas was introduced through a perforated annular ring (vortex generator), installed between both electrodes in order to aerodynamically stabilize the arc. The overall torch body and the electrodes were water-cooled using a flow of 22 lpm.

The plasma jet was controlled through a console digitally displaying arc voltage, current, plasma-forming gas flow, reactor pressure, cooling-water inlet and outlet temperatures, and flow. Data given by these thermocouples and flow meter were necessary to determine the torch efficiency. The torch power was set by varying the arc current manifold from a rectifier connected to the console. A high-frequency generator was provided for arc ignition. The plasma-forming gas flow was controlled by a Tylan (0-300 slpm He) Mass Flow Controller (MFC). A MKS Baratron pressure transducer monitored the reactor pressure. Series of relays are connected to the plasma-forming gas flow meter, inlet and outlet cooling water thermocouples and, cooling water flow meter in order to secure the plasma torch components. If one these operating data is not situated in the plasma torch defined specs (Table 3.1), the relay associated to the given reading automatically shut down the torch.

Table 3.1: Pyrogenesis RPT2 plasma torch operating parameters specs

Torch Operating Parameters Specs	Values
Plasma-Forming Gas Flow	≥ 75 slpm Helium
Cooling Water Inlet Temperature	≤ 30°C
Cooling Water Outlet Temperature	≤ 50°C
Cooling Water Flow	≥ 20 lpm

31

Chapter 3 Experimental

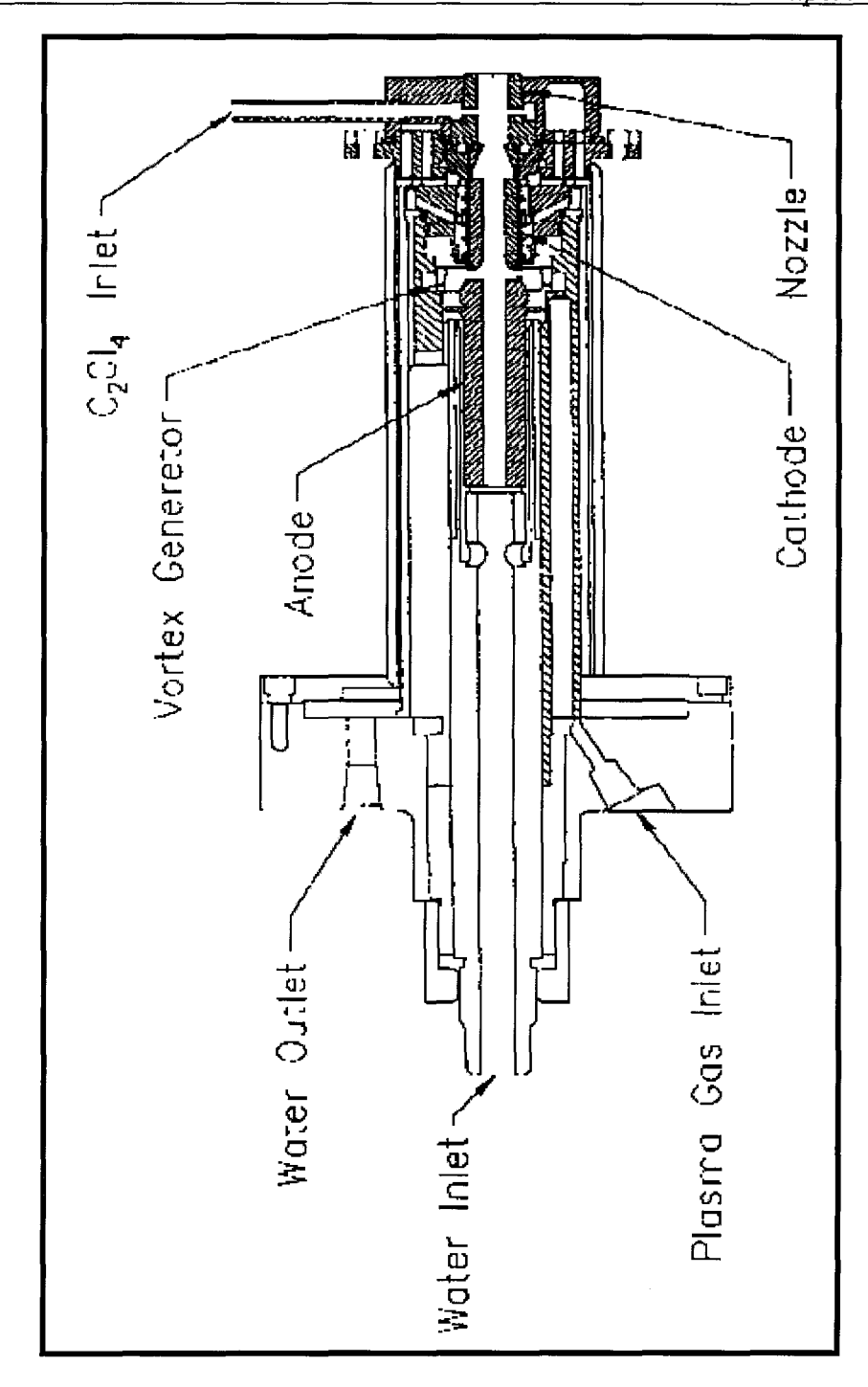


Figure 3.3: Cross-sectional view of the plasma torch (*Pyrogenesis* RPT2 model)

3.1.3 Leak Detection

Vacuum leak detection was performed before the purchase of the data acquisition system. A strip chart recorder connected to the MKS Baratron output was employed to monitor the pressure evolution of the closed vessel under vacuum.

3.1.4 Real-Time Temperature Acquisition

For real-time temperature acquisition of the system cooling water, Type K thermocouples were connected to a ComputerBoard data acquisition system, consisting of a plug and play DAS-08 board with a CIO EXP-16 multiplexer controlled by Softwire software.

Since temperature measurements will be done inside the reactor and a multiplexer accepts only one type of thermocouple at a time, Type K thermocouples were selected due to their large range of measurements.

To calculate the cooling efficiency of the reactor, these thermocouples were installed at the inlet and outlet of the reactor, movable disk, cooling coils and cooling jacket. Cooling water flow was given by rotameters placed at the water inlet of these key-cooling sites.

3.1.5 Power Supply

The non-transferred D.C. plasma torch power was supplied by eight 400-Ampere Miller power supply units connected in series giving the following specifications:

• Open-circuit voltage: 600 V

• Maximum current: 525 A (325 A @ 100% duty cycle¹)

• Maximum power: 78 kW (@ 100% duty cycle: 240 V, 325)

The overall setup was well grounded during torch operation.

3.1.6 C₂Cl₄ Injection System

The injection system consist of the following components:

- a pressurized liquid C₂Cl₄ reservoir
- two rotameters
- a liquid vaporizer
- a heated helium line for carrier gas
- a heated and insulated line injecting the mixture of C₂Cl₄ and carrier gas

¹ Duty cycle: It is the percentage of a ten minute period that the power source can be operated at a given output without overheating and damage of the unit.

Chapter 3 Experimental

• two temperature controllers stabilizing temperature of the carrier gas and the injected mixture lines.

C₂Cl₄ was delivered to the liquid vaporizer through a rotameter maintained at a flow rate from 15 to 54 ml/min. A pressurized reservoir containing the C₂Cl₄ was made of a stainless steel cylindrical tank of 10 cm i.d. and a capacity of 2 L for C₂Cl₄. Helium pressure at 100 psig (690 kPa) was applied to the top of the reservoir to allow pumping of C₂Cl₄ towards the vaporizer in a preheated and insulated ¼" i.d. (6.35 mm) stainless steel duct. The liquid vaporizer was another cylindrical stainless steel container of 10 cm i.d. and 10 cm high sitting on a hot plate.

The C_2Cl_4 vapors were collected in the vaporizer and then fed to the torch nozzle using a carrier gas. The latter was a heated 20 slpm helium flow, regulate with a rotameter, at 100 psig (690 kPa) and was controlled at $150 \pm 5^{\circ}C$ prior its input into the vaporizer. The mixture of gaseous C_2Cl_4 and helium was ejected then from the top of the vaporizer in a heated $\frac{1}{4}$ " i.d. (6.35 mm) stainless steel duct towards the torch nozzle. The mixture was injected in the torch at a maintained temperature of $200 \pm 10^{\circ}C$.

3.1.7 Vacuum System

A 5 hp Kinney liquid ring Vacuum Pump (KLRC-75), coupled with a globe valve, was used to manually control the pressure of the reaction chamber from 100 to 760 torr. City water was regulated at 5 gpm (19 lpm) for vacuum sealing. An oil sealed pump was not opted to prevent dissolution and clog up of possible remaining materials.

Also, a mechanical Ruvac E116-S25 double-stage root blower/centrifugal vacuum pump (*Leybold Inc.*) was connected in parallel for preliminary vacuum evacuation of the reaction chamber. This step was done before performing an experiment to eliminate the maximum amount of air contaminants and condensed humidity by the cooled walls. Hydrogen, nitrogen and oxygen encourage production of by-products and reduce carbon availability for fullerene production.

3.1.8 Exhaust Gas Neutralizing System

A 12' high packed-column of 10 cm i.d. was erected to neutralize chlorine gas (Cl₂) from the vacuum pump off-gas stream. Column height and diameter were designed according to Perry's Chemical Engineering Handbook [38] for ceramic saddles packing (25 mm). Chlorine gas reacts with alkaline solution, yielding to a salt. Therefore, a shower of 50% NaOH was chosen as alkaline solution reactant. For simplicity of operation, it was decided to operate the column in a close-circulation loop of NaOH driven by an alkaline proof liquid pump (Little Giant ¾ hp). The column gas outlet was exhausted into the laboratory fume hood.

3.2: Extraction and Purification of Fullerenes

3.2.1 Laboratory Equipment and Instrumentation

During the extraction and purification of fullerenes, the following equipment and instruments were used:

- a Bransonic 8210R-MT (VMR Scientific) ultrasonic bath, for promoting mixing of the soot particles with toluene during the extraction process;
- a vacuum filtration setup, using Celite 521 [Aldrich] as filtering agent, for removal of insoluble particles in toluene.
- a Caframo VV2000 rotary evaporator, for the evaporation of solvents;
- a standard glass chromatography column (3.8 cm ID) with pressure adapter, for the purification of fullerenes;
- a high vacuum manifold (10⁻³ torr), equipped with a Balzers Rotary Vane Pump, for drying solid samples in analytical work;
- a Mettler AE200 analytical balance having a precision of 0.1 mg and accuracy of ±0.3 mg; used for measuring the weight of samples.

3.2.2 Quantification of Fullerenes

Dissolved fullerene extract in toluene was injected in a High Performance Liquid Chromatography (HPLC) system, which consisted of a Waters 600EP multisolvent

Chapter 3 Experimental

system with a UV/VIS detector. A computer running with Millennium 2000 software controlled and monitored HPLC operating conditions, and sampled results.

3.3: Optical Setup

In view of the importance of residence time of the gaseous precursors in a specific temperature zone, a spectroscopic study was conducted for experimental temperature profiling of the plasma tailflame within the reactor. The setup used to acquire emissivities from the different plasma components is shown on Figure 3.4. The lens was installed at a distance of 2f of the plasma jet giving an inverted reproduction in real size (enlargement of -1) of the discharged image on a 200 microns optical fiber, f (=30 cm) being the focal length of the lens. The optical fiber was mounted on an optical bench equipped with micrometric screws permitting lateral displacements for data acquisitions along the vertical and the horizontal axis. A He-Ne laser having a specific wavelength of 632.8 nm was employed to align the overall optical system with the plasma torch. The light emissions from the plasma were sent through the optical fiber toward a Jobin Yvon THR1000 monochromator, featuring 1 m focal distance. The function of the monochromator is to isolate radiation of the desired wavelength from the rest of the other radiations coming from the emitting source.

The monochromator system includes two major components: the slits, one for entrance and one for exit, and the dispersion element. The entrance slit (Figure 3.4) essentially controls resolution of the entering radiation from the studied light source and allows the latter to reach the dispersion element. The entrance slit also prevents external system radiations, such as room light, windows, etc., from traveling down the light path. A step-by-step motor controlled by Winspec software from *Princeton* on a PC computer operated the rotation of the diffraction grating, necessary for the adjustment of the wavelength. Placed after the dispersion element, the exit slit permits only radiation of the desired wavelength to be collected by the detector [40]. The entrance and exit slits are adjusted in height and width by a micrometric screw.

Chapter 3 Experimental

The isolated spectral lines are detected at the exit slit using CCD (Charge-Coupled-Device) linear array photodiode (1024 pixels; 12 Å/pixel) manufactured by *Princeton Instruments*. CCD photodiodes provide a way to detect analog electrical signals from a visible scene and shift it into a digital data [3]. The actual linear array photodiode features an electromagnetic obturator controlled numerically by the Winspec software from *Princeton* that allows to fix the exposure time of the cell.

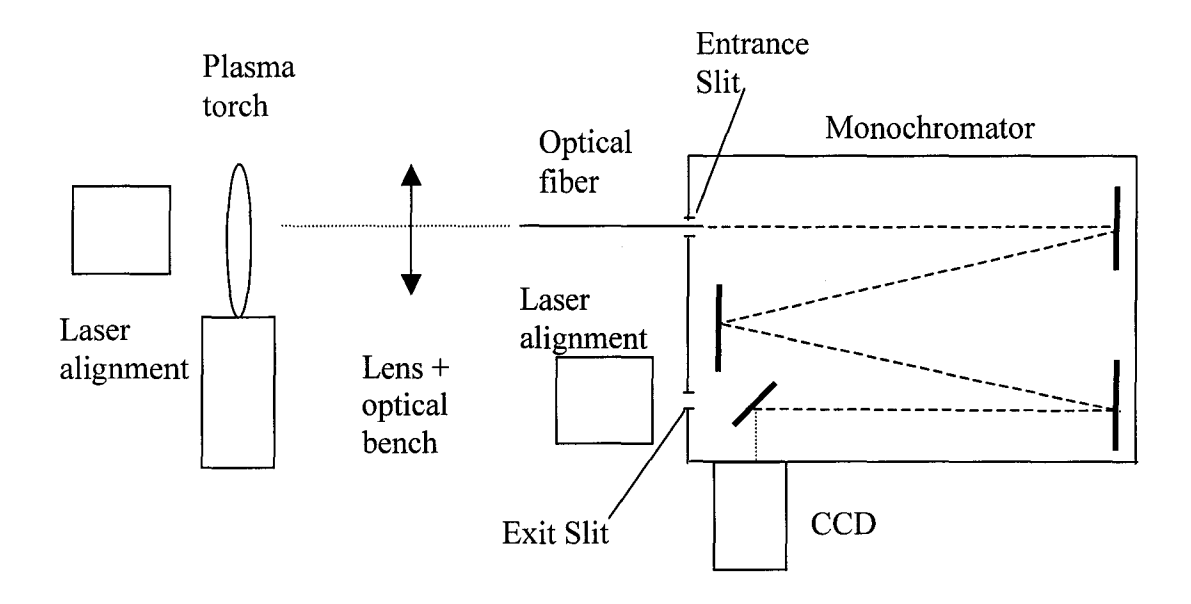


Figure 3.4: Optical setup

Chapter 4: Procedure & Analysis

4.1: Operation of Soot Production System

Before starting a soot generation experiment, the injection system heaters were turned on for warm up to the operating temperatures (Section 3.1.6) and helium pressure was applied to the C₂Cl₄ reservoir. The carrier gas and the liquid C₂Cl₄ rotameter were preadjusted to their respective flow conditions. The reaction chamber was evacuated to the maximum vacuum (the lowest attainable pressure) with a mechanical Ruvac E116-S25 double-stage root blower/centrifugal vacuum pump (*Leybold Inc.*). Then, the chamber was backfilled up to atmospheric pressure with argon. The column closed-circulation loop was filled with a 50% caustic solution and initiated by turning on the liquid pump. Since helium did not necessitate the use of the high-frequency generator for torch ignition in vacuum, a flow of 150 slpm of helium was used for torch ignition. Once ignited, the plasma jet was immediately adjusted to a flow of 100 slpm of argon for torch nozzle and chamber warm up. The warm up cycle lasted 10 minutes. A cold nozzle leads to accumulation of clogging graphitic material in itself and a cold reactor wall favors production of chlorinated by-product condensation.

Once the injection system, the packed-column and the reactor are ready, the plasma torch was readjusted to a flow of 225 slpm of helium. The chamber pressure and the plasma arc current were stabilized to the desired values. Finally, the mixture of helium carrier gas and gaseous C₂Cl₄ was initiated in the torch nozzle. The experimental runs were performed for 5 minutes. The non-automatic control devices, such as the arc current manifold, the rotameters and the globe valves, were adjusted, if needed, to their set point during the experiments.

After each experiment, the injection system and the plasma torch were shut down. The reactor was re-evacuated and backfilled with argon. The used NaOH was sent in a canister to the waste disposal unit and the column was rinsed out with fresh water. The system was then allowed to cool down for 2 hours before opening for soot collection. The

soot deposited on the reactor walls and cooling unit was brushed down and collected in sample bags. Zones before and after the movable disk in the reactor, on the disk itself and the quench zone were sampled and weighed separately for a better process characterization.

4.2: Mass Spectrometry

Before performing the long extraction and quantification procedures of fullerenes (Sections 4.3 and 4.4), samples were sent to the McGill Medical Mass Spectrometry unit. Figure 4.1 shows a typical mass spectrometry output of the soot produced where peaks for C_{60} (720) and C_{70} (840) are presented. According to the output, the process seems to synthesize chlorinated by-products and/or impurities. Fullerene and by-product yields are discussed in more detail in section 7.3.

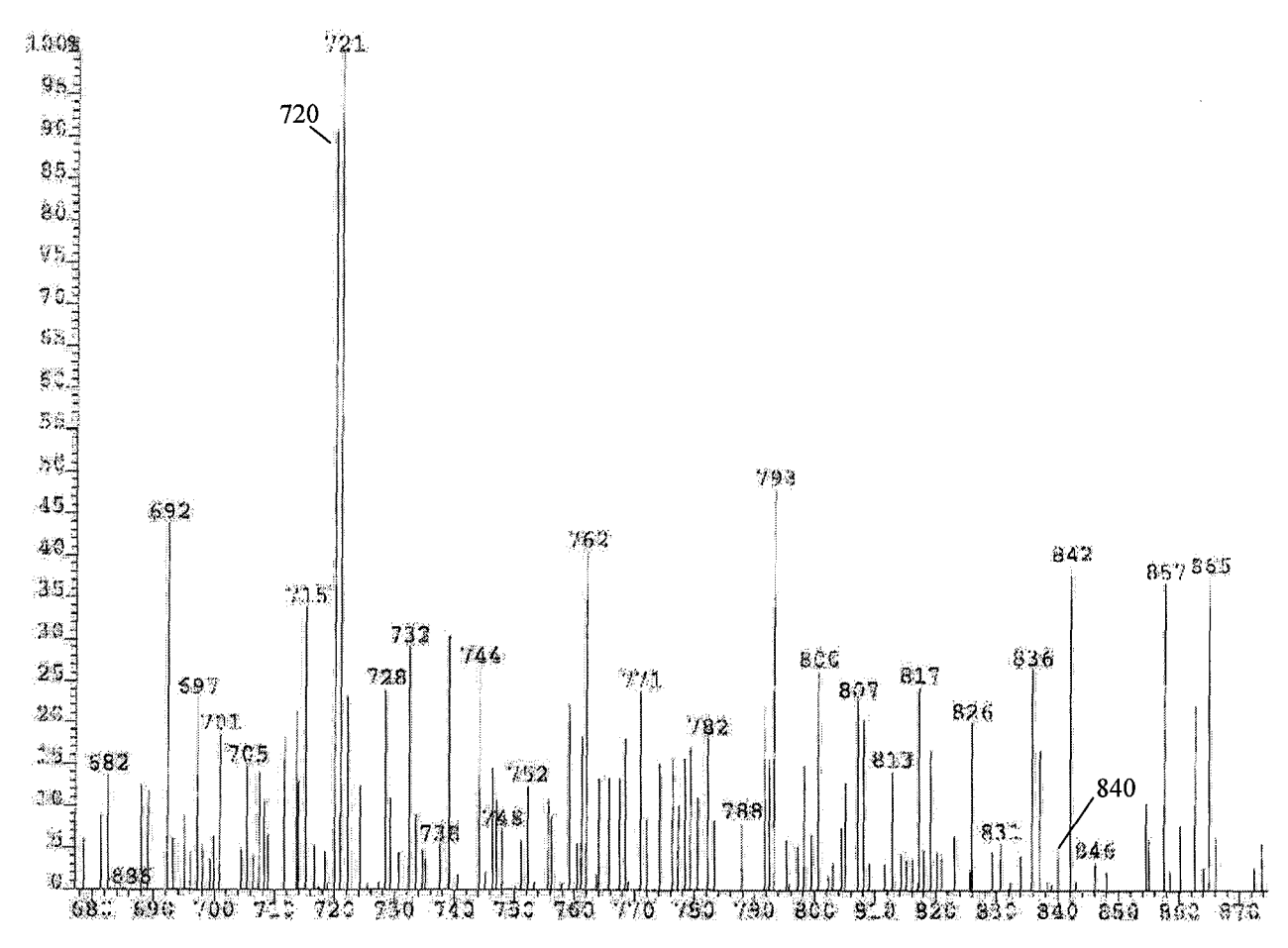


Figure 4.1: MS output of soot produced in the cylindrical reactor

4.3: Extraction of Fullerenes from Soot

The fullerene extract was first prepared by placing a suspension (4.5 mg/ml) of soot in toluene into a sonication bath for 30 minutes. The resulting solution was then vacuum filtered using Celite 521 [Aldrich] as filtering agent in a filtering funnel. During the filtration process, drops of toluene were added to clean the funnel wall and to make sure that the filtering agent paste never gets dried.

The solvent from resulting homogeneous solution was then evaporated in a rotary evaporator to yield a brown-black solid of crude extract. The extract was put on vacuum (10^{-3} torr) for a complete dryness. Toluene was trapped in a liquid nitrogen condenser at the pump inlet. The dry extract was weighed and the percent extraction was calculated as the following:

$$\%Extraction = \frac{Weight \ of \ crude \ extract}{Weight \ of \ soot} X100 \tag{4.1}$$

4.4: Quantification of Fullerenes in Crude Extract

The quantification of fullerenes in the crude extract was performed using HPLC. Ready for injection HPLC samples were prepared with the dried crude extract dissolved in a 250 ml volumetric flask. For most accurate results, the HPLC unit was calibrated using commercial standards of C₆₀ and C₇₀. The following HPLC operating conditions were obtained from the calibration and were used to quantify fullerenes:

Solvent:

65% methanol; 35% toluene

Injection volume:

 $20 \mu l$

Flow rate:

1.5 ml/min

Detection wavelength:

330 nm

The chromatograph output monitors the quantification as arbitrary units versus retention time. Amount of fullerenes is proportional to the area, expressed in $\mu V \cdot s$, under each fullerene peak. C_{60} peak appears at a retention type of 6.650 minutes and C_{70} , at 9.633 minutes.

Chapter 5: Modeling Background

The ability to build the large fullerene molecule is believed to depend on the residence time of the precursors in the appropriate temperature zone for fullerene formation, which is approximately situated between 2200K and 2600K [31]. In order to estimate these residence times, the spherical reactor model of Bilodeau *et al.* [6] was converted to the cylindrical geometry to evaluate the temperature and velocity fields inside the reactor. Basically, the change of the model geometry was made by transforming the small spherical nodes, which composed the whole reactor model, into rectangular nodes. One should note here that this conversion is only preliminary and does not represent the actual geometry of the reactor, particularly in the area of the torch itself and at the gas exhaust.

5.1: Explanation of model

5.1.1 Assumptions Applied by Bilodeau et al. [6]

- The plasma is assumed to be at Local Thermodynamic Equilibrium (LTE) and the reactor is operated at steady state;
- The reactor is assumed axisymmetric along the plasma jet. Therefore, the model is computed in two-dimensions. Three-dimensional effects of the C₂Cl₄ injection are thus neglected, but the momenta of these flows are respected. However, the model geometry does not respect the geometry around the plasma torch and in the gas exhaust zone around the movable disk (Figure 5.1 and 5.2). The ratio L_E/L_R=0.90 (Figure 5.1);
- The time-averaged effects of turbulence are considered. The K- ε model is used to calculated the contribution of turbulence on the transport coefficients in the equations of momentum, energy and carbon mass conservation;
- The effect of swirl imparted to the gas upstream of the torch is assumed negligible within the reactor;
- Compressibility effects are neglected. The squared Mach number M^2 is below 0.5;

- The plasma is optically thin. The radiation term is represented by the net emission coefficient method, with R_p = 0.5 mm. Proportion of carbon in the gas is taken into account, assuming that C₂Cl₄ is in a fully dissociated state;
- Condensation of carbon occurs at 1600 K;
- The effect of the electric field is neglected in the region considered, including the nozzle and inside the reactor volume.

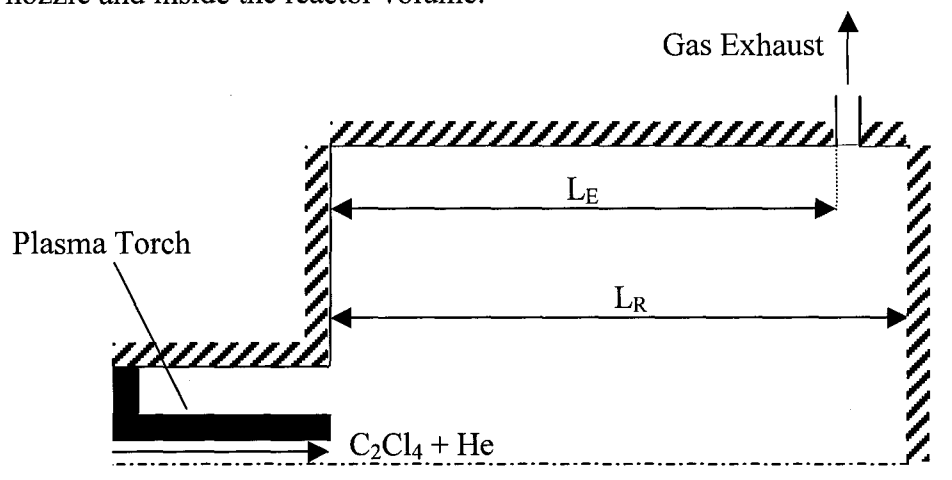


Figure 5.1: Computational domain of the simulated reactor adapted from the spherical model (L_E: length from Torch nozzle to gas exhaust; L_R: Total reactor length)

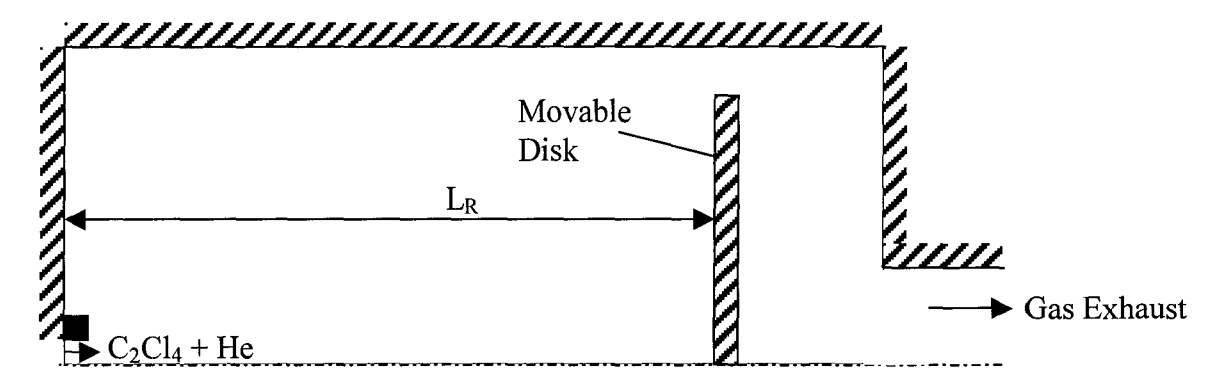


Figure 5.2: Actual experimental reactor geometry

5.1.2 Boundary Conditions [6]

The computational domain is shown in Figure 5.1 and consists of the nozzle, the torch tube and the cylindrical reactor. The axis of symmetry is taken to be in the direction of the plasma jet. The modeling equations are presented in Appendix II and are applied to the points in the gas phase that are not on the boundaries of the computational domain or

adjacent to solid walls. Conditions are however specified at the boundaries of the computational domain as follows.

Nozzle Entrance

Parabolic velocity and temperature profiles are assumed at the nozzle entrance, which is located just at the torch exit.

Axis of Symmetry

The radial velocity is null, as are the radial gradients of all other variables:

$$\frac{\partial v_z}{\partial r} = \frac{\partial h}{\partial r} = \frac{\partial X}{\partial r} = \frac{\partial K}{\partial r} = \frac{\partial \varepsilon}{\partial r} = 0 \qquad v_r = 0$$
 (5.1)

where v_z is the axial velocity, h, the specific gas enthalphy, X, the mass fraction of hydrocarbon in the gas and K and ε are respectively the turbulent kinetic energy and its rate of dissipation.

Reactor Exhaust

Gradient are assumed to be null in the direction of the flow (equation 5.1), and the radial velocity is adjusted to ensure conservation over the reactor.

Turbulence near Walls

Walls are taken into account on the intensity of turbulence. Wall functions are used to define the values of K and ε for wall adjacent points.

Reactor Walls

Special conditions are also fixed for the walls, which lie within the computational domain:

$$v_z = v_r = X = K = \varepsilon = 0 \tag{5.2}$$

Heat transfer through the wall occurs only by thermal conduction. The whole region surrounding the reactor computational domain is assumed to be composed of water fixed at a temperature of 350 K. Velocities are not solved and the heat transfer between the wall and water is defined by a convection coefficient.

Applying the mentioned assumptions and boundary conditions, the fullerene precursor residence times in the 2 200K-2 600K temperature window were estimated using the following experimental conditions.

Helium Plasma-Forming Gas (slpm):	225
C ₂ Cl ₄ Injection Flow (mol/min):	0.29
Pressure (torr):	200
Torch Power (kW):	45, 55, 65
Reaction Length (cm):	40, 63, 88

Chapter 6: Diagnostic Background

A plasma emission phenomenon consists of radiative decay processes of excited atoms or molecules at higher energy electronic states, which deliver an emission spectrum. The excitation process is typically the result of collisions between atoms and/or molecules in the thermal plasma systems, and is thus related to the energy distribution function of the various species, hence their temperature. Diagnostic methods, such as optical emission spectroscopy, are used to extract plasma properties of interest: temperature and species density as examples.

In this project, the plasma temperature profile was determined using spectroscopy according to the setup described in section 3.3. Plasma temperatures were extracted using the Boltzmann plot method on the C_2 molecular spectra (Swan Band) and Helium emission lines [4]. It is believed that the C_2 radicals play an important precursor role in the formation of fullerenes [28]. The C_2 Swan band also forms a very important contribution to the radiation emitted by the graphite arc plasma in fullerene synthesis experiments. Therefore, the Swan band becomes of great interest to study the presences and properties of C_2 radicals that possibly act as fullerene precursors [28].

In these measurement techniques, plasma temperature is calculated by relative intensity spectroscopy. Heavy particle temperature was extracted from the Swan Band rotational lines and electronic temperature, from helium lines at wavelengths 3964.73 Å, 5015.68 Å and 7281 Å.

Generally, some assumptions are required to exploit diagnostic methods based on the intensity measurement of the lines. These assumptions are particularly associated to the thermodynamic equilibrium of the plasma state and are reviewed shortly in the next paragraphs.

6.1: Generalities on Thermodynamic Equilibrium

6.1.1 Complete Thermodynamic Equilibrium (CTE)

A CTE plasma means that all elementary collision and radiative processes follow the microreversibility principle. The kinetic energy (the temperature) is the same for all plasma constituents (electron, heavy particles) and their possible reactions. It is useful to first assume this state even if it is impossible to reproduce it under laboratory conditions [7].

In a CTE situation, the plasma follows the equilibrium laws set by collisional energy exchange processes, where the following distributions apply:

1. The velocity distribution functions for every particles of species r follows the Maxwell-Boltzmann distribution:

$$f(v_r) = \frac{4v_r^2}{\sqrt{\pi} \left(\frac{2kT}{m_r}\right)^{3/2}} \exp\left(-\frac{m_r v_r^2}{kT_k}\right)$$
 (6.1)

where v_r is the velocity of particles of specie r, m_r is their mass, and T_k is a parameter describing their kinetic temperature [7].

2. The population density of the excited states of every species r follows a Boltzmann distribution:

$$n_{r,m} = n_r \frac{g_{r,m}}{Q_r} \exp(-E_{r,m} / kT_{exc})$$
 (6.2)

where n_r is the total number density of ions of species r, Q_r is their partition function, $E_{r,m}$ is the energy of the m^{th} quantum state, $g_{r,m}$ is the statistical weight of this state, and T_{exc} is the species excitation temperature [7].

3. The Saha equations describes the ionization equilibrium for neutrals, electrons, and ions:

$$\frac{n_{r+1}n_e}{n_r} = \frac{2Q_{r+1}(2\pi m_e kT)^{3/2}}{Q_r h^3} \exp(-E_{r+1}/kT_s)$$
 (6.3)

where E_{r+1} represents the ionization energy required to produce (r+1)-times ionized atom from an r-times ionized atom, and T_s is the species temperature related to the Saha law [7].

4. And the electromagnetic radiation field is governed by Plank's law:

$$B_{\nu}(T) = \frac{2h\nu^3}{c^2 (e^{h\nu/kT_{rad}}) - 1)}$$
 (6.4)

 $B_{\nu}(T)$ is the intensity at frequency ν of blackbody radiation. T_{rad} represents the temperature of blackbody radiation absorbed into the plasma [7].

CTE implies that the parameters T_k , T_{exc} , T_s , and T_{rad} are all equal and refer to a unique plasma temperature T [7].

6.1.2 Local Thermodynamic Equilibrium (LTE)

In laboratory applications, CTE cannot be assumed due to the presence of a temperature gradient. The radiative phenomena typically escape from the plasma and are not reabsorbed. Therefore, the concept of LTE is applied, where there is only microreversibility for the collision processes. Thus, the Maxwell, Boltzmann and Saha laws from the above section are still applicable and the Plank law is not. In addition, LTE requires that all local gradients (temperature, density, heat conductivity, etc.) are sufficiently small in order that a given particle diffusing from one location to another has enough time to reach equilibrium [7]. In fact, LTE can be stated when the light (electron) and heavy particles (molecular species) are in thermo-equilibrium, in other terms, when they are at the same temperature. The Boltzmann distribution $(n_{r,m})$ can be used giving the population density of excited energy states as a tool to extract plasma temperature; the intensity of the emitted radiation from a given state being proportional to the number of electrons (n_k) on that level.

6.2: Temperature Determination using Atomic Lines

The helium excitation lines were exploited to determine the electronic temperature profile. The relative intensities method is also well known as the Boltzmann diagram method. This graphical method, which requires the intensity of more than one spectral line, uses the combination of the Boltzmann distribution (eq. 6.2) with local atomic line emissivity. The local atomic line emissivity is represented by:

$$\varepsilon(r) = E \bullet A_{mn} \bullet n \tag{6.5}$$

where A_{mn} is the transition probability (s⁻¹) of an electron to transfer from energy level m to energy level n of the atom, E is the photon energy emitted from this transition, and n is the number of electrons. In this equation, a radial symmetry was assumed. Figure 6.1 schematics the energy emitted from a level transition of an electron.

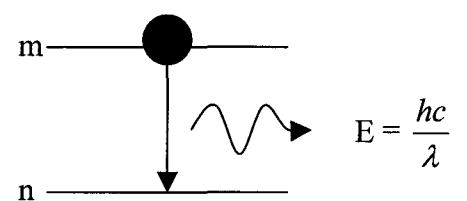


Figure 6.1: Level transition representation of an electron

And the combination of the Boltzmann distribution and the local atomic line local emissivity $\varepsilon(r)$ yields to:

$$\varepsilon(r) = A_{mn} \cdot \frac{1}{4\pi} \cdot \frac{hc}{\lambda} \cdot g_n \cdot \frac{N_{tot}(T)}{Q(T)} \cdot Exp\left(-\frac{E_n}{k_b T}\right)$$
(6.6)

Where,

λ: wavelength in cm

h: Plank constant (6.626217E-27 erg s)

c: Speed of light (2.99792458E10 cm s⁻¹)

k_b: Boltzmann constant (1.380662E-16 erg K⁻¹)

g_n: Degeneration term of the atomic level

 $N_{\text{Tot}}(T)$: the total density of pure plasma gas (cm⁻³) as function of temperature

Q(T): the internal partition function of pure plasma gas

E_n: Energy of the superior level (J)

Table 6.1 represents the choice of He lines used to perform the atomic spectroscopy analysis. These lines were selected, because there are relatively far from Cl lines. Usage of He lines near to Cl lines distorts readings due to the intensity absorption of one line by the other(s).

Table 6.1: Data of the selected spectral lines of Helium [36]

Wavelength (Å)	Energy E _n (cm ⁻¹)	gn	A _{mn} (10 ⁸ sec ⁻¹)
3964.73	191492.816	1	7.17X10 ⁻²
7281.35	184864.932	1	1.81X10 ⁻¹

Equation 6.6 is employed for the excitation temperature determination from absolute line emissivity. This method extracts temperature by comparing line intensities with a standard lamp.

For Boltzmann diagram method, equation 6.6 is rearranged by taking the logarithm on both sides:

$$\ln\left(\frac{\lambda\varepsilon(r)}{A_{mn}g_n}\right) = \frac{-E_n}{k_bT} + \ln\left(\frac{hc}{4\pi} \bullet \frac{N_{TOT}(T)}{Q(T)}\right)$$
(6.7)

Processing a few spectral line emissivities, the temperature for each distance (x) from the plasma centerline may be obtained by computing the inverse slope of the curve:

$$\ln\left(\frac{\lambda\varepsilon(r)}{A_{mn}g_n}\right)vs.\frac{-E_n}{k_b} \tag{6.8}$$

6.3: Temperature Determination using Molecular Lines (C₂)

Plasma temperature determination from molecular spectroscopy may be performed by line superposition, where an experimental line is fitted to a simulated Swan Band system at a given temperature and by Fowler Milne, which is based on equilibrium thermodynamic law. In this work, the Boltzmann diagram method applied on rotational lines was used. Saidane [41] and Sum [46] rigorously described this method.

For a rotational line, it can be formulated:

$$\ln\left(\frac{\varepsilon}{\sum S_{K'',J'}^{K',J'}}\right) = -\frac{hcF_{v}(J)}{k_{B}T} + \ln C$$
(6.9)

Where,

ε: Emissivity of the C₂ line

 $\sum S_{K'',J''}^{K',J'}$: Holn-London factor

 $F_v(J)$: Rotational energy of the analyzed line

Equation 6.9 is applied on rotational lines 25, 26, 27, 28, 30, 39, 40, 42, 43, 45 in order to plot the Boltzmann diagram. Figure 6.2 presents a simulated Swan band for a temperature of 4000 K.

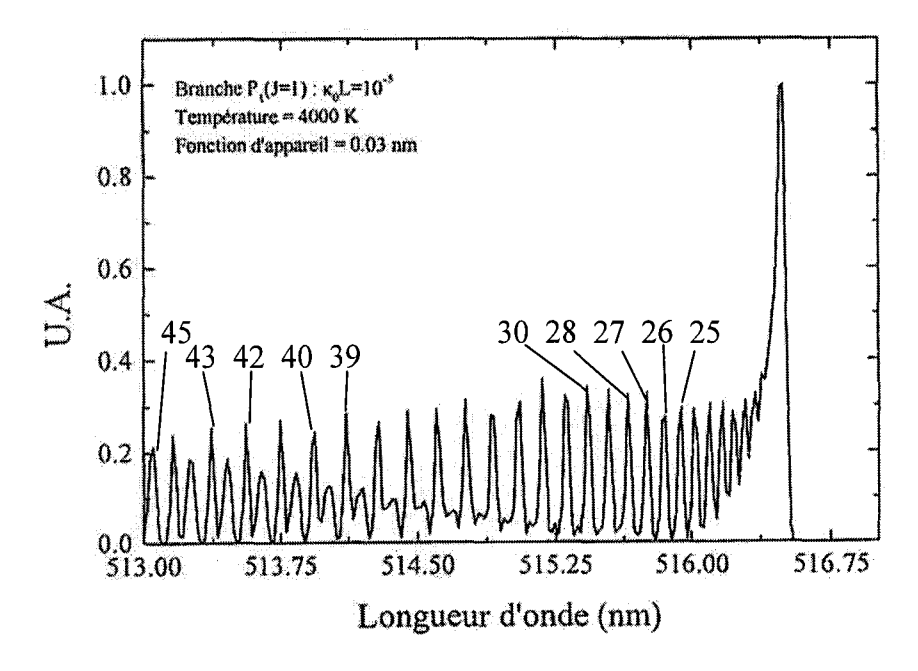


Figure 6.2: Simulated Swan band for a temperature of 4000 K [41]

6.4: Abel Inversion

Plasma constitutes a non-uniform light source. The emitted light per unit volume depends on the considered area. Each line of sight data acquisition measures the integral intensity $(I(x)^1)$ emitted by the plasma on the line of sight, which is y on Figure 6.3. Therefore, this intensity corresponds to the contribution summation coming from all the plasma regions along the line of sight. Using a mathematical tool, a given I(x) of a plasma of total radius R may be transformed into local emissivity $(\varepsilon(r))$ [30][35]. This mathematical tool is called the Abel Inversion and has the function to reconstruct cylindrical symmetric profiles from its projection [8].

If I(x) is the experimental intensity measured following the line of sight (y) situated at a distance x from the plasma centerline axis, I(x) can be related with the radial emissivity ($\varepsilon(r)$), r being the radial distance from the plasma centerline axis (Figure 6.3):

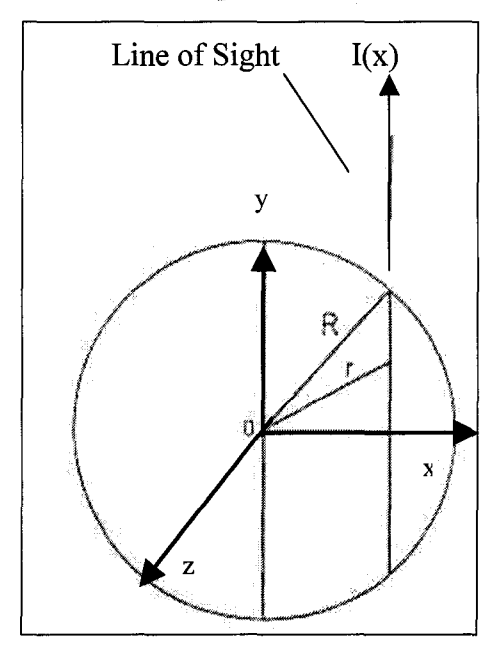


Figure 6.3: Illustration of the Abel Inversion [35]

Abel Inversion was however not applied during the plasma diagnostic, because not enough total intensity acquisitions along x were performed for an appropriate radial profile. In the present setup, the lack of intensity acquisitions along x is due to time limitations during experimental runs. The time constraints are intrinsic to our synthesis

 $^{^{1}}$ I(x) is found by computing the area under the spectral line at the given wavelength displayed on the CCD photodiode.

system: the optical fiber tip was moved manually with a micrometric screw along the x axis, rather than a step-by-step motor, each line intensity acquisition required an exposure time of 3-5 seconds, and the accumulation of soot on the reactor quartz window was obstructing the light intensity after just a few minutes. As a consequence, only three acquisitions were made at x=0, ± 6 mm for every z position and wavelength recorded. Thus, the obtained temperatures profiles only consider total intensity, which results in average temperature along a line of sight instead of a local temperature. One may note however that the intensity I(x) recorded is strongly influenced by the maximum emissivity $\epsilon(r)$ along the line of sight. Hence, such measurement is often seen in the literature as representing an estimation of the maximum temperature in the jet.

The procedure for spectral acquisition of the C_2 Swan band was not affected by this time evolution of soot deposited on the window since a global C_2 band spectra is acquired within an exposition of 3-5 seconds, and only relative intensity values are used for temperature evaluations.

In the case of He line acquisitions, in order to try to maintain relatively uniform window opacity for different lines, the reactor was stopped after one wavelength acquisition to yield time for monochromator adjustment to a new wavelength. This procedure of course strongly increases the uncertainty of the measure temperature.

Chapter 7: Results and Discussion

7.1: Modeling

The simulation was performed with the operating conditions described in Section 5.2. For comparison purposes, Figures 7.1 and 7.2 respectively represent the typical modeled isotherms and gas velocity vectors inside the reactor for the operating conditions used for spectroscopy. As observed in the spherical reactor [1][2][6], the main stream shows strong thermal gradients occurring in the radial direction and axial gradients in the area in front of the end plate (Figure 7.1), and also a large re-circulation in the region away from the hot plasma (Figure 7.2). Note that the length of vectors in Figure 7.2 and 7.3 is not proportional to velocity. The purpose of these figures is to illustrate the gas re-circulation in their respective reactor.

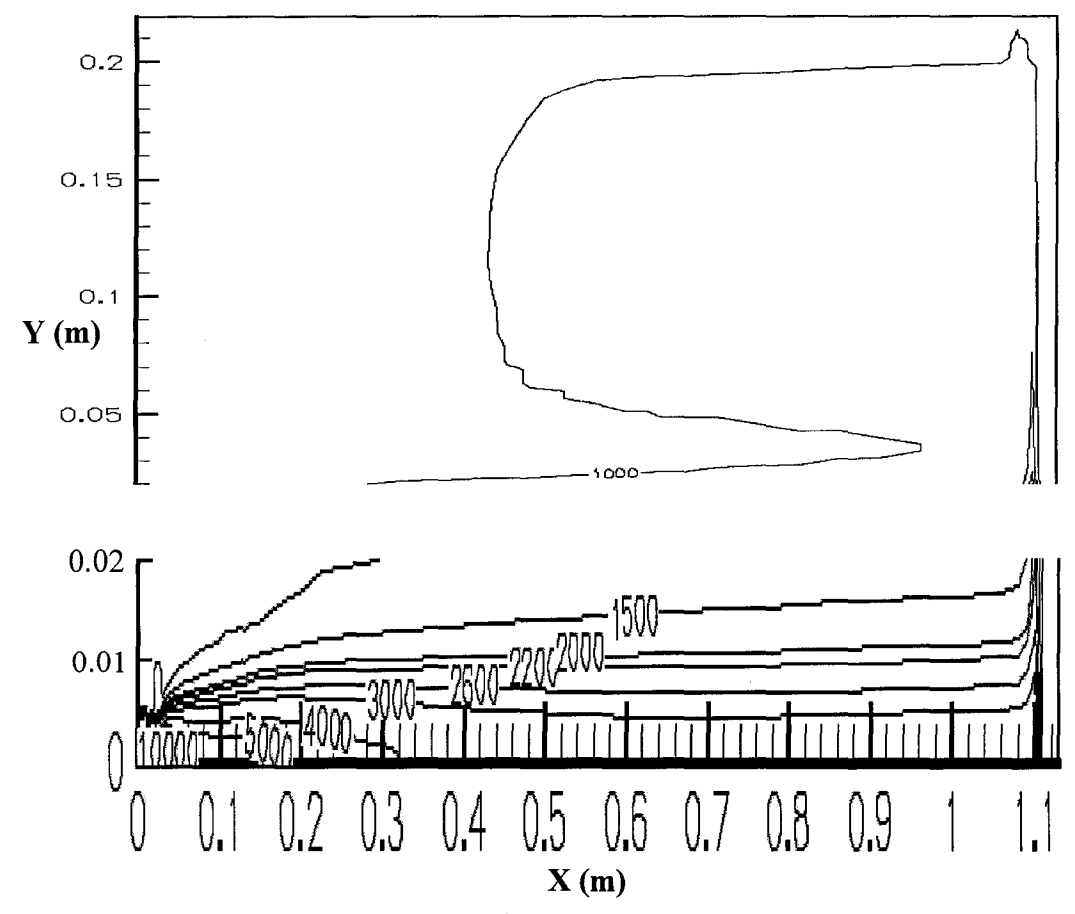


Figure 7.1: Reactor Isotherms (K) from modeling in the 1 m long cylindrical reactor [45 kW, 0.15 mol/min C₂Cl₄, 200 Torr, 100 cm reactor length]

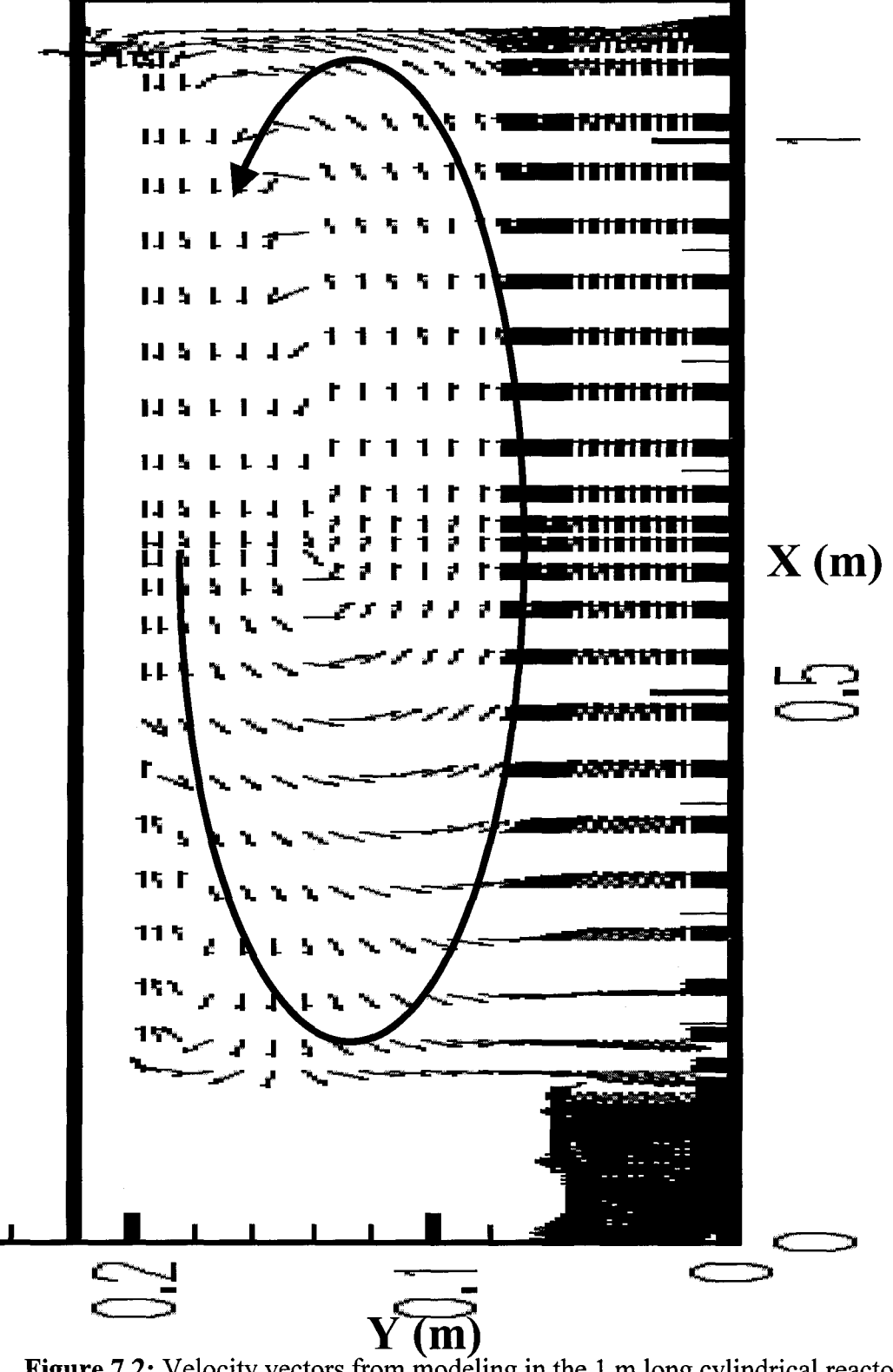


Figure 7.2: Velocity vectors from modeling in the 1 m long cylindrical reactor [45 kW, 0.15 mol/min C₂Cl₄, 200 Torr, 100 cm reactor length]

The fullerenes formation temperature window was shown by Mckinnon [31] to be between approximately 2200-2600 K. Residence times of the plasma gas along the plasma torch tailflame axis (y=0) were thus calculated by Alexakis [1] in this temperature window in the spherical reactor. It has also been showed experimentally [1] that as residence time increases in the C₂Cl₄-based reactor, the soot and fullerene yields increase. Such residence times were thus calculated for the present 1 m long cylindrical geometry (Table 7.1). The results yield residence times that are substantially higher than those calculated in the spherical geometry. A cylindrical reactor may thus allow a greater expansion of the 2200-2600 K volume. Because of the geometry, size of the reactor, and location of the exit port made as an annular ring around the movable disk, the cold gas recirculation close to the torch nozzle is minimized when compared to the original spherical reactor. This effect should favor higher fullerene yields and formed the basic idea behind the change to a free axial expansion of the plasma tailflame opposed to the strong quenching re-circulation induced by the spherical profile.

Table 7.1: Comparison of residence times in 2200-2600 K zone obtained in the cylindrical (1 m long) and spherical reactors [1]

Experimental Conditions			Modeling Results			
Condition #	Plasma flow (slpm)	Power (kW)	C ₂ Cl ₄ feed rate (mol/min)	(torr)	Residence time in 2200- 2600 K (s) (Cylindrical)	Residence time in 2200-2600 K (s) (Spherical)
1	225	45	0.29	200	1.29 x 10 ⁻³	3.0×10^{-5}
2	225	55	0.29	200	1.29 x 10 ⁻³	9.1 x 10 ⁻⁵
3	225	65	0.29	200	1.03 x 10 ⁻³	11.0×10^{-5}

Table 7.2 sustains this affirmation: a longer reactor enhances the precursor residence time. The temperature profiles for the different reactor lengths are displayed in Appendix II for the first 0.5 m length of the reactor. One can speculate that as increasing the reactor length, the 2200-2600K temperature window is stretched towards the end of the reactor and less cold gas re-circulation enters the plasma centerline axis.

Experimental conditions					Modeling Results	
Condition #	Plasma flow (slpm)	Power (kW)	C ₂ Cl ₄ feed rate (mol/min)	Pressure (Torr)	Reactor length (cm)	Residence time in 2200-2600 K(s) (Cylindrical)
74	225	55	0.29	200	40	0.96×10^{-3}
5	225	55	0.29	200	63	1.07×10^{-3}
6	225	55	0.29	200	88	1.23 x 10 ⁻³

Table 7.2: Residence times in 2200-2600K zone versus three investigated reactor length during the experimental soot generation (Section 7.3)

However, only preliminary comparisons of the residence time between both reactors can be made for the following reasons. First, the velocity vector profile (Figure 7.2) shows that the first 10 cm on the axis was modeled using the spherical geometry computational domain (Figure 7.3); there is no velocity data representation on Figure 7.2 for radial distances higher than 0.05 m. This results in an end plate position occurring in the modeling figures with an added 10 cm downstream from the true experimental position.

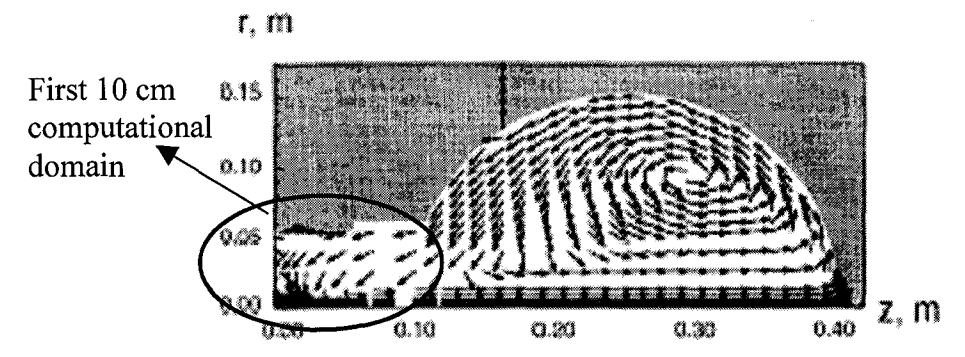


Figure 7.3: Velocity vectors from modeling in the spherical reactor geometry (ID=30 cm) [6]

Second, the 2200-2600 K temperature windows stretched on the overall length of the reactor, while the spectroscopy show a less spread reality of this temperature zone. Spectroscopy measurements were attempted on axial distance away from the torch nozzle (>10 cm) and the CCD detected no plasma emissivity. Plasma emissivities are usually detected at such temperature levels.

7.2: Spectroscopy Results

Relative intensity spectroscopy was conducted on the plasma flame with and without C₂Cl₄ injection. The modeling related to the spherical geometry could not be tested and compared to experimental data because of the lack of optical access in that reactor. The present cylindrical reactor design provides this optical access, giving the possibility for a first comparison of the model with experimental data. The modeling is therefore used to indicate the general trends for the present case. The obtained experimental results will help to make further refinements on the modeling.

As indicated in section 6.4, one problem observed during the spectroscopy study was the accumulation of soot on the quartz window strongly limiting light intensity acquisitions to only a few minutes (1 to 2 minutes) of experimental run. Thus, the lowest carbon mass rate and relative intensity measurements were chosen in order to increase the acquisition time, and include the soot hindering effect in the temperature calculation. The procedure used is explained in Chapter 6 and the operating conditions were the same as in Figure 7.1 and 7.2 for temperature comparison purpose.

Measurements were collected at the centerline and ± 0.6 cm radial distances in the flame over a length of 7.5 cm. Axial distances further away from the torch nozzle are unfortunately not accessible due to poor plasma intensity. Temperatures were extracted using the C_2 molecular spectra (Boltzmann diagrams over lines in the P-branch of the $A^3\Pi_q$ - $X^3\Pi_u$ Swan system) and helium lines at wavelengths 3964 Å and 7281 Å giving the least amount of interference with chlorine radiation. Figure 7.4 is a close-up of the modeled temperature profiles near the torch nozzle and Figure 7.5, the evaluated temperature for both the C_2 molecule (Swan band) and He atomic line spectra. Note that the measured temperatures are well above the condensation temperature of Carbon (≈ 1600 K). Therefore, carbon particle radiation within the plasma should not influence the recorded intensity. Most of the soot collection is made downstream in the reactor. The

possible absorption of the carbon soot in the cold gas surrounding the plasma has been neglected.

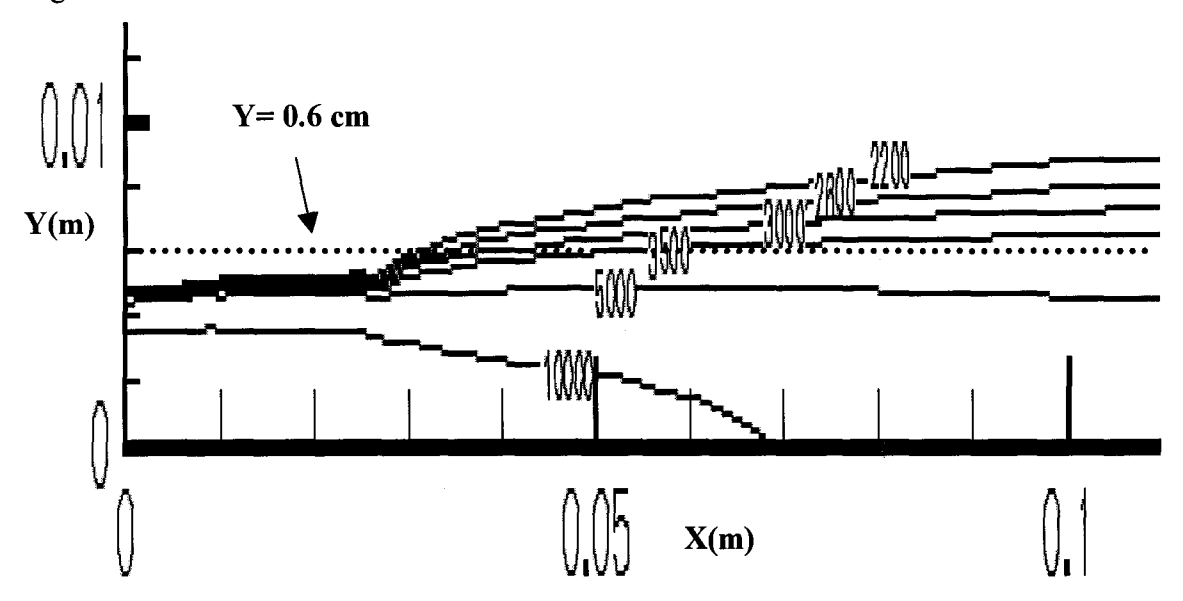


Figure 7.4: Modeled temperature profile (K) near the nozzle exit region

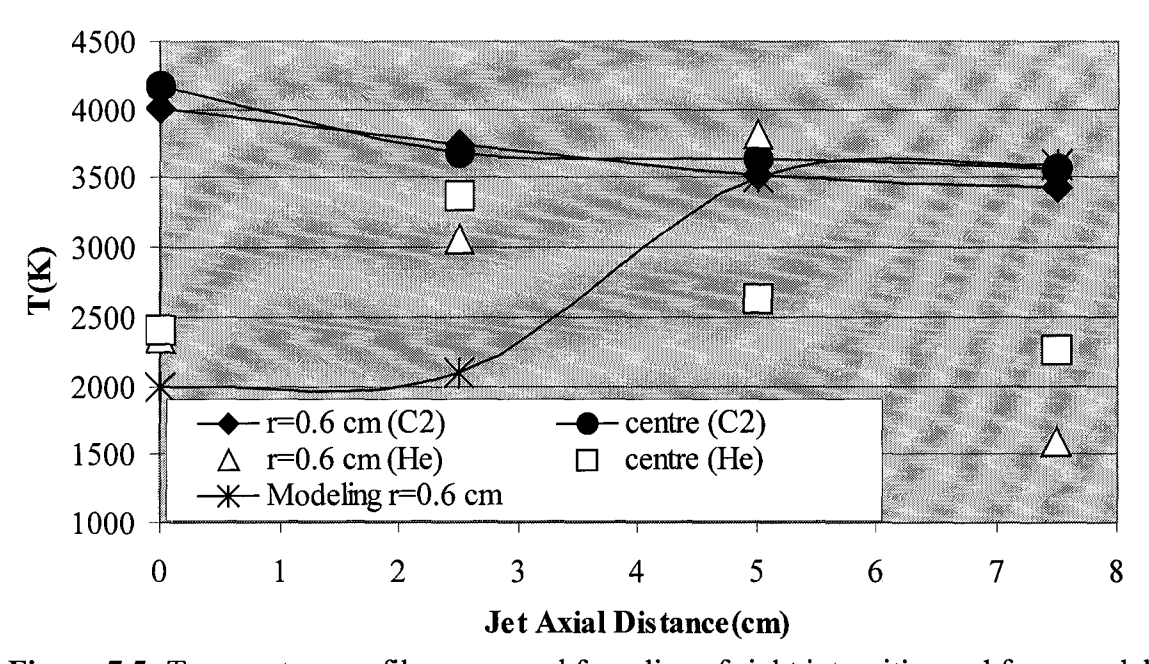


Figure 7.5: Temperature profiles measured from line of sight intensities and from modeling (operating conditions in Table 7.1; Torch Power=45 kW and reactor length=63 cm)

Temperature profiles on the helium lines on Figure 7.5 show a scattered profile following the plasma jet axis. Since the plasma torch is assumed to operate at LTE, these profiles

should display a decreasing temperature profile close to those using the Swan Band (C₂). Experimental errors may be attributed to this study. Boltzmann diagrams for the helium temperature were plotted using only two excitation lines. Hence, only two points were used to calculate the slope in the Boltzman plot. Usually, at least five lines are suggested for such temperature evaluation. Plasma temperatures extracted from the Swan band present a consistent decreasing profile from 4167 K at x=0 to 3563 K at x=7.5 cm for the centreline axis and, from 4005 K at x=0 to 3430 K at x=7.5 cm for a radial distance r=0.6 cm. Boltzmann diagrams of Swan band were plotted using ten rotational lines and the experimental temperature profile thus suggests that the 2200-2600K temperature window is further downstream of the plasma region. Figure 7.6 is an example of Boltzmann diagram plotted using Swan Band at point (0, 0.6) on the plasma jet.

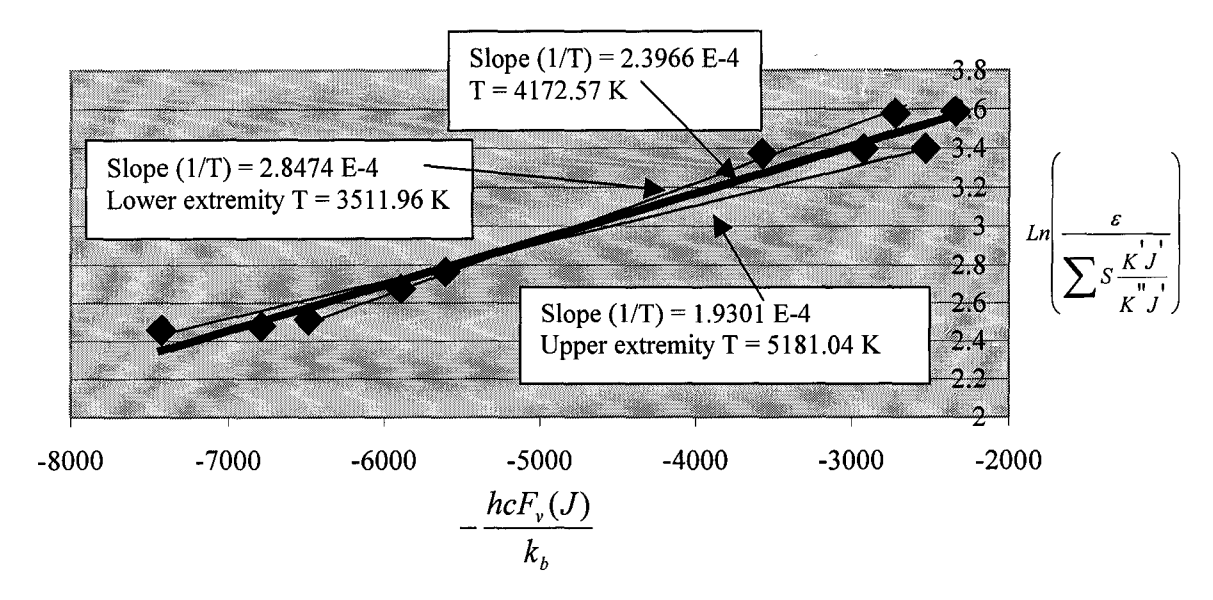


Figure 7.6: Boltzmann plot on Swan Band obtained at point (0, 0.6) on the plasma jet

As expected, the ten points on Figure 7.6 tend to follow a straight-line shape. Plotting a straight line between the points, the average slope (1/T) and temperature respectively yield to 2.3966 E-4 and 4172.57 K at this point in the plasma jet. Computed temperatures on extreme points on the above Boltzmann diagram gives 5181.04 K (+24.2%) for the upper extremity and, 3684.26 K (-15.8%) for the lower one. These temperatures and percentages demonstrate the high degree of sensitivity of the Boltzmann diagram when done with only two points and explain the usage of several spectral lines in plotting such

graph. Thus, higher percentage errors can be attributed to temperatures extracted from the helium spectral lines.

The profiles show temperature values that are much lower than the estimated 10 000 K through modeling (Figure 7.4) on the torch centreline axis. It was thus not relevant to show the modeled temperature from values at the centre on Figure 7.5. Given that the Abel inversion was not performed, this spectroscopic profiling displays average temperatures rather than local ones, which should be slightly higher. Considering that carbon is in ionic form for temperature of 10 000 K, there is very low or no emissivity coming from the Swan band in the core of the jet.

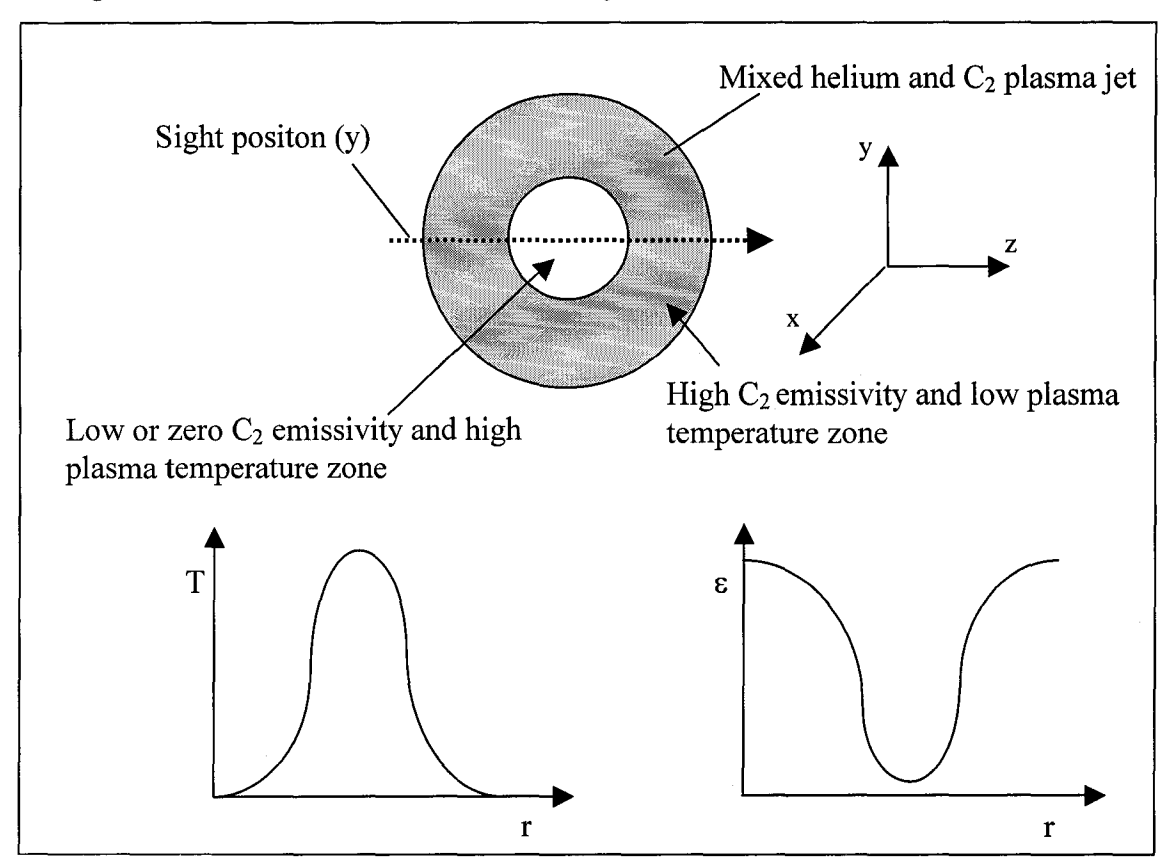


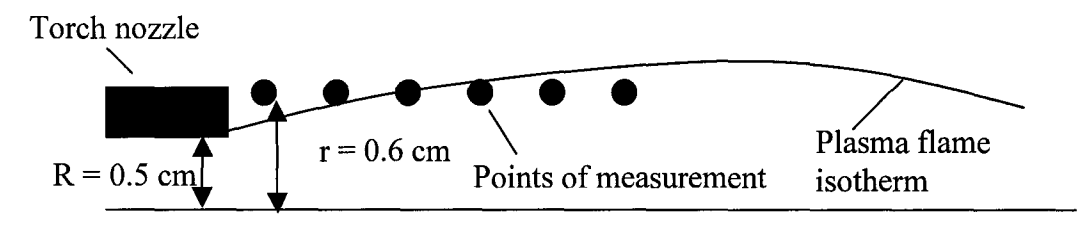
Figure 7.7: Hypothetical Temperature pattern (left) showing maximum temperature in the core of the jet, and the Swan band (C_2) emissivity (right) as a function of radius in line of sight positions y=0

Figure 7.7 shows the difference between the hypothetical plasma temperature and C₂ emissivity patterns along one sight position (y). The collected intensity measurements

may thus come from the extremities of the plasma jet captured by the line of sight and temperature in the core of the plasma jet may thus not be determined precisely. Abel inversion is very seldom used in profiles such as the C_2 Swan band showing off-axis peaks of intensity. One cannot rely on this line of sight measurement to evaluate core temperature of the jet. This higher core temperature is expected to be in a range where practically no C_2 emission exists. Data acquisition using several atomic lines will be needed to measure the plasma core temperature.

A huge part of the difference between the modeling and the experimental temperature values is also attributed to the different size of torch nozzle used in both situations. Although the experiments were performed originally with a nozzle having 5 mm in radius as for the modeling calculations, the relatively strong erosion caused by the chlorinated plasma increased this outlet radius to 7 mm over a series of experimental runs. The model also assumed cylindrical nozzle geometry, while the nozzle erosion pattern effectively shows a conical type of geometry. Such changes should promote radial dispersion of the jet and lead to a decrease of the temperatures measured on the plasma jet axis. This cooling phenomenon is not seen to affect regions at a certain radial distance from the torch centreline. From Figure 7.5, experimental and modeling values are situated in the same temperature range at r=0.6 cm from the plasma centreline axis at jet axial distances of 5 cm and higher. Closer to the torch nozzle at radial position of 0.6 cm, the model predicts lower temperatures because of the limited radial extent of the tailflame exiting from a 5 mm radius nozzle. The experimental nozzle however was eroded with time resulting in a diameter of approximately 7 mm, explaining the differences for $z \le 0.5$ cm (see Figure 7.8).

a) Modeling representation of the plasma flame



b) Real representation of the plasma flame

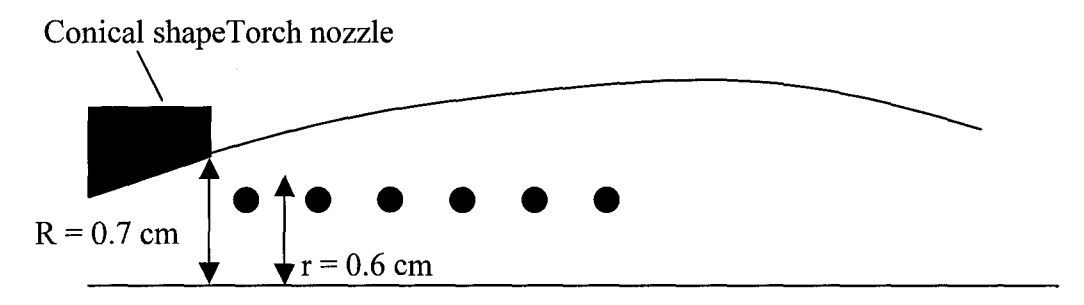


Figure 7.8: Temperature point of measurement between modeling (a) and experimental acquisitions (b)

7.3: Soot Generation Experimental Results

7.3.1 Vacuum Trials and Improvements

Previous work done by Sum [46] using the same cylindrical reactor associated the absence of fullerene in the produced soot partly to the vacuum leaks of air contaminants into the reactor. The nitrogen and oxygen contained in the atmosphere act as a contaminant limiting the fullerene formation and yielding CN and CO_x molecules. Thus, vacuum leaks reduce the availability of carbon for fullerene formation and may add convective cooling term. A maximum vacuum of 5 to 10 torr was achieved at the evacuation step and spectroscopy studies detected the CN molecular band between wavelength 389.5 and 392 nm [46]. These results thus suggested performing vacuum trials and improvements.

Following unsuccessful tests with a leak detector, it was decided to go with a trial and error study. The reactor was evacuated to its maximum level following various modifications on O-ring seals, ports, etc. The vacuum-controlling valve was then closed and the pressure from a MKS Baratron gauge was recorded on a strip chart leading to leak rate evaluations. The pressure range was recorded from 5 to 20 torr as a function of time to reach a minimum leak rate value.

During these tests, the changes on the reactor lowered the base vacuum to 0.65 torr (86.6 Pa) and the leak rate from 7 torr/min to 1 torr/min. Most of the changes were made on the O-rings and poorly fixed Normal Pipe Thread (NPT) fittings, while some of the original welds were redone. Originally, the reactor was sealed with custom-made buna O-rings. Custom-made O-rings do not insure a good seal due to potential leaking sources at the joint site and buna material is not recommended for a chlorinated environment. All O-rings were replaced by manufactured ones made of viton, which are chlorine resistant. The several NPT fittings that composed the reactor were carefully sealed with Teflon. NPT fittings are characteristically machined with large threads, which encourage leaks. An insulation application is always necessary in their uses and Teflon is widely used for this purpose due to its heat and corrosion resistance. At this point, the cylindrical reactor has a higher leak rate than the spherical one due to its larger size and the larger amount of ports and access parts.

The optimal base vacuum of 0.65 torr (86.6 Pa) attained is still higher than the base operating pressure of less than 10 Pa recommended by Saidane [41] in his study of residual gas contamination. This study was made in a graphite arc system, where the reactor was preliminary evacuated to 0.1, 1, 10, 100 Pa before filling it up with helium. Figure 7.9 shows that the presence of nitrogen related to a low vacuum aborts the fullerene condensation process and encourages the production of contaminants, such as CN. The graphite arc system however uses a fixed gas pressure, where no helium is flowing in the reactor. This is very different from the plasma torch system, where a high flow of helium (225 slpm) is continuously fed to the reactor and not necessarily entrained in the reaction zone.

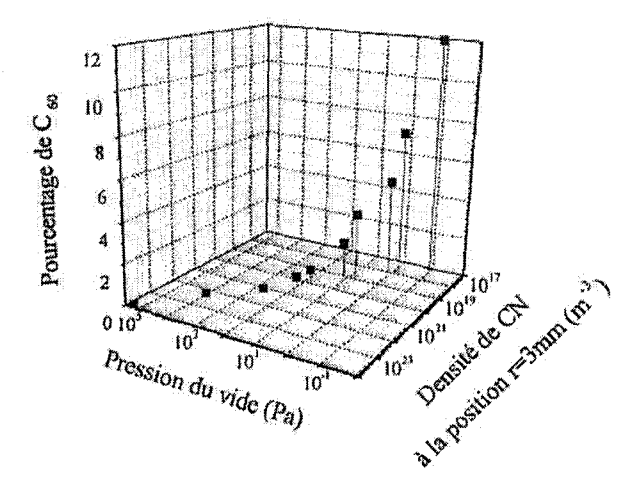


Figure 7.9: Percentage of C₆₀ in soot and CN density versus base vacuum [41]

7.3.2 Overall Energy Balance

In order to compute the cooling efficiency and fullerene yield, the following system (Figure 7.10) has been established around the experimental setup for heat and mass balance calculations.

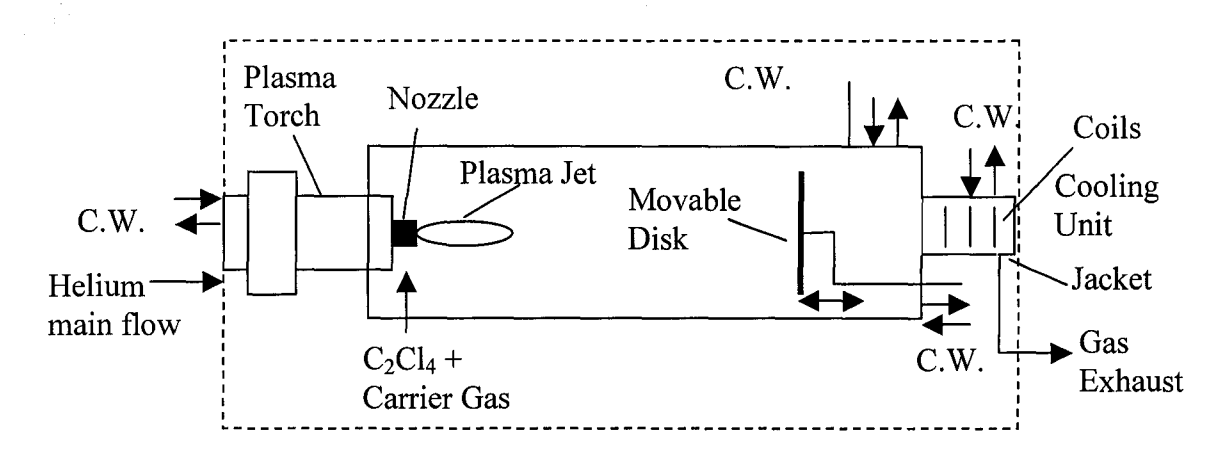


Figure 7.10: System definition for energy balance calculations (C.W.=cooling water)

Taking the reactor as the system, the overall energy balance is expressed as the following:

$$Q_{Accumulation} = Q_{Input} - Q_{Torch Water} - Q_{Reactor Water} - Q_{Exhaust Gas}$$
(7.1)

Temperature data acquisitions were performed running the torch at 45 kW with 225 slpm of helium in order to calculate the reactor and the torch efficiency. During these experiments, the movable disk was set to run a reactor of 88 cm long. As far the original spherical reactor design, the system never achieves steady state during soot generation due to the continuous accumulation of soot on the reactor walls. Measurements were thus recorded without injection of C₂Cl₄. Thus, the helium gas entering the reactor through the plasma torch is exhausted by the vacuum pump and the mass and energy accumulation terms equal zero.

Table 7.3: Summary of the calorimetric study

	Plasma Torch	Reactor	Movable Disk	Cooling Coils
Cooling-water flow (I/min)	22.0 ± 0.5	11.70 ± 0.05	12.10 ± 0.05	16.70 ± 0.05
Energy Transferred to cooling water (kW)	17.8 ± 0.8	15.61 ± 0.81	2.30 ± 0.11	0.72 ± 0.12

According to the energy balance equation and Table 7.3, 81% of the input energy to the plasma jet is transferred to the overall cooling water, and 40% of this amount going to the torch cooling water. This leads to the conclusion that 19% of the energy leaves with the off-gas, while the torch has an efficiency of 60.4% when it is operated at 45 kW. Similar measurements on the spherical reactor setup yielded 73% to 77% torch efficiency [1]. This difference may possibly be explained by small changes in torch electrode geometry and/or cooling water temperature difference. The torch supplier indicated that slight changes were made on the electrode inner diameters. With regards to cooling water, Alexakis [1] used a closed water circuit controlled at 22.9 ± 2.8 °C at the torch inlet for cooling, whereas city water was employed for the present thesis. Since experiments were performed during wintertime, the temperature at the torch inlet lied between 1°C and 5°C.

An unrealistic cooling term of -0.45 kW was obtained for the jacket surrounding the cooling coils. The low temperature gradient between the cooling water and gas in the

cooling zone did not lead to a temperature rise of the cooling fluid. Therefore, this negative temperature gradient is probably due to the action of background noise on the thermocouples.

The error on the energy transferred to cooling water was calculated according to the significant figures in the flow measurements (digital output and analog rotameters) and thermocouple readings. Error on the flow measurement was defined to be half of the smallest unit of measurement.

7.3.3 Overall Mass Balance

To seek the effect of the reactor length on fullerene yield, soot generation runs were performed using middle range operating conditions: 55 kW torch power, 0.29 mol/min C₂Cl₄ feed rate, 200 torr chamber pressure, 5 minutes operation time and 40, 63, 88 cm reactor length.

Figure 7.11 and Table 7.4 display respectively the total mass of soot and the percentage of recovery in the reactor after 5 minutes of operation and, the dependency of the soot yield and mass recovery with the reactor length. No atmospheric contaminant entering the reactor, such as nitrogen and oxygen, is assumed. The percentage of recovery is computed using the total mass of input C₂Cl₄ and the results are compared with those obtained with the former spherical reactor of 30 cm I.D. [1] using the same operating conditions. However, Alexakis results were performed during 4 minutes operation time.

After each trial, the soot was separated in four different samples according to their provenance in the reactor. Soot collected before the movable disk, on the disk and on the reactor wall that surrounds it, after the disk, and in the cooling zone was analyzed separately for a geometric fullerene yield profile. Soot collected at the disk level counted for more than 80% of the total soot and was darker than soot coming from any other parts of the reactor. Soot coming from the cooling zone, before and after the disk was brownish black, predicting a higher degree of chlorinated by-products. Thus, this device and its

surface temperature play a critical role in gas quenching and precursor residence time. This is unlike the spherical reactor showing soot collection distributed on essentially all reactor walls with varying concentration of $C_{60, 70}$. The present reactor seems to provide better selectivity and control of the conditions at the collecting surface, a parameter that will need to be optimized in terms of overall yield in future work.

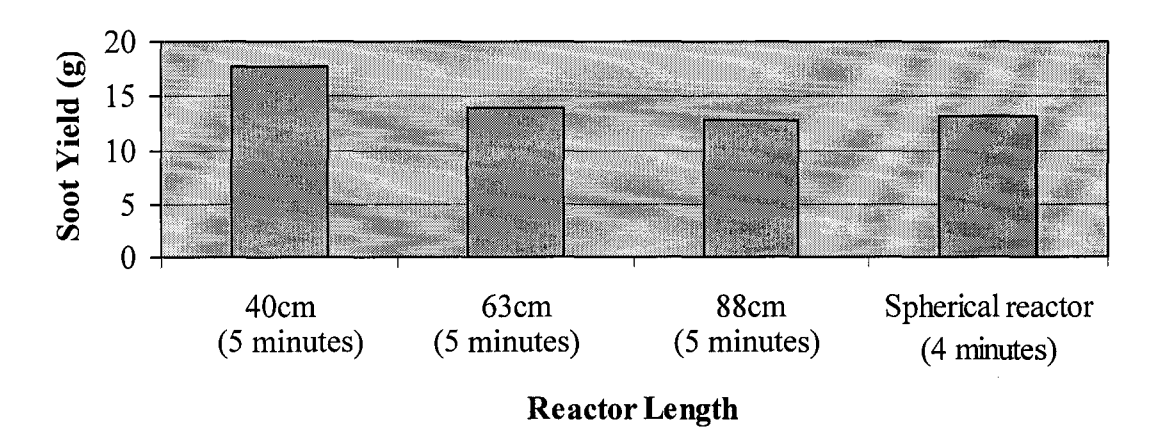


Figure 7.11: Deposition yield for total soot (Note that cylindrical reactor results are for 5 minutes operation)

Table 7.4: Summary of percentage mass recovery

Reactor Length/Type	C ₂ Cl ₄ feed rate (mol/min)	Time of experiment	Mass of Input C ₂ Cl ₄ (g)	Percentage of Mass Recovery	Percentage of Carbon Recovery
40 cm	0.29	5 min.	240.439	7.36%	50.86%
63 cm	0.29	5 min.	240.439	5.75%	39.73%
88 cm	0.29	5 min.	240.439	5.29%	36.55%
Spherical (30 cm ID)	0.29	4 min.	192.351	6.80%	46.98%

As observed in Table 7.4 and Figure 7.11, the percentage of mass and carbon recovery for the shortest (40 cm long) and the spherical reactor are in agreement to their similar size. The results for longer (63, 88 cm) reactors are lower compared to optimized results obtained with the original spherical reactor [1]. The strong limitations of the formation temperature window and large cooling-gas re-circulation in the plasma jet offered by the spherical shape and 40 cm long reactors encourage a higher soot condensation. Also, wall

temperature is known to be a key factor in fullerene soot condensation rate [1]. Insufficient temperatures increase by-product formation, while excessively high temperatures produce loss of C_{60} by sublimation. For longer reactor cases, the plasma radiation and convection energies were transferred to a larger inner surface area than in the 40 cm long and 30 cm ID spherical reactors, predicting lower wall temperature. During the first minute of operation, it was observed that the cold reactor walls condensed a layer of sticky chlorinated carbon compounds, which was not recoverable in the soot. It was observed that this sticky layer became more and more important as increasing the reactor length. One solution to this is to apply a layer of insulation to increase the wall temperature toward a higher yield of soot and fullerenes and pre-heat the reactor chamber before C_2Cl_4 injection.

The poor wall temperature optimization also determines the circumstances of larger amount of soot produced in a shorter reactor (Figure 7.11). A 40 cm long reactor generated up to 18 g of soot in five minutes of operation, while 63 cm and 88 cm long reactors of respectively condensed 14 g and 13 g of soot. Due to its smaller inner surface area, the thickness of the non-recoverable chlorinated carbon layer was less important in short reactor than the one observed in a longer reactor.

7.3.4 Effect of Reactor Length on Fullerene Production

Using the same operating conditions as in the previous section, the soot coming from the four different regions in the reactor were submitted to HPLC analysis. Soot coming from the disk area was observed to be darker than soot coming from other regions in the reactor. This soot yielded the highest percentage of extraction (up to 97%) and fullerene content (Table 7.5). Therefore, its black color at the collection moment was a good signal to evaluate the degree of purity. Table 7.5 represents preliminary soot yields, % extract, % C_{60} in extract, % C_{60} in soot and fullerene yields obtained with the cylindrical reactor. These being compared to the optimized spherical reactor results running at the same operating conditions. The results obtained in the cylindrical reactor are of preliminary nature, because no reactor optimization has been done so far. It is to be noted that the soot

collected in the cooling zone was not analyzed due to its brownish color, revealing a poor degree of purity. As opposed to the MS output (Figure 4.1), these trials gave no significant C_{70} trace according to the HPLC outputs.

Table 7.5: C₆₀ yields in cylindrical associated with the length or the type of reactor

Collection	Site	Before Disk	Disk Area	After Disk	Cooling Zone
Soot Yield (g)	40 cm	1.71	13.23	2.45	0.3
	63 cm	1.23	11.03	1.18	0.39
	88 cm	1.33	12.03	N/A	0.15
	Spherical (overall)	THE STATE OF	13.1		
% Extract	40 cm	94.4	41	N/A	N/A
	63 cm	N/A	95.3	81.4	N/A
	88 cm	69.6	96.5	N/A	N/A
	Spherical		27.5		
% C ₆₀ in Extract	40 cm	0.15	0.17	N/A	N/A
	63 cm	N/A	0.47	0.087	N/A
	88 cm	0.48	0.81	N/A	N/A
	Spherical (overall)	Filtran Control of the Control of th	11.3%		
% C ₆₀ in Soot	40 cm	0.14	0.07	N/A	N/A
	63 cm	N/A	0.45	0.07	N/A
	88 cm	0.33	0.79	N/A	N/A
	Spherical (overall)	ere kut j ija. Sosa ya ereka akt	3.1		
C ₆₀ Yield	40 cm	1.65	6.39	N/A	N/A
$(mg C_{60}/mol C_2Cl_4)$	63 cm	N/A	34.23	0.57	N/A
	88 cm	3.03	65.54	N/A	N/A
	Spherical (overall)		350		

The preliminary results in the cylindrical reactor indicate substantially smaller C_{60} yields compared to the small spherical geometry (ID=30 cm). At this point however, no significant comparison of the absolute yields in the two systems can be made since no optimization of the wall temperature at the soot collection plate was performed. Alexakis results [1] correspond to data following a long optimization effort particularly with regards to wall temperature and plasma torch efficiency, while the present cylindrical

reactor data are still of a preliminary nature. The plasma torch used in the present reactor was shown to be less efficient than the one used in the spherical reactor (Table 7.3). This yields to realize that a certain amount of energy, supposedly attributed for the thermal plasma dissociation of C₂Cl₄ in this case, is loss in the torch cooling water. The dissociation of C₂Cl₄ in the plasma flame is thus less efficient and the reactor walls remain colder than the optimized temperature for a good fullerene production. Furthermore, these experiments were run with optimized operating conditions evaluated for the original spherical reactor. A cylindrical reactor might perform larger fullerene yields using another range of operating parameters.

The collecting wall temperature was shown to strongly influence the percentage of C_{60} and C_{70} , as well as the quantity of chlorinated by-products generated in the original reactor [1]. The MS output (Figure 4.1) attests the high production of impurities. The trend observed in the C_{60} fraction with increasing reactor length is however very interesting. Despite of a lower amount of soot recovered, a longer reactor produces C_{60} in a larger yield. It follows the idea that yield should be increasing with larger residence times of the fullerene precursors in the formation temperature window, which is the case when increasing the reactor length.

A ten-fold increase in C_{60} yield is observed (Table 7.5) by essentially doubling the reactor length from 40 cm to 88 cm. The calculated residence time in the 2200-2600K temperature window varies only by 26% in the same length increase. These calculated residence times might be quite far from reality if one considers the unrealistic 2200-2600 K temperature window on the overall reactor length. The optimized 30 cm ID spherical reactor yields are around 50 times larger than the 40 cm long cylindrical reactor. Since the spherical reactor has its torch recessed by 10 cm in one port, both cases are essentially the same as far the plasma torch nozzle to end wall distance is 40 cm. One can thus expect similar C_{60} yields results should be attainable with the cylindrical geometry through an optimization of the wall temperature at the collection sites.

7.3.5 Soot Quality Reproducibility

Reactors of 63 cm and 88 cm long gave the best soot quality as reported in the previous section. Replicate runs were performed using these reactor lengths at the same operating conditions (pressure, C₂Cl₄ feed rate, torch power, time of experiment) in order to verify how reproducible is the actual system. Since 80% of the soot is collected at the disk level, soot coming from the disk area for each replicate is compared according to their quality in Figure 7.12 and Table 7.6. The percentage of C₆₀ in the soot extract was chosen as the soot quality indicator and the reproducibility number is represented as the standard deviation computed between each replicate soot quality.

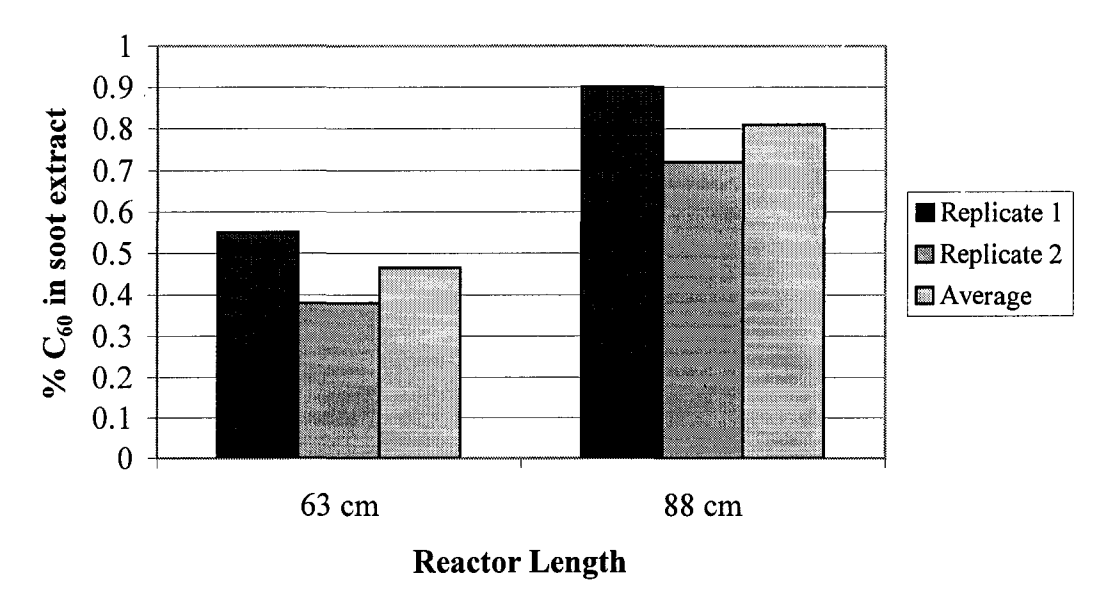


Figure 7.12: Replicate comparison following their soot quality

Table 7.6: Standard deviation calculations of replicate soot quality

Length	Replicate 1 (%C ₆₀ in soot extract)	Replicate 2 (%C ₆₀ in soot extract)	Average (%C ₆₀ in soot extract)	Standard Deviation (%C ₆₀ in soot extract)
63 cm	0.55	0.38	0.47	0.12
88 cm	0.9	0.72	0.81	0.13

Soot quality of replicates show values that are in the same order of magnitude in the 0-1% C_{60} range. Percentage differences between replicate 1 and 2 are respectively 30% and 20% for reactor of 63 cm and 88 cm long. These percentage differences are high, because

they are normalized to the low yields of fullerenes obtained so far. The calculated standard deviations seem also high when associated to the low yields of fullerenes. However, a standard deviation within the 0.15% would reflect a good reproducibility of the plasma system if compared to optimized values of the order of 3.0% as obtained by Alexakis [1]. Nevertheless, the reproducibility number was found to be independent of the variation of the reactor length. Therefore, reproducibility may depend on the degree of mixing of the precursor species in the plasma jet and on the control of the reactor wall temperature. At this point, no goal value of standard deviation has been set, since the system optimization was not achieved and reproducibility was computed only with two replicates. It is thus difficult to evaluate the size of the obtained reproducibility number.

Conclusions

Fullerene synthesis based on the thermal plasma dissociation of C₂Cl₄ was studied in a variable length cylindrical reactor. This project was the continuity of work started and formerly developed by *Pyrogenesis Inc.* in Montreal, Canada with a spherical-shaped reactor. Poor temperature control at the collection sites and limitations of the precursor residence time in a specified synthesis zone led to this new study with a cylindrical reactor geometry. Contrary to the spherical reactor (ID=30 cm) that strongly limited the plasma tailflame expansion, the new water-cooled reactor (ID=30 cm) was designed with cylindrical geometry and flexibility to modify the length of the expanding plasma flame up to L=100 cm. A quartz window provides optical access to the plasma jet for spectroscopy measurements for the first 30 cm downstream of the plasma torch nozzle. A 100 kW non-transferred d.c. plasma torch is used for the dissociation of TCE injected in the torch nozzle. The modeled temperature profile is compared with experimental profiles obtained from atomic and molecular spectroscopy. The T-profile findings are presented and used to explain the fullerene soot collection yields.

The modeling part showed a very promising potential, giving higher precursor residence times of the order of 100 times in the temperature formation window than those calculated for the spherical geometry. CFD calculations of a longer reactor revealed a greater expansion of the 2200-2600K temperature window, establishing fullerene formation. Doubling the reactor length, the fullerene precursor residence time in the formation temperature window increased by 26%. Furthermore, the modeling profiled a minimization of cold gas re-entrainment at the torch nozzle exit and a reduction of the gas velocity gradient compared to the original reactor. These two effects should favor higher fullerene yields and formed the basic idea behind the change to a free axial expansion of the plasma tailflame opposed to the strong quenching re-circulation induced by the spherical profile.

Experimental temperatures extracted from two helium excitation lines follow an unusual scattered pattern, which is not close to temperatures calculated from the Swan band (C_2) under LTE assumption. Temperatures calculated from the Swan Band displayed a reasonable decreasing trend from 4000 K at the torch nozzle to 3500 K at 7.5 cm away from the nozzle at 45 kW torch power and 0.15 mol/min C_2Cl_4 feed rate. Hence, the fullerene formation temperature window (2200-2600K) is predicted to be further downstream in the reactor. Only two lines of helium giving the least amount of interference with chlorine radiation were available. The helium based temperature measurements were unreliable because only two emission lines could be used, whereas the C_2 temperature extraction uses ten rotational lines.

The experimental temperature profile obtained by optical spectroscopy was much lower on the plasma centreline axis than suggested by the model (around 10 000 K) at the same operating conditions. Due to the time limitation of the experiments and lack of radial diagnostic acquisition, the Abel inversion for local temperature determination could not be computed and only some average temperature values along an optical line of sight were calculated along two radial positions (0, 0.6 cm). Considering there is no emission of the Swan band for temperature of the order of 10 000 K, the C2 Swan band cannot evaluate the temperature of the plasma jet core. The Swan band, showing off-axis peaks of intensity, is very seldom used to evaluate core temperature of the jet. Therefore, this higher core temperature is expected to be in a range where practically no C₂ emission exists. The resulting low temperatures may thus be attributed to the absence of the C₂ emission in the core of the plasma jet. Nevertheless, the off-axis temperatures measured from the Swan band are comparable with those calculated from the modeling. For a radial distance of 0.6 cm, experimental and modeled temperatures are very closed to each other at the end of the tailflame. One should note here that no experimental temperature profiles could be obtained on the original spherical reactor to validate modeling in this case.

Fullerene production runs were performed using 55 kW torch power and 0.29 mol/min C₂Cl₄ feed rate for three different reactor lengths: 40 cm, 63 cm and 88 cm. Soot was

collected and sampled individually according to defined collection zones in the reactor. Samples were weighed and analyzed through Mass Spectrometry (MS) and HPLC methods for fullerene quantification. Soot collected on the end disk counted for more than 80%.

Total mass recovery of the shortest reactor used (40 cm) and the original 30 cm ID spherical reactor are in agreement to their similar size. The former recovered 7.36% of the total mass of C₂Cl₄ and the latter, 6.8%. Reactors of length of 63 cm and 88 cm respectively condensed 5.75% and 5.29% of the total mass of C₂Cl₄ fed in the reactor. The strong limitations of the formation temperature window and large cooling gas recirculation in the plasma jet offered by a short reactor and the spherical shape reactor encourage a high soot condensation. Also, wall temperature is known to be a key factor in fullerene soot condensation rate [1]. Insufficient temperatures increase by-product formation, while excessive high temperatures produce loss of C₆₀ by sublimation. The low results using long cylindrical geometries and the decreasing mass recovery as functions of reactor length are attributed to a poor temperature optimization of the reactor inner walls. The plasma radiation and convection energies were transferred to a larger surface area in the 63 cm and 88 cm long cylindrical reactors than in shorter geometries, predicting lower wall temperature. During the first minute of operation, the cold reactor walls condensed a layer of sticky chlorinated carbon compounds, which was not recoverable in the soot. And this sticky layer became more important as increasing the reactor length.

The overall yield of fullerenes improved by increasing the reactor length from 8.04 mg C₆₀/mol C₂Cl₄ for a 40 cm long reactor, 38.87 mg C₆₀/mol C₂Cl₄ for a 63 cm long reactor, to 68.57 mg C₆₀/mol C₂Cl₄ for an 88 cm long reactor. The 30 cm ID spherical reactor achieved a yield of 350 mg C₆₀/mol C₂Cl₄. HPLC results gave no significant trace of C₇₀. At this point, no significant comparison can be made between yields of both systems. Trials in the cylindrical reactor were performed with non-optimized wall temperature and torch efficiency using operating parameters tuned for the spherical reactor. Thus, the

actual data in the cylindrical reactor are still of a preliminary nature. The increasing fullerene yield trend as function of reactor length is however very interesting. It follows the idea that yield should be increasing with larger residence times of the fullerene precursors in the formation temperature window, which is the case when increasing the reactor length.

Analysis on replicate soot quality showed low system reproducibility when normalized to obtained low fullerene yields. Such computed standard deviations will represent a better reproducibility, when compared to optimized fullerene yields. Reproducibility was independent of the reactor length. It may thus depend on the degree of mixing of the fullerene precursor in the plasma jet and/or on the control of the reactor wall temperature.

In summary, the following specific findings were obtained:

- Measured temperature values are in the same order of magnitude at
 a certain radial distance away from the plasma centreline axis as
 the model predictions. Experimental evaluation of the jet core
 temperature could not be made in this project. Faster data
 acquisition of I(y) profiles are needed to perform Abel inversion on
 atomic lines;
- C₆₀ yield correlated with an increase of the reactor length;
- Poor wall temperature and torch efficiency optimization resulted in an increase of by-product formation and lower C₆₀ yields;
- The length of reactor does not affect the system reproducibility.

Future Work

The modeling study predicted a higher fullerene production potential than the original spherical geometry. First of all, the following optimizing solutions should help and improve directly the fullerene yield:

- Increase the fullerene collecting site temperature up to its optimum value by adding insulating material. Presently, the process is running far under its optimal temperature as demonstrated by the optimization process performed in the spherical reactor [1] and the product recovery results for various reactor lengths.
- Bring geometrical modifications in the reactor to minimize convective and radiative heat loss stimulated by the large cooled gas re-circulation at the torch nozzle exit. The reason of such modifications is the interest to expand the fullerene formation temperature window. Among the preliminary ideas, a graphite tube surrounding the plasma flame has been suggested to isolate the fullerene formation zone from the rest of the reactor space.
- After the above modifications have generated better C_{60} and higher fullerene yields, trials with argon as plasma-forming gas must be investigated, due to its significant lower cost over helium.

A new trend in the fullerene synthesis field relates to the injection of metallic particles for a catalytic production of carbon nanotubes [11][23][49]. Such particles initiate a catalytic interaction at the metal-carbon interface, which favors the growth of C_{60} , C_{70} and higher molecules, nanotubes for instance. This would be a good extension of the present work, since the same fullerene reactor would be set up for carbon nanotube production.

References

- 1. Alexakis, T. (1997), Production of fullerenes via the thermal plasma dissociation of tetrachloroethylene (C₂Cl₄), Ph. D. Thesis, CRTP, McGill University, Dept. of Chem. Eng.
- 2. Alexakis, T., Tsantrizos, P.G., Tsantrizos, Y.S., Meunier, J.-L. (1997), Synthesis of fullerenes via the thermal plasma dissociation of hydrocarbons, Appl. Phys. Lett., 70 (16), 2102-2104.
- 3. Barbe, D.F., Charge-coupled devices, Springer-Verlag, New York, 1980.
- 4. Berghaus, J.O. (2000), Substrate bias assisted RF thermal plasma diamond deposition, Ph. D. Thesis, CRTP, McGill University, Dept. of Chem. Eng., Chapter 4.
- 5. Baum, R. (1993), Fullerenes produced by harnessing sunlight, Chemical & Engineering News, 71, 21-22.
- 6. Bilodeau, J.-F., Alexakis, T., Meunier, J.-L., Tsantrizos, P.G. (1997), Model of the synthesis of fullerenes by the plasma torch dissociation of C₂Cl₄, J. Phys. D: Appl. Phys., **30**, 2403-2410.
- 7. Boulos, M.I., Fauchais, P., Pfender, E., *Thermal Plasmas: Fundamental and Applications*, vol. 1., Plenum Press, New York, 1994.
- 8. Buie, M.J., Pender, J.T.P., Holloway, J.P., Vincent, T., Ventzek, P.L.G., Brake, M.L. (1996), *Abel's Inversion Applied to Experimental Spectroscopic Data with Off Axis Peaks*, J. Quant. Spectrosc. Radiat. Transfer, **55** (2), 231-243.
- 9. Chang, T-M., Naim, A., Ahmed, S.N. (1992), On the mechanism of fullerene formation. Trapping of some possible intermediates, J. Am. Chem. Soc., 114, 7603-7604.
- Chen, H.S., Kortan, A.R., Haddon, R.C., Kaplan, M.L., Chen, C.H., Mujsce, A.M., Chou, H., Fleming, D.A. (1991), *Reactivity of C₆₀ in Pure Oxygen*, Appl. Phys. Lett., 59 (23), 2956-2958.
- 11. Cota-Sánchez, G., Merlo-Sosa, L., Huczko, A., Soucy, G. (2001), *Production of Carbon Nanostructure Using a HF Plasma Torch*, Proc. of ISPC-15, **2**, 515-520.
- 12. Dresselhaus, M.S., Dresselhaus, G., Eklund, P.C., Science of Fullerenes and Carbon Nanotubes, Academic Press, New York, 1996.
- 13. Duclos, S.J., Brister K., Haddon, R.C., Kortan, A.R., Thiel, F.A. (1991), *Effects of Pressure and Stress on C*₆₀ Fullerite to 20 GPa, Nature (London), **351**, 380-382.

- 14. Fischer, J.E., Heiney, P.A., McGhie, A.R., Romanow, W.J., Denenstein, A.M., McCauley, J.P. Jr, Smith, A.B., III (1991), *Compressibility of Solid C*₆₀, Science, **252**, 1288-1290.
- 15. Gao, X., Gao, J. (1994), Electrochemical mechanism for fullerene formation in plasma arcs, J. Phys. Chem., **98**, 5618-5621.
- 16. Goeres, A., Sedlmayr, E. (1991), On the Nucleation Mechanism of Effective Fullerite Condensation, Chem. Phys. Letts, **184** (4), 310-317.
- 17. Gruen., D.M., Liu, S., Krauss, A.R., Pan, X. (1994), Fullerenes as precursors for diamond film growth without hydrogen or oxygen additions, Appl. Phys. Lett., 64, 1502-1504.
- 18. Gruen., D.M., Liu, S., Krauss, A.R., Pan, X. (1994), Buckyball microwave plasmas: Fragmentation and diamond-film growth, J. Appl. Phys., 75, 1758-1763.
- 19. Hauffler, R.E., Conceicao, J., Chibante, L.P.F. (1990), Efficient production of C_{60} , $C_{60}H_{36}$, and the solvated buckide ion, J. Phys. Chem., **94**, 8634-8636.
- 20. Heath, J.R. (1992), Synthesis of C₆₀ from Small Carbon Clusters, in <u>Fullerenes:</u> Synthesis, Properties and Chemistry of Large Carbon Clusters, Hammond, G.S., Kuck, V.J., ACS, Washington D.C.
- 21. Howard, J.B., Lafleur, A.L., Makarovsky, Y., Mitra, S. (1992), Fullerenes synthesis in combustion, Carbon, 30 (8), 1183-1201.
- 22. Huczko, A., Lange, H., Byszewski, P. (1997), Fullerene formation in carbon arc: electrode gap dependence and plasma spectroscopy, J. Phys. Chem. A, 101, 1267-1269.
- 23. Huczko, A., Lange, H., Sogabe, T. (2000), Influence of Fe and Co/Ni on Carbon Arc Plasma and Formation of Fullerenes and Nanotubes, J. Phys. Chem. A., 104 (46), 10708-10712.
- 24. Hunter, J.M., Fye, J.L., Roskamp, E.J. (1994), Annealing carbon cluster ions: a mechanism for fullerene synthesis, J. Phys. Chem., 98, p. 1810-1818.
- 25. Kikuchi, K. Nakahara, N., Wakabayashi, T., Honda, M., Matsumiya, H., Moriwaki, T., Suzuki, S., Shiromaru, H., Saito, K., Yamauchi, K., Ikemoto, I., Achiba, Y. (1992), *Isolation and Identification of Fullerene Family: C*₇₆, C₇₈, C₈₂, C₈₄, C₉₀ and C₉₆, Chem. Phys. Letts., **188** (3,4), 177-180.
- 26. Kroto, H.W., Heath, J.R., O'Brien, S.C., Curl, R.F., Smalley, R.E. (1985), Buckminsterfullerene, Nature (London), 318, 162.

- 27. Lafleur, A.L., Howard, J.B., Marr, J.A. (1993), Proposed fullerene precursor corannulene identified in flames both in the presence and absence of fullerene production, J. Phys. Chem., 97, 13539-13543.
- 28. Lange, H., Saidane, K., Razafinimanana, M., Gleizes, A. (1999), Temperatures and C₂ Column Densities in a Carbon Arc Plasma, J. Phys. D: Appl. Phys., **32**, 1024-1030.
- 29. Li, J., Komiya, S., Tamura, T., Nagasaki, C., Kihara, J., Kishio, K., Kitazawa (1992), Growth and Properties of Pure C₆₀ Single Crystals from Vapor, Physica C, **195**, 205-208.
- 30. Lochte-Holtgreven, W. (1968), *Plasma diagnostics*, North-Holland Publishing Co., Amsterdam, Netherlands, Chapter 3.
- 31. McKinnon, T.J. (1991), Calculated equilibrium yields of C_{60} from hydrocarbons pyrolysis, J. Phys. Chem., **95**, 8941-8944.
- 32. Mclean, D.G., Sutherland, R.L., Brant, M.C., Brandelik, M.D., Fleitz, P.A., Pottenger, T. (1993), *Non-linear absorption study of a C*₆₀-toluene solution, Opt. Lett. **18**, 858.
- 33. Manuel, N. R., Monceau P., Hodeau, J.-L. (1992), Crushing C₆₀ to Diamond at Room Temperature, Nature, 355, 237-239.
- 34. Melunas, R.J., Change, R.P.H., Liu, S., Kappes, M. (1991), *Nucleation of diamond films on surfaces using carbon clusters*, Appl. Phys. Lett., **59**, 3461-3463.
- 35. Mermet, J.-M., Robin, J.-P. (1973), Étude de l'inversion d'Abel en vue de la mesure de la répartition de la température dans un plasma inductif, Rev. int. Htes Temp. et Réfract., 133-139.
- 36. NIST Atomic Spectra Database Lines Form (1999), http://physics.nist.gov/cgi-bin/AtData/lines_form
- 37. Paquin, G., *Carbone 60 La nouvelle vedette de la chimie*, Québec Science, Apr. 1992, p. 20-3.
- 38. Perry, R.H., Green, D., *Perry's Chemical Engineering Handbook*, 6th Edition, McGraw-Hill Chemical Engineering Series, New York, 1984, pp. 18-19 to 18-23.
- 39. Pope, C.J., Marr, J.A., Howard, J.B. (1993), Chemistry of fullerenes C60 and C70 formation in flames, J. Phys. Chem., 97, p. 11001-11013.
- 40. Robinson, J.W., *Atomic Spectroscopy*, 2nd edition, rev. and expanded, Marcel Dekker, New York, 1996.

- 41. Saidane, K. (1999), Caractérisation expérimentale d'un plasma d'arc à électrodes de graphite dans l'hélium. Contribution à l'optimisation de la production des fullerenes, Ph. D. Thesis, Université Paul-Sabatier, Toulouse III, Centre de Physique des Plasmas de leurs Applications à Toulouse (CPAT).
- 42. Saxby, J.D., Chatfield, S.P., Palmisano, A.J., Vassallo, A.M., Wilson, M.A., Pang, L.S.K. (1992), *Thermogravimetric Analysis of Buckminsterfullerene and Related Materials in Air*, J. Phys. Chem., **96** (1), 17-18.
- 43. Schön, J.H., Kloc, C., Batlogg, B. (2001), *High-Temperature Superconductivity in Lattice-Expanded C*₆₀, Science, **293**, 2432-2434.
- 44. Smalley, R.E. (1992), Self-Assembly of the Fullerenes, Acc. Chem. Res., 25 (3), 98-105.
- 45. Strout, D.L., Scuseria, G.E. (1996), A cycloaddition model for fullerene formation, J. Phys. Chem., 100, 6492-6498.
- 46. Sum, K. (1999), Fullerene Study from Vaporization of Graphite in a Thermal Plasma Jet, M.Eng. Thesis, CRTP, Dept. of Chemical Engineering, McGill University.
- 47. Taylor, R., Walton, D.R.M. (1993), *The chemistry of fullerenes*, Nature, **363**, 685-693.
- 48. Trutt, L.W., Kost, A. (1992), Optical Limiting Performance of C₆₀ and C₇₀ Solutions, Nature, **356**, 225-226.
- 49. Wang C., Imahori, T., Tanaka, Y., Sakuta, T., Takikawa, H., Matsuo, H. (2001), Synthesis of Fullerene with C-Si, Mixed Particles by Using Induction Thermal Plasma, Proc. of ISPC-15, 7, 2817-2822.
- 50. Wang, X.K., Zhang, T.G., Lin, W.P., Liu, S.K., Wong, G.K., Kappes, M.M., Chang, R.P.H., Ketterson, J.B. (1992), *Large second-harmonic response of C60 thin films*, Appl. Phys. Lett., **60**, 810-812.
- 51. Withers, J.C., Loutfy, R.O., Lowe, T.P. (1997), Fullerene Commercial Vision, Fullerene Science and Technology, 5 (1), 1-31.
- 52. Xie, S.-Y., Huang, R.-B., Yu, L.-J., Ding, J, Zheng, L.-S. (1999), *Microwave synthesis of fullerenes from chloroform*, Appl. Phys. Letts., **75** (18), 2764-2766.

Appendix I: C₆₀ physical constants

Table AI.1: Physical constants for C₆₀ molecules [12]

Quantity Quantity	Value Value
Average C-C distance	1.44 Å
C-C bond length on a pentagon	1.46 Å
C-C bond length on a hexagon	1.40 Å
C ₆₀ mean ball diameter	7.10 Å
C ₆₀ ball outer diameter	10.34 Å
Moment of inertia I	$1.0 \times 10^{-43} \text{ kg m}^2$
Volume per C ₆₀	$1.87 \times 10^{-22} / \text{cm}^3$
Binding energy per atom	7.40 eV
Heat of formation (per g C atom)	10.16 kcal
Electron affinity	$2.65 \pm 0.05 \text{ eV}$
Cohesive energy per C atom	1.4 eV/atom
Spin-orbit splitting of C (2 p)	$2.2 \times 10^{-4} \text{ eV}$
-First ionization potential	7.58 eV
Second ionization potential	11.5 eV
Optical absorption edge	1.65 eV

Table AI.2: Physical constants for crystalline C ₆₀ in the solid state [12]				
Quantity	Value			
fcc Lattice constant	14.17 Å			
C ₆₀ -C ₆₀ distance	10.02 Å			
C ₆₀ -C ₆₀ cohesive energy	1.6 eV			
Tetrahedral interstitial site radius	1.12 Å			
Octahedral interstitial site radius	2.07 Å			
Mass density	1.72 g/cm ³			
Molecular density	$1.44 \times 10^{21} / \text{cm}^3$			
Compressibility (-dln V/dP)	6.9 X 10 ⁻¹² cm ² /dyne			
Bulk modulus	6.8, 8.8 GPa			
Young's modulus	15.9 GPa			
$D\mathrm{T}_{01}/dp$	11 K/kbar			
Vol. Coeff. of thermal expansion	6.1 X 10 ⁻⁵ /K			
Optical absorption edge	1.7 eV			
Work function	$4.7 \pm 0.1 \text{ eV}$			
Velocity of sound v_t	$2.1 \times 10^5 \text{ cm/s}$			
Velocity of sound v_l	$3.6 - 4.3 \times 10^5 \text{ cm/s}$			
Debye temperature	185 K			
Thermal conductivity (300 K)	0.4 W/mK			
Electrical conductivity (300 K)	1.7 X 10 ⁻⁷ S/cm			
Phonon mean free path	50 Å			
Static dielectric constant	4.0 – 4.5			
Melting temperature	1180°C			
Sublimation temperature	434°C			
Heat of sublimation	40.1 kcal/mol			
Latent heat	1.65 eV/C ₆₀			

Appendix II: Modeling of Different Reactor Length

Modeling Equations [6]

Briefly, the Fortran code solves the equations of continuity and conservation of axial and radial momentum, energy and carbon species in their cylindrical coordinates form. One must note that the plasma torch efficiency, found in Section 7.3.2, is globally inserted in these equations.

Continuity Equation

$$\frac{\partial \rho}{\partial t} + \frac{\partial}{r \partial r} (r \rho v_r) + \frac{\partial}{\partial z} (\rho v_z) = 0$$
 (AII.1)

where t is the time, z and r are respectively the axial and radial coordinates, ρ is the density, and v_z and v_r are the axial and radial components of the bulk gas velocity.

Axial and Radial Momentum Equations

$$\frac{\partial}{\partial t}(\rho v_{z}) + \frac{\partial}{r\partial r}(r\rho v_{r}v_{z}) + \frac{\partial}{\partial z}(\rho v_{z}v_{z}) = -\frac{\partial P}{\partial z} + 2\frac{\partial}{\partial z}(\eta \frac{\partial v_{z}}{\partial z}) + \frac{\partial}{r\partial r}\left[r\eta\left(\frac{\partial v_{z}}{\partial r} + \frac{\partial v_{r}}{\partial z}\right)\right] \text{ (AII.2)}$$

$$\frac{\partial}{\partial t}(\rho v_{r}) + \frac{\partial}{r\partial r}(r\rho v_{r}v_{r}) + \frac{\partial}{\partial z}(\rho v_{z}v_{r}) =$$

$$-\frac{\partial P}{\partial r} + \frac{2\partial}{r\partial r}(r\eta \frac{\partial v_{r}}{\partial r}) + \frac{\partial}{\partial z}\left[\eta\left(\frac{\partial v_{z}}{\partial r} + \frac{\partial v_{r}}{\partial z}\right)\right] - 2\eta \frac{v_{r}}{r^{2}}$$
(AII.3)

in which η is the effective viscosity (laminar + turbulent) and P, the pressure in the reactor.

Energy Equation

$$\frac{\partial}{\partial t}(\rho h) + \frac{\partial}{r\partial r}(r\rho v_r h) + \frac{\partial}{\partial z}(\rho v_z h) = \frac{\partial}{\partial z}\left(\frac{k\partial h}{C_p\partial z}\right) + \frac{\partial}{r\partial r}\left(r\frac{k\partial h}{C_p\partial r}\right) - U \tag{AII.4}$$

where h is the gas specific enthalpy, k the effective thermal conductivity (laminar + turbulent), C_p the specific heat at constant pressure and U is the radiation loss term.

Hydrocarbon Mass Conservation

$$\frac{\partial}{\partial t}(\rho X) + \frac{\partial}{r\partial r}(r\rho v_r X) + \frac{\partial}{\partial z}(\rho v_z X) = \frac{\partial}{\partial z}\left(\rho D\frac{\partial X}{\partial z}\right) + \frac{\partial}{r\partial r}\left(r\rho D\frac{\partial X}{\partial r}\right) - S_m \tag{AII.5}$$

where X is the mass fraction of C_2Cl_4 in the gas and D is the effective mass diffusivity (laminar + turbulent), S_m a mass source term that simulates the rate of condensation of the hydrocarbon at 1600 K.

Effect of turbulence

The contribution of turbulence on the transport coefficient is calculated using the K- ε model. Basically, two additional equations are needed to be solved for the turbulent kinetic energy (K) and its rate of dissipation (ε) :

$$\frac{\partial}{\partial t}(\rho K) + \frac{\partial}{r\partial r}(r\rho v_r K) + \frac{\partial}{\partial z}(\rho v_z K) = \frac{\partial}{\partial z}\left(\eta_k \frac{\partial K}{\partial z}\right) + \frac{\partial}{r\partial r}\left(r\eta_k \frac{k\partial K}{\partial r}\right) - G - \rho\varepsilon \tag{AII.5}$$

$$\frac{\partial}{\partial t}(\rho\varepsilon) + \frac{\partial}{r\partial r}(r\rho v_{r}\varepsilon) + \frac{\partial}{\partial z}(\rho v_{z}\varepsilon) = \frac{\partial}{\partial z}\left(\eta_{\varepsilon}\frac{\partial\varepsilon}{\partial z}\right) + \frac{\partial}{r\partial r}\left(r\eta_{\varepsilon}\frac{k\partial\varepsilon}{\partial r}\right) - C_{d}G\frac{\varepsilon}{K} - C_{2}\rho\frac{\varepsilon^{2}}{K} \quad (AII.6)$$

where η_k and η_{ε} are the effective diffusion coefficients for K and ε , C_d and C_2 are correction factors for region outside the nozzle, and G is given by:

$$G = \eta_t \left\{ 2 \left[\left(\frac{\partial v_r}{\partial r} \right)^2 + \left(\frac{v_r}{r} \right)^2 + \left(\frac{\partial v_z}{\partial z} \right)^2 \right] + \left(\frac{\partial v_z}{\partial r} + \frac{\partial v_r}{\partial z} \right)^2 \right\}$$
(AII.7)

with

$$\eta_t = C_d \rho K^2 / \varepsilon \tag{AII.8}$$

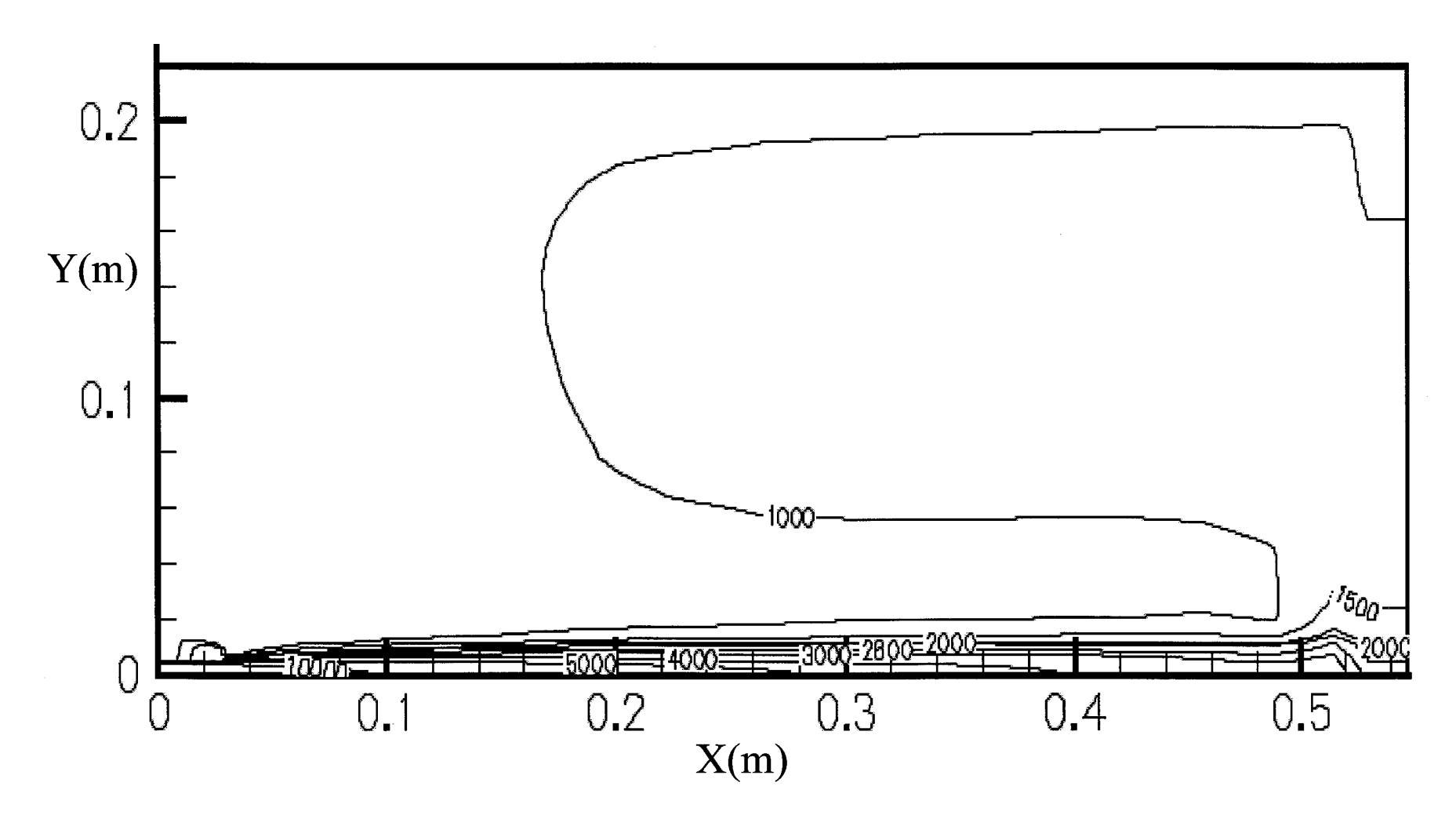


Figure AII.1: Temperature profile (K) from modeling [helium flow: 225 slpm; torch power: 55kW; C₂Cl₄ flow: 0.29 mol/min; pressure: 200 torr, reactor length 40 cm]

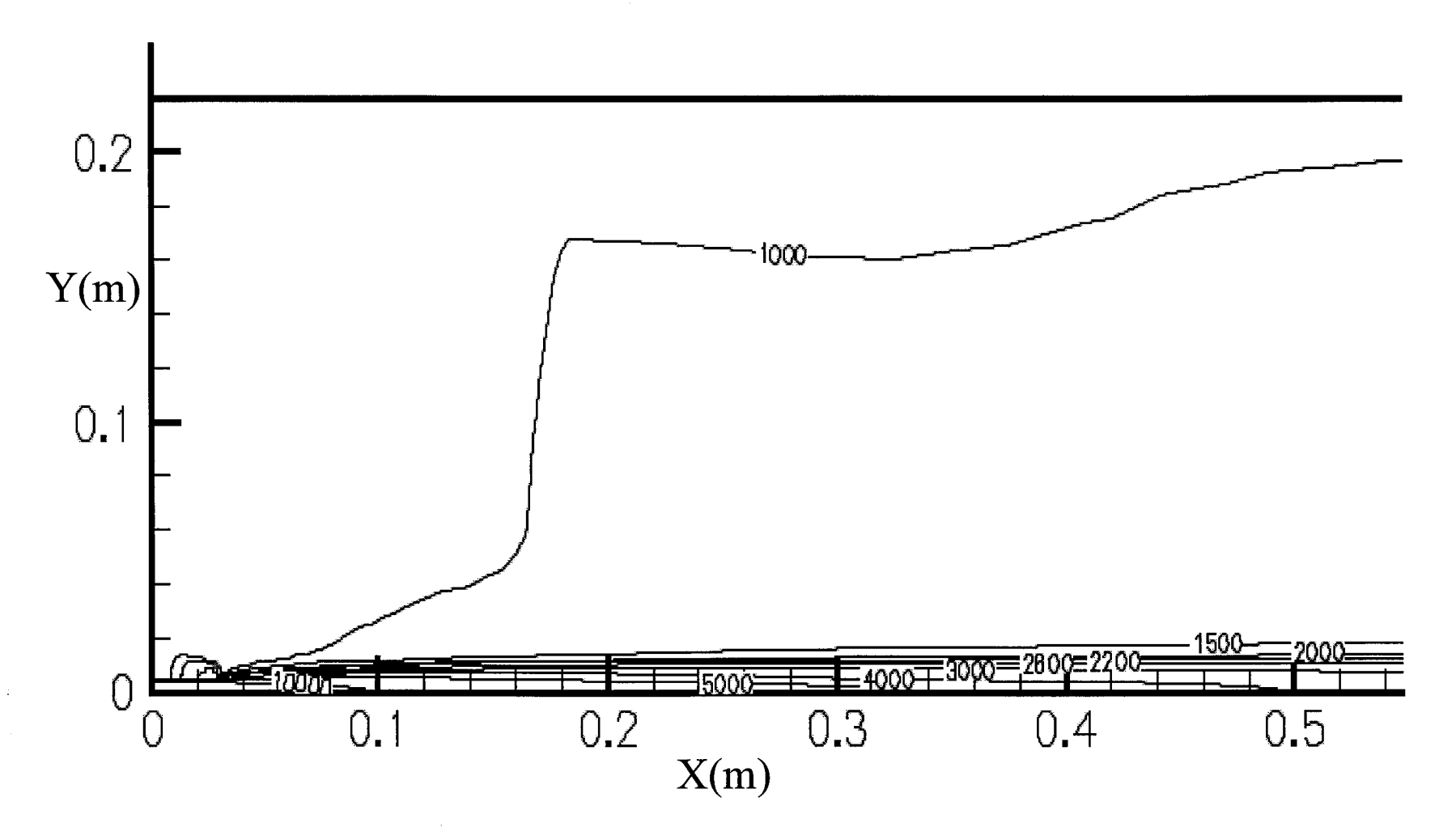


Figure AII.2: Temperature profile (K) from modeling [helium flow: 225 slpm; torch power: 55kW; C₂Cl₄ flow: 0.29 mol/min; pressure: 200 torr, reactor length 63 cm]

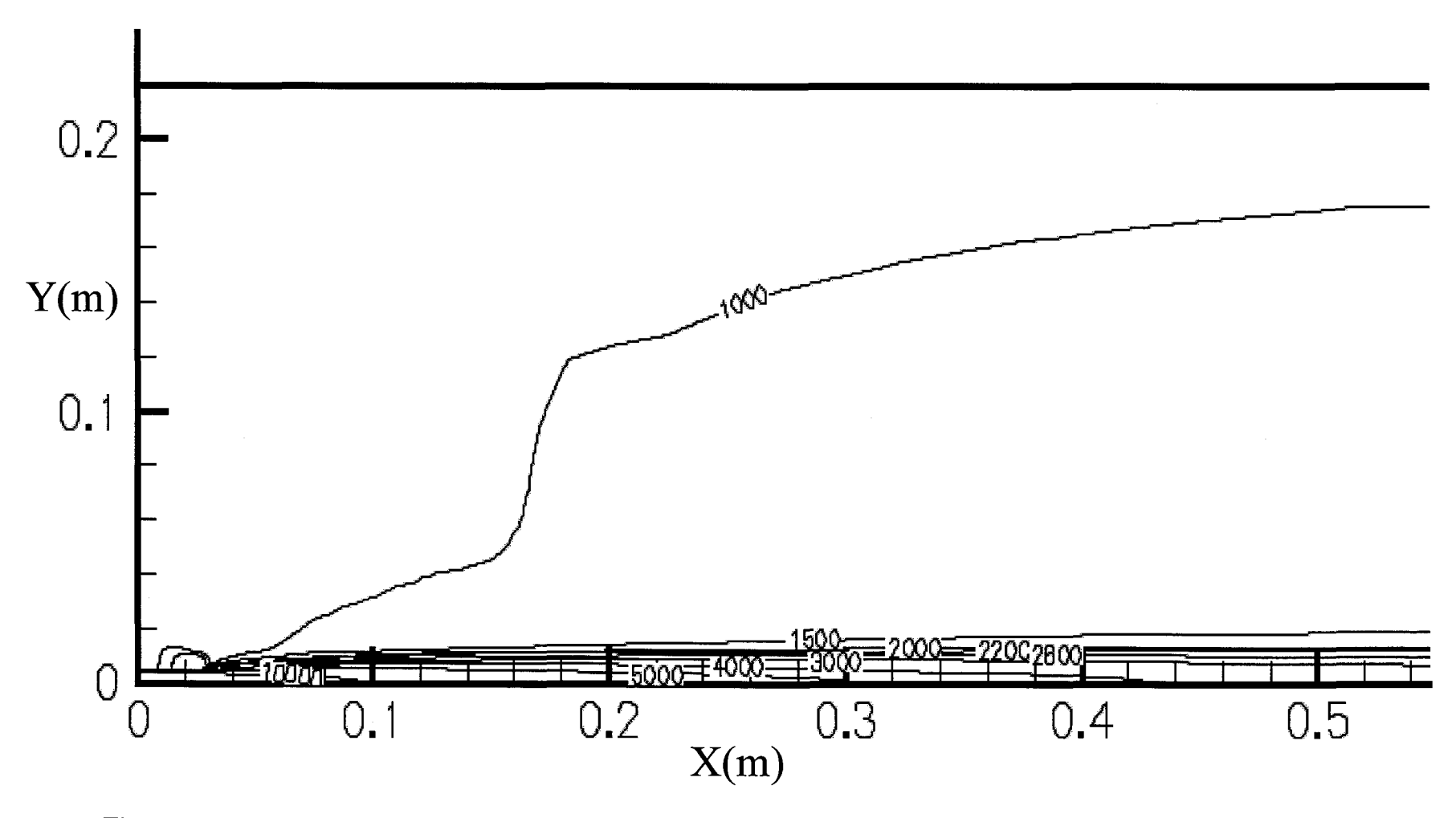


Figure AII.3: Temperature profile (K) from modeling [helium flow: 225 slpm; torch power: 55kW; C₂Cl₄ flow: 0.29 mol/min; pressure: 200 torr, reactor length 88 cm]